

TRANSPORT AND COLLECTIVE MODES IN DIRAC MATERIALS

By

DIBYA KANTI MUKHERJEE

PHYS08201105002

Harish-Chandra Research Institute, Allahabad

A thesis submitted to the

Board of Studies in Physical Sciences

In partial fulfillment of requirements

for the Degree of

DOCTOR OF PHILOSOPHY

of

HOMI BHABHA NATIONAL INSTITUTE

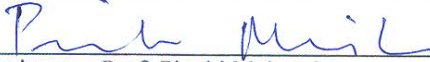


July, 2018

Homi Bhabha National Institute¹

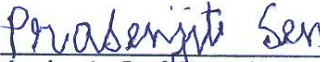
Recommendations of the Viva Voce Committee

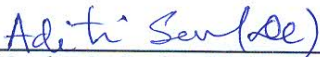
As members of the Viva Voce Committee, we certify that we have read the dissertation prepared by Dibya Kanti Mukherjee entitled "Transport and Collective Modes in Dirac Materials" and recommend that it may be accepted as fulfilling the thesis requirement for the award of Degree of Doctor of Philosophy.


Chairman - Prof. Pinaki Majumdar 30/10/18
Date:


Guide / Convener - Prof. Sumathi Rao 30/10/18
Date:


Examiner - Prof. Tanmoy Das 30/10/2018
Date:


Member 1- Prof. Prasenjit Sen 30/10/18
Date:


Member 2- Prof. Aditi Sen (De) 30/10/18
Date:

Member 3- Prof. G. V. Pai (deceased) Date: N/A

Final approval and acceptance of this thesis is contingent upon the candidate's submission of the final copies of the thesis to HBNI.

i/We hereby certify that I/we have read this thesis prepared under my/our direction and recommend that it may be accepted as fulfilling the thesis requirement.

Date: 29.10.2018

Place: Allahabad


Prof. Sumathi Rao
Guide

¹ This page is to be included only for final submission after successful completion of viva voce.

STATEMENT BY AUTHOR

This dissertation has been submitted in partial fulfillment of requirements for an advanced degree at Homi Bhabha National Institute (HBNI) and is deposited in the Library to be made available to borrowers under rules of the HBNI.

Brief quotations from this dissertation are allowable without special permission, provided that accurate acknowledgement of source is made. Requests for permission for extended quotation from or reproduction of this manuscript in whole or in part may be granted by the Competent Authority of HBNI when in his or her judgment the proposed use of the material is in the interests of scholarship. In all other instances, however, permission must be obtained from the author.

Dibya Kanti Mukherjee

Dibya Kanti Mukherjee

DECLARATION

I, hereby declare that the investigation presented in the thesis has been carried out by me. The work is original and has not been submitted earlier as a whole or in part for a degree / diploma at this or any other Institution / University.

Dibya Kanti Mukherjee
Dibya Kanti Mukherjee

List of Publications arising from the thesis

Journal

1. “Transport through Andreev bound states in a Weyl semimetal quantum dot”, Dibya Kanti Mukherjee, Arijit Kundu and Sumathi Rao Phys. Rev. B, **2017**, 96, 161408 (R).

Preprint

2. “Floquet manipulation of spin-dependent Andreev reflection in spin-orbit coupled systems”, Dibya Kanti Mukherjee, Joanna Hutchinson, Arijit Kundu arXiv:1708.06773 [cond-mat].
3. “Momentum space interferometry in Weyl Semimetals”, Dibya Kanti Mukherjee, Sumathi Rao, Sourin Das, arXiv:1710.06873 [cond-mat].
4. “Spin Response and Collective Modes in Simple Metal Dichalcogenides”, Dibya Kanti Mukherjee, Arijit Kundu, H. A. Fertig, arXiv:1805.08223 [cond-mat].

Further Publications of candidate not used substantially in this thesis

5. “Chiral nodes and oscillations in the Josephson current in Weyl semimetals”, Udit Khanna, Dibya Kanti Mukherjee, Arijit Kundu and Sumathi Rao Phys. Rev. B, **2015**, 93, 121409 (R) .

Conferences

1. School on Topological Quantum Matter at HRI, Allahabad, India (9 - 21 Feb 2015). Presented poster titled “Andreev bound states in Weyl semimetal - superconductor heterojunctions”.
2. Conference on Interactions and Topology in Dirac Systems at ICTP, Trieste, India (3 – 9 August 2016). Presented poster titled “Chiral nodes and oscillations in the Josephson current in Weyl semimetals”.

Others

1. Tutor for the course ‘An Introduction to Anyons’ by Sumathi Rao at the school ‘An Advanced School and Topical Workshop on Topological Particles in Condensed Matter’
2. Teaching Assistant for the course “Advanced Quantum and Statistical Mechanics” during August-December, 2014.

3. Teaching Assistant for the course “Advanced Quantum Mechanics” during January-May, 2015.

Dibya Kanti Mukherjee

Dibya Kanti Mukherjee

DEDICATION

*Dedicated to my parents Deb Kumar and Chandana Mukherjee,
my sister Debapriya
and my wife Samarpita*

ACKNOWLEDGEMENTS

I would like begin by expressing my gratitude towards my advisor Prof. Sumathi Rao. Her enthusiasm for physics and ability to assimilate new directions of research is infectious. This thesis would not have been possible without her invaluable support in the days of despair. I would sincerely like to thank her for her kindness and her constant display of belief in me. I thank Prof. Arijit Kundu for our numerous discussions. He has truly acted as a friend, philosopher and guide throughout my PhD tenure. I would also like to thank Prof. H.A. Fertig and Prof. Sourin Das who have introduced me to several aspects of physics previously unknown to me.

I express my sincere gratitude to all my teachers at HRI. I am indebted to Prof. Ashoke Sen, Prof. Rajesh Gopakumar, Prof. Raj Gandhi, Prof. Biswarup Mukhopadhyay, Prof. Anshuman Maharana, Prof. Anirban Basu, Prof. Sandhya Choubey, Prof. Jayanta Kumar Bhattacharjee, Prof. G. V. Pai, Prof. Pinaki Majumdar, Prof. Prasenjit Sen, Prof. Aditi Sen De, Prof. Ujjwal Sen and Prof. Sandhya Choubey for the excellent teaching and discussions. I am grateful to the people in the technical section of HRI. In particular, I would like to mention Rajiv, Chandan, Ravi, Mr. Sanjay Verma, and Mr. Amit Khulve for their constant supports. I must also thank DAE and HBNI for their help and financial support. I gratefully acknowledge the financial support provided by the Infosys Foundation as the form of ‘Infosys scholarship for senior students’.

It gives me immense pleasure to thank my collaborators, Dr. Udit Khanna and Dr. Joanna Hutchinson for the many captivating discussions during our colorful collaborations. Several discussion sessions with my colleagues Abhishek Joshi, Samrat Kadge, Arijit Dutta, Sauri Bhattacharyya, Aditya Banerjee, Subhronel Chakrabarti, Krashna Mohan Tripathi, Swapnamay Mondal have been extremely enriching and illuminating. I would also like to thank Samrat, Arijit and Titas Chanda for helping me out with coding on several occasions.

Next, the turn for my fellow HRImates, with whom I spent one of the most beautiful times of my life, which has made HRI a “Home away from home” for me during the past seven years. My wholehearted thanks goes to Bhuru da, Hochi da, Atri da, Pallab da, Masud da, Bedo da, Shubho da, Nilay da, Gupta, Bachha, Mountain, Samrat, Soumyarup (Hego), Joya, Gunjan, Abdul, Rito(WiFi), Nirmom, Susovan, Jayita di, Indrani di, Landau for all the intense and enjoyable “*adda*”s/discussions/late-night-parties and debates, thereby making my stay at HRI a forever memorable one. I thank Papon, Arif, Kashinath, Gol da, Dhiraj da, Niyogi da, Rana, Taushif da, Sankha da, Godfather, Jonthu da, Tarat da, Paromita di, KMT, Joshi, B, Sarif, Karim, Yogendra da for tolerating me for the past few years as a friend. I thank everyone in HRI for bearing with my jokes, pranks and ridiculous observations about life.

I am forever grateful to my parents and to my wonderful sister, Buri, for supporting me throughout my academic career. No words can describe the gratitude I feel towards my wife, Samarпита, who walked the same journey as me and made even the darkest moments dazzle.

Contents

SYNOPSIS	1
List of Figures	6
List of Tables	15
1 Introduction	17
1.1 Preliminaries	17
1.1.1 The Dirac equation	17
1.1.2 Berry Phase and Chern Numbers	18
1.1.3 Role of Berry phase in condensed matter physics	19
1.2 Dirac Materials	20
1.2.1 Graphene	20
1.2.2 Silicene	24
1.2.3 Transition Metal Dichalcogenides(TMDs)	24
1.2.4 Weyl Semimetals	25
1.3 Structure of the thesis	27
2 Momentum space interferometry in Weyl semi-metals	29
2.1 Time-reversal broken WSM	30
2.1.1 Low energy subspace	31
2.1.2 Spin preserving selection rule	33
2.2 Inversion symmetry broken WSM	35
2.3 Summary and Conclusion	38
3 Transport through Andreev bound states in a Weyl semimetal quantum dot	41
3.1 Modelling a WSM-SC interface for a TRS broken WSM	42
3.1.1 Scattering matrix approach	44
3.1.2 Lattice simulation	48
3.1.3 Inversion symmetry broken WSM	52

3.2	Oscillations in the Josephson current in Weyl semimetals	53
3.2.1	WSM-SC junction	54
3.2.2	Bound levels in the SC-WSM-SC geometry	55
3.2.3	Periodic oscillations in the Josephson current	56
3.3	Summary	57
4	Spin-dependent Andreev reflection in spin-orbit coupled systems by breaking time-reversal symmetry	59
4.1	Pseudo Spin-Orbit Coupled system	61
4.2	Time Reversal symmetry breaking by Periodic drive	63
4.3	Scattering matrix formalism	65
4.4	Spin-dependent Andreev reflection	66
4.5	Summary	69
5	Spin waves in MoS2	73
5.1	Model of the system	74
5.2	Hartree-Fock Approximation	77
5.3	Time dependent Hartree-Fock Approximation	79
5.4	Spin-wave modes for small hole-doping	82
5.5	Numerical Results and Discussion	86
5.6	Summary	89
6	Summary and Future Directions	91
	Bibliography	95

SYNOPSIS

Introduction -

Dirac materials are condensed matter systems where the low energy excitations around a finite number of points in the Brillouin Zone(BZ) behave as either massive or massless Dirac particles [1]. The most well known example is that of graphene which is a two dimensional hexagonal lattice comprised of carbon atoms. In graphene, the gap between the conduction and valence bands vanish at the K and K' points of the BZ and about these points the energy-momentum dispersion is linear, mimicking the massless Dirac equation[2, 3]. In recent years, a large number of seemingly diverse materials have been identified which display similar characteristics. Examples include Weyl semimetals[4], d -wave superconductors[5], surface states of topological insulators[6], etc. These materials, despite being vastly different from each other, exhibit properties which are a direct consequence of their low energy spectrum and hence are universal. Other systems like silicene[7], transition metal dichalcogenides[8] are described by the massive Dirac equation. Most of these have strong spin-orbit coupling which plays a crucial role in transport and other properties. One of the major points of focus of this thesis is to investigate the physical consequences of the nontrivial spin texture of the low energy excitations in these materials.

We next briefly discuss some of the materials studied in the thesis.

Silicene -

Silicene is a two dimensional allotrope of silicon with the atoms arranged on a hexagonal lattice. The lattice, unlike graphene, has a periodically buckled topology due to the relatively larger size of the silicon atoms. Also, compared to graphene, silicene has significantly stronger spin-orbit coupling which leads to a gapped low energy spectrum about the K and K' points. Silicene is of particular interest as the band gap can be tuned by oxidation[9], by application of an electric field perpendicular to the sample or by a biaxial strain[10]; this also makes it a good candidate for monolayer topological insulators[11].

Transition metal dichalcogenides -

Monolayer transition metal dichalcogenides(TMD) are also two dimensional semiconducting materials. The lattice is hexagonal with the metal atoms(*eg*, Mo, W) and the chalcogen(*eg*, S, Se) dimers located at the inequivalent sites. The low energy Hamiltonian about the K and K' points in the BZ is formed by the d -orbital electrons of the transition metal. The inversion symmetry breaking gives rise to a large direct band gap in the spectrum(~ 1 eV). Also, the presence of strong(~ 80 meV) spin-orbit coupling leads to spin split valence bands. This spin splitting, however, is opposite about the K and K' points, resulting in a overall time reversal symmetric spectrum. This results in a spin and valley coupled description of the low energy physics[12]. A small hole doping produces two spin polarized Fermi surfaces with opposite polarization, one about each of the K points.

Weyl semimetals -

Weyl semimetals(WSM) are three dimensional free fermion phases. In such systems, the low energy physics is governed by emergent chiral Weyl fermions around nodes in the BZ where the valence and the conduction bands touch. Just like graphene, the energy-momentum dispersion is linear and is described by the Weyl equation. These Weyl nodes can be viewed as monopoles which act as a source or sink of Berry curvature[13]. As the total Berry flux integrated over the BZ has to be zero, the Nielsen-Ninomiya theorem dictates that there must be an even number of Weyl nodes in the BZ. This prevents the destruction of the WSM phase by a small perturbation. Another novel feature is the presence of Fermi arc surface states which connect the projection of the Weyl nodes on the surface BZ[14]. These systems also exhibit several interesting transport phenomena due to the chiral anomaly[15] such as negative magnetoresistance, and the anomalous Hall effect[16]. In the past few years, it has been shown that TaAs and NbAs classes of materials host Weyl fermionic modes[17].

Summary of the research work -

The thesis consists of mainly two parts. The first part of the thesis contains studies of transport through heterostructures involving Dirac materials and the second part contains an analysis of

spin susceptibility in hole doped TMDs.

Overall, the thesis has seven chapters. They are briefly described in the following:

- In the first chapter, we introduce Dirac materials. We start from the low energy Hamiltonian valid near isolated points in the BZ and provide tight binding realization of the effective low energy theory. In particular, we discuss the two different types of WSMs: Time-reversal symmetry (TRS) broken and inversion symmetry broken, and provide a minimal model describing each of them. We also discuss the buckled honeycomb lattice description of silicene. Lastly, we discuss the simplest model describing the TMDs.
- In the second chapter, we consider a two node (located at $\mathbf{k} = (0, 0, \pm k_0)$) TRS broken Weyl semimetal sandwiched between two normal metal leads. The leads are kept at a small potential difference and the separation between the Weyl nodes ($2k_0$) is varied. We explicitly construct a finite sized lattice and attach the leads via self energy terms in the total Green's function. The current is next calculated using the Green's function of the full system[18]. We find that the current oscillates as a function of $\theta = 2k_0L$ where L is the length of the physical system. The nontrivial spin texture around the Weyl nodes forces the backscattering process at the lead-WSM interface to scatter an electron from one node to the other as long as spin is preserved, giving rise to the aforementioned oscillations. This can be interpreted as a momentum space interferometer where the backscattering channel is analogous to the weakly coupled arm of a Fabry-Perot type interferometer[19]. A similar study is conducted for a minimal model of the inversion symmetry broken WSM with four nodes in the bulk. An additional selection rule is obtained as the backscattering preserves the pseudo-spin degree of freedom.
- In chapter three, we extend the study to transport across WSM-superconductor heterostructures. We first observe a similar pattern in Andreev spectroscopy in a WIS geometry where W is a pristine WSM, I is a WSM with a barrier potential and S is a s -wave superconductor. We study this geometry using both the analytical scattering matrix approach and also numerically using a slightly modified version of the Landauer formalism. In this chapter, we try to disentangle the physics of Klein tunneling (which is probed by changing the barrier

potential) and k_0L oscillations[20]. In fact, as the relevant system parameters are changed, two distinct frequencies emerge: one from the Klein tunneling due to the finite barrier height and one from the chiral nature of the excitations. The calculations are repeated even for the inversion symmetry broken model with similar results. In the same chapter, we briefly look at the Josephson effect for a SWS geometry where W is a WSM and S-s are s -wave superconductors. We find that analogous to the previous cases, the Andreev bound state spectrum exhibits a periodicity as a function of θ and the resulting critical current also displays a similar period. Additionally, the critical current actually changes sign and undergoes a $0 - \pi$ transition[21].

- In chapter four, we explore the possibility of obtaining spin dependent Andreev reflection for a two dimensional system with strong spin orbit coupling when the TRS is broken. We explicitly study the case of silicene, driven with high frequency circularly polarised light by considering an effective static model obtained from the Brillouin-Wigner expansion of the high frequency drive limit[22]. However, our results are not specific to the Floquet system and should be qualitatively seen in other TRS broken systems also.
- Chapter five contains our study of the spin-spin correlation function of a hole doped TMD with screened Coulomb interaction. For concreteness, we take the parameter values of MoS_2 . We first employ the static Hartree-Fock(HF) approximation and find that the HF Hamiltonian has a structure very similar to the original noninteracting Hamiltonian with parameters renormalized depending on the hole doping. These parameters are found self consistently. On top of the ground state of this HF Hamiltonian, we obtain the spin-spin correlation function by performing a time dependent Hartree-Fock approximation analysis and the poles of this function are studied to find spin-wave modes separated from the particle-hole continuum. Interestingly, these spin wave modes are present in this system even though there is no spontaneous magnetic ordering of the ground state. We find that these modes are present for arbitrary small values of the strength of the interaction and should be experimentally observable[23]. Also, limitations of such approaches are also discussed.

- We conclude by summarizing our findings in chapter seven. In this last chapter, we also discuss possible future works.

List of Figures

1.1	(a) Graphene is a two dimensional honeycomb lattice composed of carbon atoms. \mathbf{a}_1 and \mathbf{a}_2 are the unit lattice vectors and δ_i are vectors connecting the nearest neighbour atoms. (b) The hexagonal Brillouin Zone of Graphene. \mathbf{b}_1 and \mathbf{b}_2 are the reciprocal lattice vectors. This figure is taken from [24].	21
1.2	The energy spectrum of the tight binding model of graphene. About the gapless points in the BZ, the energy dispersion is linear. This figure is taken from [24].	22
1.3	The solid lines denote the nearest neighbour bonds whereas the dashed lines show the NNN bonds. $\nu_{ij} = \pm$ signs give us the phase convention for the Haldane model.	23
1.4	(a) The conduction and the spin-split valence bands near the band edges near the K and K' points of the BZ. (b) Strength of the spin-orbit coupling of the valence band in eV. This figure is taken from [8].	24
1.5	(a) The 2D planes between the two Weyl nodes can be thought of integer quantum hall systems with non-vanishing Chern number. (b) The Fermi arcs lie within the projections of the Weyl nodes on the surface BZ. The red line on the surface BZ (k_x - k_y plane) indicates a nonzero LDOS due to the Fermi arc states whereas the yellow plane indicates zero LDOS. Both figures are taken from [25].	26
2.1	A typical phase diagram of our model system. The Weyl semi-metal (WSM) phase appears at the strong topological insulator (STI), normal insulator (NI) ($\epsilon = 6t$) and strong topological insulator (STI), weak topological insulator (WTI) ($\epsilon = 2t$) boundaries with broken time reversal/ parity perturbations. The WSM phase extends with increasing perturbations (blue/filled region). Parameters used here are $\lambda_z = \lambda_{SO}$, and $b = (0.6\lambda_{SO}, 0, 0)$. This figure is taken from [26].	31

- 2.2 (Color online) (a) Oscillations in the current along the direction in which the Weyl nodes are split in the momentum space for the TR symmetry broken WSM bulk as a function of k_0L/π . The dotted lines show the theoretically predicted periodicity. The parameters used are $t = 1$, $\lambda_{SO} = \lambda_z = 0.5t$, $\epsilon = 6t$, $\mu_L = 0.3t$, $\mu_R = 0$. The inset shows the behaviour of the current in the perpendicular direction with the same parameter values. It is quite clear that this does not show any oscillations as a function of k_0L/π . (b) Spin textures of the second band in the k_x - k_z plane, with the Weyl nodes at $k = k_0\hat{z}$ and $k = -k_0\hat{z}$ indicated by red dots. Possible scattering process for a forward moving spin up electron is shown. The spin texture is symmetric under $\{k_x, \sigma_x\} \leftrightarrow \{k_y, \sigma_y\}$ 32
- 2.3 (Color online) Diagrammatic representation of the interference process. The diagram on the left shows the closed loop experienced by an electron with up spin (red line). The wall in the middle is representative of the Brillouin zone (BZ) with the holes being the only momentum values that allow low energy scattering states in the TR broken WSM bulk. The scattering processes (green arrows) at the leads take the electron from one Weyl node to the other. The diagram on the right shows the same for an electron with down spin (blue line). 34
- 2.4 (Color online) (a) Current along the direction in which the Weyl nodes are split in the WSM bulk for the inversion symmetry broken WSM as a function of k_0L/π . The dotted lines clearly indicate the predicted periodicity due to internodal scattering. The periodicity is a function of only one of the relevant momentum scales of the problem (see main text). The parameters used are $\lambda = 1$, $\mu_L = 0.1\lambda$, $\mu_R = 0$. The number of sites is kept fixed at $L = 60$. The inset shows the variation of current in the perpendicular direction for the same set of parameter values. As expected, it does not exhibit any periodicity. (b) Spin textures of the second band with the Weyl nodes indicated by red dots for the inversion symmetry broken WSM. Possible scattering process for a forward moving spin up electron is shown. The red cross indicates the absence of the corresponding process due to preservation of the orbital degree of freedom. The spin texture is symmetric under $\{k_x, \sigma_x\} \rightarrow \{k_z, \sigma_z\}$ 35
- 2.5 (Color online) Variation of current as a function of the number of lattice sites. The dashed line has a periodicity of 4 sites whereas the continuous line has a periodicity of 5 sites. The parameters used are $\lambda = 1$, $\mu_L = 0.1\lambda$, $\mu_R = 0$ 36
- 2.6 (Color online) Variation of current for different values of the scrambling parameter α . All parameters are same as that of Fig. 2.4. 37

-
- 3.1 Setup of the system. A time-reversal broken Weyl semimetal WSM of length L has been sandwiched between a superconductor (SC) with a gap Δ and a normal/WSM metal lead (N). The momentum separation between the Weyl nodes in the WSM dot is $2k_0$ and the WSM has a bias V_0 42
- 3.2 Diagrammatic representation of the possible scattering processes showing all the relevant scales. The Weyl nodes are located at $k_z = \pm k_0$ and q_{\pm} are the two possible momenta of electronic excitations above the finite potential barrier V_0 of the WSM. $\tan\theta$ denotes the Fermi velocity v_F of such excitations. I describes an incident electron and R and AR describe normal and Andreev reflected electrons and holes respectively. 43
- 3.3 (color online) A typical pattern of the current through the WSM dot oscillating with the size of the dot, with beats due to the double periodicity (a) The peaks of conduction, i.e, the map of the Andreev spectrum, appear at lengths d where $(q_+ + q_-)d/\pi$ is an integer, with $q_{\pm} = \sqrt{k_0^2 \pm 2m_W V_0}$ in red(solid) lines. The best fit to this pattern in terms of the simple two frequency function given in Eq. 3.9 with $\alpha = 2.24$ and $\beta = 0.9$ plotted in blue (dotted) lines is also shown. Note the excellent agreement between the numerical data and the formula. The parameters used are $k_0 = 1$, $m_S = m_W = 0.5$, $\mu_S = 4$, $\mu_W = 0$, $\lambda = 0.5$, $\Delta = 0.01$, $V_0 = 0.56$. (Here we only consider normal incidence). (b) Here the current integrated over the transverse momentum is shown, which also peaks at the same lengths d where $(q_+ + q_-)d/\pi$ is an integer. (c) The complete plot of the current through the WSM dot as a function of its bias voltage and its size. Other parameters used are mentioned above. 46
- 3.4 (a) Variation of the amplitude of oscillation (β) of the zero-bias conductance with the barrier height along the x axis and the ratio of the Fermi momentum and the separation of Weyl nodes along the y axis. The parameters used are $k_0 = 1$, $m_S = m_W = 0.5$, $\lambda = 0.5$, $\Delta = 0.01$. (Here we only consider normal incidence). (b) Conductance as a function of the length of the barrier along the x axis and the incident energy along the y axis at fixed $V_0 = 0.2$ 47
- 3.5 Dispersion of the inversion symmetry broken WSM along with the barrier potential V_0 . $v_{F1} = \tan(\theta_1)$ and $v_{F2} = \tan(\theta_2)$ are the Fermi velocities at q^+ and q^- respectively. 51
-

- 3.6 (color online) (a) The schematic of the procedure used for the lattice simulation. After integrating out the two leads, one superconducting and one normal metal, the full Green's function of the system, \mathcal{G} , contains the corresponding self energies. The final current through the system is obtained after averaging over the lead states, which include the information of the Fermi function of the leads (b), (c) Results of the lattice based simulation, verifying the oscillation dependence of the current as a function of V_0 and k_0 respectively. Here, the dotted lines show the periodicity expected from Eq. 3.10. The parameters used are $\Delta = 0.1$, $\epsilon = 6$, $\lambda_Z = \lambda = 0.5$, $\mu_L = 0.05$, $\mu_R = 0$. The length of the WSM dot is kept fixed at 60 in units of lattice spacing. 52
- 3.7 (a) Variation of the current as a function of the barrier height for an inversion symmetry broken WSM. The length of the Weyl semimetal is kept fixed at 100 sites. The values of the other parameters are $\lambda = 1$, $\mu_L = 0.5\Delta$ and $\mu_R = 0$. Here, $k_0 = \pi/2 - \sin^{-1}(m/\lambda)$ is kept fixed. (b) The same as a function of the separation of Weyl nodes (m is varied to change the separation of the Weyl nodes) in the Brillouin zone for fixed barrier height. The dotted lines indicate the periodicity expected from the ideas of the main text. 53
- 3.8 (Color online) The probability that an electron will be reflected as an electron ($|\chi^\pm|^2$) or as a hole ($|\eta^\pm|^2$) at a WSM-SC interface, discussed in Eq. (3.28). Note that the probability of reflection as an electron is finite. The parameters used are $\hbar^2 k_0^2 / 2m_W = 10\mu_W = 10^3\Delta = \mu_S/2$, $p \ll k_0$ and $m_S = m_W$ 54
- 3.9 The variation of the bound levels (solutions of Eq. (3.29)) near the chemical potential with the length L of the WSM for various values of θ , where $\theta = 2k_0L \bmod(2\pi)$. The parameters used are the same as in Fig. 3.8. 55
- 3.10 (Color online) The Josephson current as a function of both L and k_0 is shown at the value of $\phi \approx \pi/2$. The initial value at the origin is $(k_0, L) = (q, l)$, $ql \approx 10\pi$. The contours of constant current follow a set of (approximate) hyperbolas for constant $\theta = 2k_0L \bmod(2\pi)$, a few of which are shown in the right margin (with the minimum and the maximum current occurring near $\theta = \pi$ and $\theta = 0$ respectively). Other parameters used are the same as in Fig. 3.8. 56
- 4.1 A setup where the model we discuss can be realized. On the right side ($x > 0$), the \mathcal{N} region is modeled with spin-orbit coupled two dimensional material (say silicene). Time reversal symmetry is broken with either a complex next-nearest-neighbor hopping term or with circularly polarized light. The left side ($x < 0$), the \mathcal{S} is modeled with a proximity induced superconductor of the same material (without the radiation). 60

- 4.2 Spin asymmetry in band structure created by next-nearest-neighbor hopping as shown in Eq. (4.4). The Hamiltonian of the time reversal symmetric system with $\delta\epsilon_{\eta\sigma} = \delta\epsilon_{-\eta-\sigma}$ is shown in (a) Such symmetry is broken for finite t_2 and θ , as shown (b). The parameters used are $lE_z = 0.005t_0$ and $\lambda = 0.05t_0$ 60
- 4.3 The topological phases of the system Eq. (4.8) is shown above in (a), where the chern number of up and down spin bands are shown in parenthesis. The quantum spin-hall system is particularly marked. Periodic drive created spin asymmetry in band structure is shown in (b) and (c). The Hamiltonian of the pristine system ($\alpha = 0$), representing silicene is time reversal symmetric giving the relation $\delta\epsilon_{\sigma}^{\eta} = \delta\epsilon_{-\sigma}^{-\eta}$ among the gaps of the system. Such symmetry is broken for finite α , as shown in the right. An Andreev reflection process is allowed for an incident electron with energy E , spin σ and valley index η , only when $\epsilon \geq \max\{\delta\epsilon_{\sigma\eta}, \delta\epsilon_{-\sigma-\eta}\}$. $lE_z = 0.08$ for both (a), (b) and $\omega = 10t_0$ for (c). . . . 62
- 4.4 Top panel: The conductances of an electron in the static ($\alpha = 0$) system for various values of the staggered potential (lE_z). Out of the four channels ($\eta = \pm 1, \sigma = \pm 1$) the AR probabilities are the same for channels with same value of $\eta\sigma$. For certain values of lE_z , only two of the channels with $\eta\sigma = -1$ contribute in transport. Bottom panel: For similar values of lE_z , the driven system with $\alpha = 0.2$ and $\omega = 10t_0$, significant difference in AR probability arises, even when it remains sufficient to consider only two of the channels ($\eta\sigma = -1$). In these figures the arrows on the E axis denote the minimum gaps of the system and the minimum energies E that satisfies Eq. (4.15) are marked by circles. The parameters used are $\lambda = 0.5\Delta$, $\Delta = 0.1t_0$ 63
- 4.5 The amplitude of the difference in conductances $\sum_{\eta}(G_{\eta\downarrow} - G_{\eta\uparrow})$ plotted against E/Δ . As α increases the system develops a gap at the K and K' points and consequently with larger α , the sub-gap conductance vanishes, giving rise to zero spin-dependent value. For the choice of our parameters: $lE_z = 0.25\Delta$, $\lambda = 0.5\Delta$ and $\Delta = 0.1t_0$, the critical value of α is 0.64. The value of the driving frequency is chosen to be $\omega = 10t_0$. Surprisingly, the maximum value of the spin-dependent conductance, as a function of E/Δ (E being the incident energy) remains partly constant with α , shown in the second figure. 64
- 4.6 Appearance of spin-dependent AR in presence of both the spin-orbit coupling ($\lambda \neq 0$) and periodic driving ($\alpha \neq 0$). We plot the angle resolved sub-gap ($E/\Delta = 0.4$) conductance $f_{\eta,\sigma}(\phi_i)$ (c.f. Eq. (4.14)) as a function of the incident angle ϕ_i for all the channels available ($\eta = \pm 1, \sigma = \pm 1$), as marked individually. The resultant spin-current is plotted in dashed (red) line. Non-vanishing λ prefers two (given by $\eta\sigma = -1$) out of the four channels. Whereas, non-vanishing α prefers one valley (here, $\eta = +1$). In combination of both present, we observe spin-dependent AR. $lE_z = 0.25\Delta$, $\omega = 10t_0$ and $\Delta/t_0 = 0.1$ are kept fixed. . . 67

- 4.7 (a) The angle resolved sub-gap conductance $f_{\eta,\sigma}(\phi_i)$ is plotted as a function of the incident angle ϕ_i and the resultant spin-resolved conductance is plotted with dashed lines. Only $\eta\sigma = -1$ branches contribute for our choice of parameters: $E = 0.6\Delta$, $\lambda = 0.5\Delta$, $\Delta = 0.1t_0$, $lE_z = 0.25\Delta$. (b) Same plot for $lE_z = 0.5\Delta$. Other parameter values remain unchanged from Fig. 4.4. 68
- 4.8 The conductances of an electron when the TRS is broken by complex NNN hoppings as is shown in Eq. (4.3). The parameters taken are $t_2 = 0.005t_0$, $\theta = \pi/4$, $lE_z = 0.005t_0$, $\Delta = 0.1t_0$, $\lambda = 0.05t_0$ 69
- 5.1 Absorptive part of spin response function $\text{Im } \chi_\tau(\mathbf{q}, \omega)$ for $\mathbf{q} = 0$, chemical potential $\mu_0 = -0.49\Delta$ and $U_0 = 0.2\text{eV}$ with $\tau = +1$. Model parameters for band structure in Table I. A sharp collective mode near $\omega \approx -0.0845\Delta$ is prominent above a particle-hole continuum in the interval $-0.092 \lesssim \omega/\Delta \lesssim -0.087$ 74
- 5.2 The top panel, for $\mu_0 = -0.49\Delta$, in which there is only a single Fermi surface in the valley, has a continuum of particle-hole excitations (shown in green) below some minimum frequency. The lower panel has $\mu_0 = -0.57\Delta$ for which there are two Fermi surfaces in the valley, giving rise to the continuum modes with vanishingly small energies for $q_x > 0.4k_0$ with $k_0 = \Delta/2ta$. For both panels, $U_0 = 0.2\text{eV}$ and $\tau = +1$. Other parameters are listed in Table I. Blue lines illustrate the collective spin wave mode dispersion. 75
- 5.3 The band dispersion of Hamiltonian (5.1) showing a direct band gap E_g between the valence and the conduction band and the separation of spin polarized bands in the conduction band. Position for two of μ_0 are marked on the right margin. $k_0 = \Delta/2ta$ is the scale of momentum. The parameters used are listed in Table 1 and $\tau = +1$ 76
- 5.4 Plot of a typical $\chi(\mathbf{q}, \omega)$, Eq. (5.27), showing the particle-hole excitations of the spin-split valence bands below an energy ω_c . There is a single collective mode visible for which the real part of the denominator of Eq. (5.27) is zero. Here we have used $\mathbf{q} = \mathbf{0}$, $\mu_0 = -0.49\Delta$, $\tau = +1$ and $U_0 = 0.2\text{eV}$ 77
- 5.5 Schematic representation of the left and right hand sides of Eq. (5.37) as functions of ω , shown in red and blue respectively. For low enough k_F , an isolated spin wave mode is always present. 82
- 5.6 Spin wave excitations and the particle-hole continuum as a function of the chemical potential (μ_0) shown for three different values of the interaction strength U_0 when $\mathbf{q} = \mathbf{0}$. The blue dashed line corresponds to the mode described in Fig. 5.5. The mode corresponding to Eq. (5.40) is barely visible as a red line. The vertical lines indicate the boundary beyond which the stability condition is violated. . . 84

-
- 5.7 The blue line depicts the dispersion of the isolated spin wave excitation, ie, the ω, q_x points for which the real part of the denominator of the spin susceptibility given by Eq. (5.27) vanishes. The green continuum represents the particle-hole excitations for which the denominator of Eq. (5.27) has a nonvanishing imaginary component. Here we have taken $U_0 = 0.2\text{eV}$ 87
- 5.8 Spin susceptibility for $U_0 = 0.5\text{eV}$, $\tau = +1$ and $\mu_0 = -0.57\Delta$. Two discrete spin wave modes (indicated by arrows) are visible near $\omega = -0.055\Delta$ and $\omega = -0.092\Delta$, with the second mode very close to the continuum. However, the positivity $\omega(-\text{Im}\chi) > 0$ does not hold for all ω implying that our assumed Hartree-Fock state is not the true ground state. 89

List of Tables

5.1	Values of various parameters for MoS ₂ from Ref. [12].	74
-----	---	----

Chapter 1

Introduction

1.1 Preliminaries

1.1.1 The Dirac equation

In 1928, Paul A. M. Dirac wrote down the Hamiltonian describing relativistic spin $\frac{1}{2}$ particles[27]:

$$H = c\mathbf{p}\cdot\boldsymbol{\alpha} + mc^2\beta \quad (1.1)$$

where α_i and β obey Clifford algebra

$$\begin{aligned} \{\alpha_i, \alpha_j\} &= 2\delta_{ij}, \\ \{\alpha_i, \beta\} &= 0, \\ \beta^2 &= \mathbb{I} \end{aligned} \quad (1.2)$$

The eigenvalues of the above Hamiltonian are $E = \pm\sqrt{c^2p^2 + m^2c^4}$. In 3 + 1 dimensions, the minimal representation of α_i and β are complex 4×4 matrices. The eigenvectors are called Dirac spinors and is a four component wavefunction. This was the first successful merge of quantum mechanics and special relativity as the space and time derivatives are on the same footing in the Hamiltonian and hence in the equations of motion.

A number of variations of the Dirac equation followed. In 1929, Hermann Weyl[28] pointed out that in the $m \rightarrow 0$ limit a simplified representation exists which is block diagonal form utilizing just 2×2 Pauli matrices. It can be shown that the solutions of this Weyl equation have definite chirality. A pair of Weyl fermions with opposite chiralities can be combined to obtain a Dirac fermion. Another interesting representation was put forward by Ettore Majorana in 1937[29] which involved real numbers instead of complex numbers. The solution describes a neutral particle that was its own anti-particle.

1.1.2 Berry Phase and Chern Numbers

Let us consider a system whose Hamiltonian depends on parameters $\mathbf{R} = (R_1, R_2, \dots)$. These parameters can in general depend on time, *ie*, $\mathbf{R} = \mathbf{R}(t)$. We want to adiabatically vary $\mathbf{R}(t)$ over a path \mathcal{C} in the parameter space. We next introduce a set of instantaneous eigenfunctions $|n(\mathbf{R})\rangle$ satisfying

$$H(\mathbf{R})|n(\mathbf{R})\rangle = \epsilon_n(\mathbf{R})|n(\mathbf{R})\rangle \quad (1.3)$$

Now, if the evolution is adiabatic, if a system starts as an eigenstate $|n(\mathbf{R}(0))\rangle$, it stays an instantaneous eigenstate as the system evolves. This is known as the quantum adiabatic theorem. This means that the phase of the state is the only degree of freedom. Thus, the state at time t can be written as

$$|\psi_n(t)\rangle = e^{i\gamma_n(t)} \exp\left[-i \int_0^t dt' \epsilon_n(\mathbf{R}(t'))\right] |n(\mathbf{R}(t))\rangle \quad (1.4)$$

We insert this in the time dependent Schrödinger equation to obtain

$$i\partial_t |\psi_n(t)\rangle = H(\mathbf{R}(t)) |\psi_n(t)\rangle \quad (1.5)$$

We multiply by $\langle \psi_n(t) |$ from the left to find

$$\begin{aligned} \gamma_n &= i \int_{\mathcal{C}} d\mathbf{R} \cdot \langle \psi_n(t) | \frac{\partial}{\partial \mathbf{R}} | \psi_n(t) \rangle \\ &= \int_{\mathcal{C}} d\mathbf{R} \cdot \mathcal{A}_n(\mathbf{R}) \end{aligned} \quad (1.6)$$

The vector $\mathcal{A}_n(\mathbf{R})$ is called the Berry curvature or the Berry vector potential and is gauge dependent. Under the gauge transformation

$$|n(\mathbf{R})\rangle \rightarrow e^{i\zeta(\mathbf{R})} |n(\mathbf{R})\rangle \quad (1.7)$$

where $\zeta(\mathbf{R})$ is an arbitrary smooth function, the Berry curvature transforms as

$$\mathcal{A}_n(\mathbf{R}) \rightarrow \mathcal{A}_n(\mathbf{R}) - \frac{\partial}{\partial \mathbf{R}} \zeta(\mathbf{R}). \quad (1.8)$$

Now, for a closed contour in the parameter space, *ie*, for $\mathbf{R}(T) = \mathbf{R}(0)$, due to single valuedness of the wavefunctions, we must impose

$$\zeta(\mathbf{R}(T)) - \zeta(\mathbf{R}(0)) = 2\pi \times \text{integer}. \quad (1.9)$$

This shows that for a closed contour, γ_n only changes by an integer multiple of 2π under gauge transformations and thus, cannot be removed. This gauge invariant physical quantity is

called the Berry phase [30] and is given by

$$\gamma_n = \oint_{\mathcal{C}} d\mathbf{R} \cdot \mathcal{A}_n(\mathbf{R}). \quad (1.10)$$

In analogy to electrodynamics, it is useful to define the gauge invariant Berry curvature or Berry flux

$$\Omega_{\mu\nu}^n(\mathbf{R}) = \frac{\partial}{\partial R^\mu} \mathcal{A}_\nu^n(\mathbf{R}) - \frac{\partial}{\partial R^\nu} \mathcal{A}_\mu^n(\mathbf{R}). \quad (1.11)$$

For a three dimensional parameter space, this can be recast into

$$\begin{aligned} \boldsymbol{\Omega}_n &= \nabla_{\mathbf{R}} \times \mathcal{A}_n(\mathbf{R}) \\ \gamma_n &= \int_S d\mathcal{S} \cdot \boldsymbol{\Omega}_n \end{aligned} \quad (1.12)$$

where S is any arbitrary surface enclosed by \mathcal{C} .

1.1.3 Role of Berry phase in condensed matter physics

Condensed matter physics deals with lattices with periodic potential for which the Hamiltonian H has a period \mathbf{a} in the real space such that

$$H(\mathbf{r}) = H(\mathbf{r} + \mathbf{a}). \quad (1.13)$$

Bloch's theorem states that the eigenfunctions of such a system can be written as

$$|\psi_{n\mathbf{k}}(\mathbf{r})\rangle = e^{i\mathbf{k}\cdot\mathbf{r}} |u_{n\mathbf{k}}(\mathbf{r})\rangle \quad (1.14)$$

where $|u_{n\mathbf{k}}(\mathbf{r})\rangle$ has the same periodicity as the crystal lattice with $|u_{n\mathbf{k}}(\mathbf{r})\rangle = |u_{n\mathbf{k}}(\mathbf{r} + \mathbf{a})\rangle$. The $|u_{n\mathbf{k}}(\mathbf{r})\rangle$ s are the eigenstates of the Bloch hamiltonian $\mathcal{H}(\mathbf{k}) = e^{-i\mathbf{k}\cdot\mathbf{r}} H(\mathbf{r}) e^{i\mathbf{k}\cdot\mathbf{r}}$ so that

$$\mathcal{H}(\mathbf{k}) |u_{n\mathbf{k}}(\mathbf{r})\rangle = \epsilon_{n,\mathbf{k}} |u_{n\mathbf{k}}(\mathbf{r})\rangle. \quad (1.15)$$

The energy eigenvalues are periodic in \mathbf{k} with

$$\epsilon_{n,\mathbf{k}} = \epsilon_{n,\mathbf{k}+\mathbf{G}} \quad (1.16)$$

where \mathbf{G} is the periodicity of a reciprocal lattice vector.

The wave functions $|u_{n\mathbf{k}}(\mathbf{r})\rangle$ depend parametrically on \mathbf{k} . This means that if \mathbf{k} is changed adiabatically (by application of an electric field for example), Berry phase would play a crucial role.

In the situation when the space has no boundary (for example torus, sphere), one can show

[31] that the integration of the Berry curvature is quantised. This is the case for lattice systems as the momenta lie on a d dimensional torus. So, we can write

$$\frac{1}{(2\pi)^d} \int_{BZ} d^d k \, \Omega_n \cdot \hat{n} = c_n \quad (1.17)$$

where c_n is known as the first Chern number corresponding to the n -th band and as already mentioned, is an integer. c_n characterizes the topological structure of the mapping from the BZ to the Hilbert space, *ie*, from \mathbf{k} to $|u_{n\mathbf{k}}(\mathbf{r})\rangle$.

1.2 Dirac Materials

In several solid state systems, one would naively expect the low energy excitations to have exclusively non-relativistic description. However, the presence of periodic potential in a crystal dresses the electronic states and in some cases, the emergent low energy band structure most resembles the Dirac equation. These materials are quite different from electrons and holes described by the Schrödinger equations. When $m \rightarrow 0$, the difference is quite obvious as the Dirac fermions have gapless spectrum with a linear dispersion. Even when $m \neq 0$, the electrons and holes in the Dirac equation share the same spinor space and have the same effective mass m . However, particles and holes obeying the Schrödinger equation can have different effective masses. Another interesting feature is the fact that since these Dirac materials are low energy emergent phases, strict restrictions of Lorentz symmetry need not be obeyed always.

The most well known example is that of Graphene which hosts a gapless spectrum and is described by a 2×2 dimensional representation of the Dirac equation. Similar massless spectra are observed in other systems like surface states of topological insulators, d -wave superconductors, Weyl semimetals etc. Transport properties and response functions of such systems are typically governed by the low energy spectrum and are hence universal despite the materials themselves being quite different from each other. Other examples include systems such as Silicene and transition metal dichalcogenides where the low energy excitations are described by the massive Dirac equation.

1.2.1 Graphene

Two-dimensional materials based on honeycomb lattices have become a subject of intense investigation in the past few years, due to their interesting band structure and associated topological properties. The paradigm of this is realized in graphene, a pure carbon honeycomb lattice, which hosts a gapless spectrum with Dirac points at the K and K' points in the Brillouin zone [24] due to a combination of inversion and time-reversal symmetry, as well as the very weak spin-orbit coupling (SOC) typical of light elements.

The honeycomb lattice of Graphene is shown in Fig. 1.1(a). Here, A and B are the two

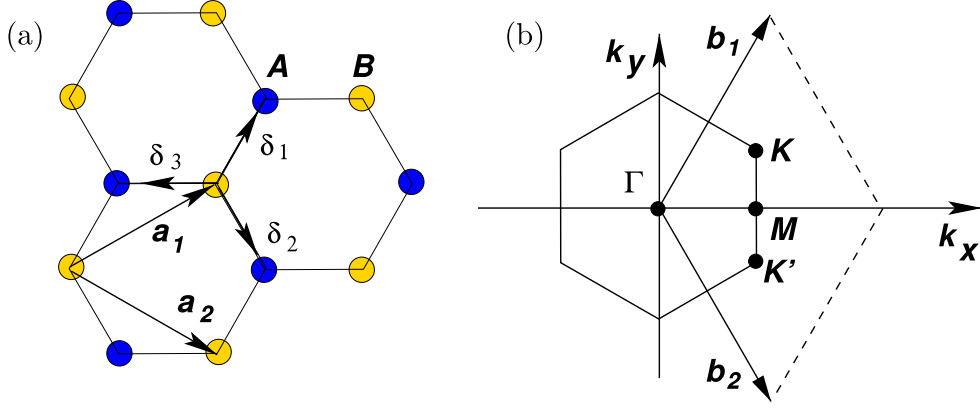


Figure 1.1: (a) Graphene is a two dimensional honeycomb lattice composed of carbon atoms. \mathbf{a}_1 and \mathbf{a}_2 are the unit lattice vectors and δ_i are vectors connecting the nearest neighbour atoms. (b) The hexagonal Brillouin Zone of Graphene. \mathbf{b}_1 and \mathbf{b}_2 are the reciprocal lattice vectors. This figure is taken from [24].

inequivalent lattice sites. The corresponding tight binding Hamiltonian is:

$$H = -t \sum_{\langle ij \rangle} a_{\sigma,i}^\dagger b_{\sigma,j} + h.c. \quad (1.18)$$

where $a_{\sigma,i}$ ($b_{\sigma,i}$) is the electronic operator on A (B) sublattice on site \mathbf{R}_i . The nearest neighbouring sites are connected by the vectors δ_i with $\delta_1 = \frac{a}{2}(1, \sqrt{3})$, $\delta_2 = \frac{a}{2}(1, -\sqrt{3})$, $\delta_3 = a(-1, 0)$.

Fourier transforming this Hamiltonian, we obtain:

$$H = \sum_{\mathbf{k}} \Psi_\sigma^\dagger(\mathbf{k}) h_\sigma(\mathbf{k}) \Psi_\sigma(\mathbf{k}) \quad (1.19)$$

where, $\Psi_\sigma(\mathbf{k}) = [a_\sigma(\mathbf{k}), b_\sigma(\mathbf{k})]^T$ is the pseudo-spin basis and

$$h_\sigma(\mathbf{k}) = \begin{bmatrix} 0 & f(\mathbf{k}) \\ f^*(\mathbf{k}) & 0 \end{bmatrix} \quad (1.20)$$

with, $f(\mathbf{k}) = -t \sum_i e^{i\mathbf{k} \cdot \delta_i}$. The energy eigenvalues corresponding to the above Hamiltonian is given by $E(\mathbf{k}) = \pm |f(\mathbf{k})|$. This spectrum is gapless at two points at the corners of the graphene BZ. Their position is given by

$$\mathbf{K} = \left(\frac{2\pi}{3a}, \frac{2\pi}{3\sqrt{3}a} \right), \mathbf{K}' = \left(\frac{2\pi}{3a}, -\frac{2\pi}{3\sqrt{3}a} \right). \quad (1.21)$$

As shown in Fig. 1.2, the spectrum can be expanded near the \mathbf{K} and \mathbf{K}' points and about these two points, the linearized Hamiltonian can be written as

$$h_\sigma(\mathbf{K}' + \mathbf{q}) = v_F \mathbf{q} \cdot \boldsymbol{\tau} \quad \text{and} \quad h_\sigma(\mathbf{K} + \mathbf{q}) = h_\sigma^*(\mathbf{K}' + \mathbf{q}) \quad (1.22)$$

where, τ_i are Pauli matrices written in the pseudo-spin basis and $v_F = \frac{3at}{2}$. Thus we end up with the two dimensional Dirac equation. One feature quite apparent in the above linearized Hamiltonian is the fact that the pseudo-spin and momentum are locked unlike normal metal. The eigenvalues and eigenvectors of the Hamiltonian $h_\sigma(\mathbf{K}' + \mathbf{q})$ is given by

$$E(\mathbf{q}) = \pm v_F |\mathbf{q}|, \quad \psi_{\mathbf{q}}^{\pm}(\mathbf{r}) = \frac{1}{\sqrt{2}} e^{i\mathbf{q}\cdot\mathbf{r}} (e^{i\theta_{\mathbf{q}}/2}, e^{-i\theta_{\mathbf{q}}/2})^T. \quad (1.23)$$

where $\theta_{\mathbf{q}}$ is the angle the planar vector \mathbf{q} makes with respect to the x-axis.

The Dirac nodes in graphene is protected by the presence of inversion symmetry, *ie*, the absence of any terms in the Hamiltonian $\propto \tau_z$. Any such perturbation would have anticommuted with the Hamiltonian and ended up opening a gap in the spectrum.

It is easy to see that under $\mathbf{k} \rightarrow -\mathbf{k}$, the pseudo-spin spinor part of the wave function becomes orthogonal[1]. This prevents intra-nodal backscattering as long as the scattering potential has no off-diagonal components in the pseudo-spin space. Experimentally, measurement of local density of states around impurities display supression of interference patterns corresponding to such processes[32]. However, internodal backscattering processes are not suppressed by such selection rules and are necessary to explain interference patterns.

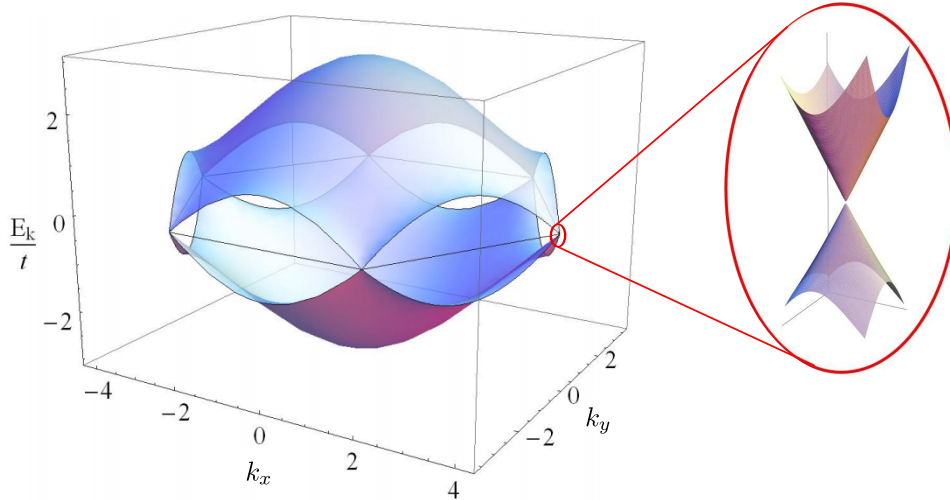


Figure 1.2: The energy spectrum of the tight binding model of graphene. About the gapless points in the BZ, the energy dispersion is linear. This figure is taken from [24].

1.2.1.1 Haldane model

Historically, the first example of Chern insulator on honeycomb lattice was given by Haldane[33]. A second term is added to describe next-nearest-neighbour (NNN) hopping from *A*-to-*A* and *B*-to-*B* hopping. Additionally, a periodic local magnetic field is added to break time-reversal symmetry. This magnetic field can be chosen to have zero total flux through the unit cell.

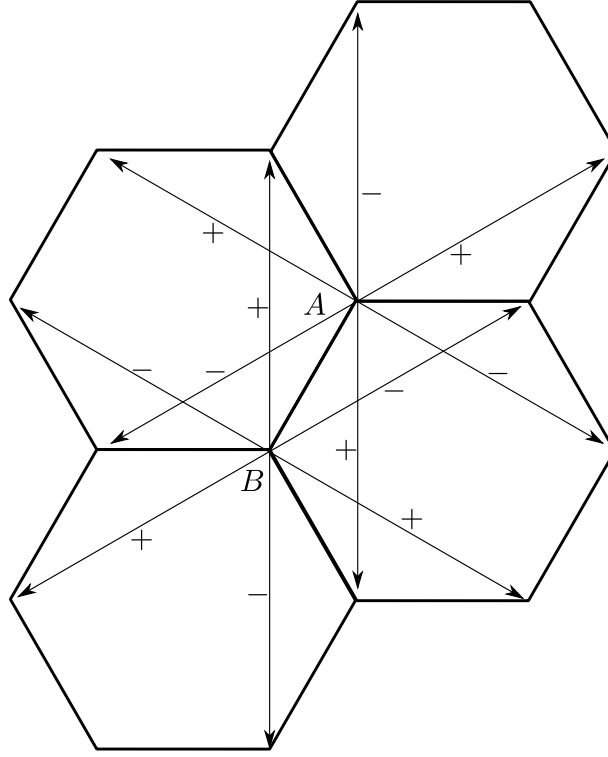


Figure 1.3: The solid lines denote the nearest neighbour bonds whereas the dashed lines show the NNN bonds. $\nu_{ij} = \pm$ signs give us the phase convention for the Haldane model.

The easiest way of introducing this is by putting magnetic phases on NNN terms as shown in Fig. (1.3). Nearest neighbour terms remain unaffected as closed paths of such processes enclose the complete unit cells and hence no net flux. Lastly, a staggered mass term is added to explicitly break the inversion symmetry.

The Hamiltonian can be written as

$$H = t \sum_{\langle ij \rangle} a_{\sigma,i}^\dagger b_{\sigma,j} + t_2 \sum_{\langle\langle ij \rangle\rangle} e^{i\nu_{ij}\phi} c_{\sigma,i}^\dagger c_{\sigma,j} + M \sum_i (a_{\sigma,i}^\dagger a_{\sigma,i} - b_{\sigma,i}^\dagger b_{\sigma,i}) \quad (1.24)$$

where the annihilation operator c can be either a or b and ν_{ij} can be chosen according to Fig. (1.3). The low energy model near the Dirac points can be obtained after some algebra to be

$$h_\sigma(\mathbf{K} + \mathbf{q}) = -3t_2 \cos(\phi) + v_F \mathbf{q} \cdot \boldsymbol{\tau} + (M - 3\sqrt{3}t_2 \sin(\phi)) \sigma_z \quad (1.25)$$

and

$$h_\sigma(\mathbf{K}' + \mathbf{q}) = -3t_2 \cos(\phi) + v_F \mathbf{q} \cdot \boldsymbol{\tau}^* + (M + 3\sqrt{3}t_2 \sin(\phi)) \sigma_z. \quad (1.26)$$

The total Chern number of the Haldane model can be computed to be $C = \frac{1}{2}[\text{sgn}(M_+) - \text{sgn}(M_-)]$ where $M_\eta = M - 3\sqrt{3}\eta t_2 \sin(\phi)$.

1.2.2 Silicene

Another two dimensional material is silicene which is a two dimensional allotrope of silicon with the atoms arranged on a hexagonal lattice. Unlike graphene, silicene has a periodically buckled topology due to the relatively larger size of the Si atoms. This is modelled by a staggered onsite potential with opposite signs on opposite sublattice sites. Also, compared to graphene, silicene has significantly stronger spin-orbit coupling. These two features lead to adding a term $\propto \tau_z$ in the Hamiltonian which leads to a gapped low energy spectrum about the K and K' points. This band gap can be tuned by application of an electric field perpendicular to the sample, by a biaxial strain[10] or by oxidation[9]. This makes silicene a good candidate for monolayer topological insulators[11].

1.2.3 Transition Metal Dichalcogenides(TMDs)

Transition metal dichalcogenide (TMD) monolayers, where a transition metal M (e.g., Mo or W) resides on one sublattice and a dimer of chalcogen X atoms (e.g., S, Se) on the other, have recently emerged as another set of important materials in the class of two-dimensional materials based on honeycomb lattices [34, 35]. These systems are gapped at the K and $K' = -K$ points due to broken inversion symmetry. The strong SOC associated with M atoms leads to very interesting spin-valley coupling near these points [36, 37]. In particular, one finds spin up and down components of the valence band well-separated in energy, with their ordering interchanged for the two valleys. This is shown in Fig 1.4. This allows for an effective valley polarization to be induced when the system spin polarizes via pumping with circularly polarized light [38–40]. The coupling of spin and valley in this way has been dramatically demonstrated via the observation of a valley Hall effect in this circumstance [41].

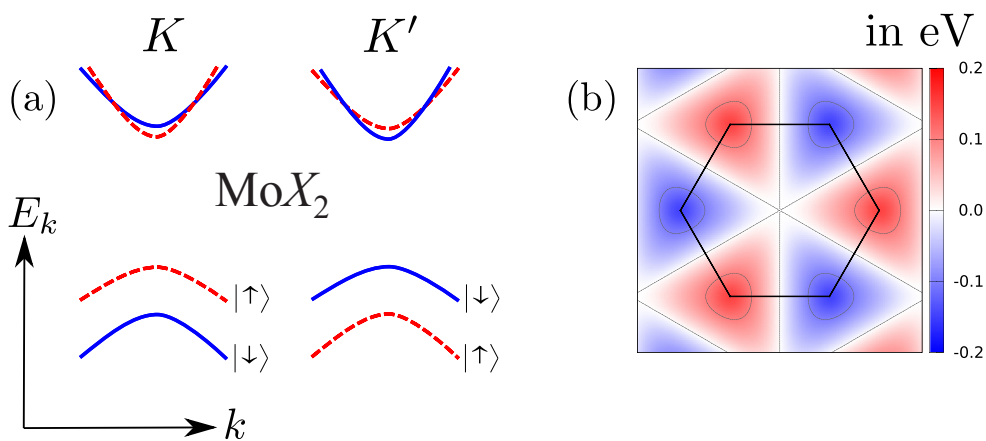


Figure 1.4: (a) The conduction and the spin-split valence bands near the band edges near the K and K' points of the BZ. (b) Strength of the spin-orbit coupling of the valence band in eV. This figure is taken from [8].

The locking of spin and valley degrees of freedom in TMD monolayers is a unique feature

of these materials. When hole-doped, it leads to a non-zero expectation value of $\sigma_z \tau_z$, where σ_z a Pauli matrix for spin, and τ_z the analogous operator for the valley index. This occurs without any interaction present in the Hamiltonian, yet is reminiscent of ferromagnetic ordering, albeit without time-reversal symmetry-breaking since this reverses both spin and valley.

1.2.4 Weyl Semimetals

Weyl semimetals (WSMs) are 3D topological systems with an even number of Weyl nodes in the BZ where the conduction and the valence bands touch. About these points, the dispersion is linear and the low energy physics is governed by the anisotropic Weyl equation[13]

$$H = \sum_i v_i (\hat{\mathbf{n}}_i \cdot \mathbf{p}) \sigma_i \quad (1.27)$$

where v_i are the anisotropic velocities and $\hat{\mathbf{n}}_i$ are the principal directions and σ_i are Pauli matrices which can describe either spin or some other internal degree of freedom. The low-energy excitations having a definite chirality $\kappa = \text{sign}[\hat{\mathbf{n}}_1 \cdot (\hat{\mathbf{n}}_2 \times \hat{\mathbf{n}}_3)]$.

It is necessary to point out a few things to emphasize the topological nature of WSMs. Firstly, it is easy to see that the WSM phase is protected against small perturbations. This is because the low energy Hamiltonian is already a linear combination of all the three Pauli matrices. Any perturbation in the same basis can also be necessarily expressed in terms of Pauli matrices. Consequently, all that the perturbations are allowed to do is to change the position of the Weyl nodes in the BZ. Secondly, it can be shown[42] that in the 3D BZ, Weyl nodes always occur in pairs with opposite chiralities; this is known as the Nielsen-Ninomiya theorem.

The Berry flux is identically zero throughout the BZ in the presence of both inversion and time reversal symmetries(TRS). Hence, to obtain Weyl nodes, it is necessary to break either of these symmetries. The minimal model for a TRS broken WSM has two nodes whereas an inversion symmetry broken WSM with TRS is required to have four nodes.

1.2.4.1 Sources of Berry Flux

Let us consider the simplest possible model for a two node WSM with nodes at $\mathbf{k} = (\pm k_0, 0, 0)$ with chirality $\kappa = \pm 1$. The Hamiltonian can then be written as

$$H^\kappa = \kappa v \mathbf{p} \cdot \boldsymbol{\sigma} \quad (1.28)$$

where $\mathbf{p} = (k_x + \kappa k_0, k_y, k_z)$

Wavefunction of the filled band near the Weyl point is given by

$$\psi(\theta, \phi) = \frac{1}{\sqrt{2}} \begin{bmatrix} -\frac{\sin\theta}{\sqrt{1+\kappa\cos\theta}} e^{-i\phi} \\ \sqrt{1+\kappa\cos\theta} \end{bmatrix} \quad (1.29)$$

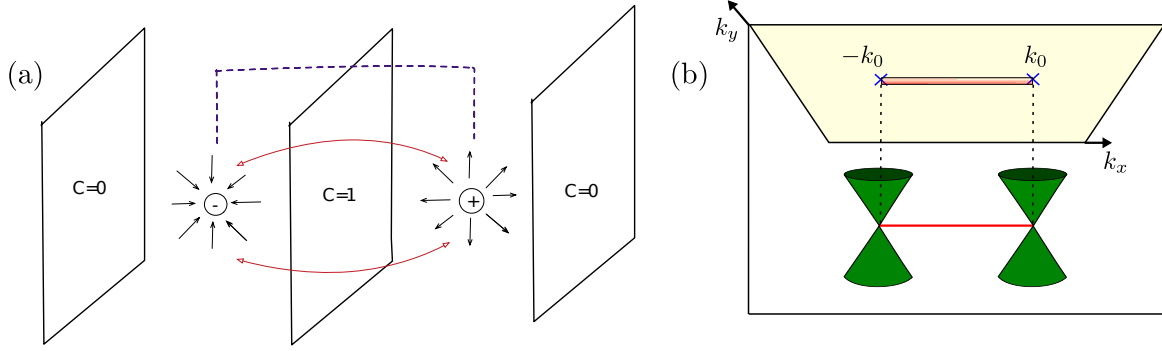


Figure 1.5: (a) The 2D planes between the two Weyl nodes can be thought of integer quantum hall systems with non-vanishing Chern number. (b) The Fermi arcs lie within the projections of the Weyl nodes on the surface BZ. The red line on the surface BZ (k_x-k_y plane) indicates a nonzero LDOS due to the Fermi arc states whereas the yellow plane indicates zero LDOS. Both figures are taken from [25].

where θ and ϕ are the polar and azimuthal angle corresponding to the vector \mathbf{p} . The Berry flux, integrated over a small sphere about the Weyl nodes is equal to $2\pi\kappa$. This is true for any surface enveloping the Weyl nodes. Thus, the nodes can be thought of as magnetic monopoles with their flux associated with the quantized charge at the nodes.

This, coupled with the Nielsen-Ninomiya theorem, shows that the only way the WSM phase can be destroyed is by merging two Weyl nodes with opposite chiralities together.

1.2.4.2 Surface states

WSMs host topologically protected surface states even though the bulk itself is gapless. Instead of closed surfaces, the surface states form open Fermi arcs that connect the projections of the Weyl nodes on the surface BZ. This is surprising as typically, it is expected that the bulk has to be gapped to prevent the hybridisation of the surface and the bulk states. This is what is seen in topological insulators for example. However, in case of WSMs, as the nodes themselves act as sources or sinks of Berry flux, the 2D layers between the two Weyl nodes have non-vanishing Chern number and effectively are integer quantum hall systems with edge states[25]. The Fermi arcs are the collection of such edge states. This is demonstrated in Fig. 1.5.

1.2.4.3 Different types of WSM

One could always add a term $\propto f(\mathbf{p})\mathbb{I}$ in Eq. 1.28 where $f(\mathbf{p})$ is any function that goes to zero at the Weyl nodes. This does not destroy the WSM phase nor does it change the location of the nodes. However, the tilt of the dispersion changes. In principal, this tilt angle could so large that touching electron and hole pockets are produced instead of point-like Fermi surface that was previously present. This type of WSM are known as type II WSM and are predicted to occur in WTe_2 [43].

Another class of WSM that have recently become quite relevant are multi-Weyl semimetals.

These are WSMs with linear dispersion along one direction and quadratic or cubic dispersion in the perpendicular directions[44]. Such systems are protected by point group symmetry of the lattice.

1.3 Structure of the thesis

The thesis deals with transport and collective modes in Dirac materials. In chapter 2 we start with the simplest TRS broken WSM with two nodes and study transport through the same by explicitly constructing a lattice model and attaching two normal leads on either side via self energy terms. A small chemical potential is maintained between the leads and the separation between the Weyl nodes ($2k_0$) is varied and the current is calculated. We demonstrate that the nature of the current depends on the spin texture of the low energy states around the Weyl nodes. We do the same analysis for the minimal inversion symmetry broken WSM with four nodes. We next study, in Chapter 3, Andreev spectroscopy in a WIS geometry where W is a pristine WSM, I is a WSM with a barrier potential and S is a s -wave superconductor. In the same chapter, we briefly look at the Josephson effect through a TRS broken WSM and show that the critical current actually changes sign and undergoes a $0 - \pi$ transition as a consequence of the same spin texture. Next, we explore the possibility of obtaining spin dependent Andreev reflection for a two dimensional system with strong spin orbit coupling when the TRS is broken in chapter 4. And lastly, in chapter 5 we study spin waves in a TMD monolayer using the time dependent Hartree-Fock approximation(TDHFA).

Momentum space interferometry in Weyl semi-metals

In this chapter we study the low energy transport of a Weyl semimetal sandwiched between two *normal leads*. Here, as we elaborate later, the spin texture and the chirality of the excitations play a crucial role. In fact, we show that for a TRS broken WSM (with two Weyl points), the current for a fixed chemical potential difference, oscillates as a function of $\delta k L$ where δk is the separation of the Weyl nodes in the BZ and L is the size of the system in real space.

There have been several experimental and theoretical studies[45–49] of spin textures in topological insulators (TIs)[6, 50] and in other Dirac materials[1]. However, much less attention has been paid to the study of the emergent pseudo-spin or orbital degree of freedom that appears in many of these materials. A notable exception is the work by Roy *et al*[51, 52], which showed that the surface states of three dimensional topological insulators are ferromagnetic in terms of this orbital pseudo spin. They also showed that as a physical consequence, tunneling between two surfaces can be suppressed by a mismatch of the orbital pseudo spin even when the other physical degrees of freedom allow tunneling.

For a time-reversal symmetry breaking WSM whose minimal model has just two Weyl nodes, the identification of the scale δk is obvious, but for a time-reversal invariant, inversion symmetry broken WSM, the minimal model has four Weyl nodes. Hence, naively the identification of δk is not obvious. However, we shall see that analogous to the behaviour in topological insulators, orbital pseudo spin conservation comes to the rescue. Unlike the spin whose polarization is tied to the direction of motion of the quasi-particle, the polarization of the orbital pseudo-spin turns out to be independent of the momentum in the inversion symmetry broken WSM. Hence, conservation of pseudo spin, allows for scattering only between a single pair of Weyl nodes, and we show that we get $\delta k L$ oscillations for an appropriate δk even for inversion symmetry broken WSMs.

This chapter is divided into several sections. In section 2.1, we introduce the TRS broken WSM model and we calculate the current as a function of the internodal distance in the NWN

geometry for a fixed chemical potential difference across the sample. We demonstrate the periodic oscillations and provide the mechanism behind the same. In section 2.2, we repeat the same process for an inversion symmetry broken WSM and introduce additional selection rules which dictate the scattering processes as TRS is preserved. Lastly, in section 2.3, we discuss the robustness of these oscillations and propose experimental setups that could probe into this kind of transport.

2.1 Time-reversal broken WSM

In this section, we will study the current through a junction of a TRS breaking WSM of length L between two normal leads.

The WSM is modeled by the standard Hamiltonian for a three dimensional topological insulator in the Bi_2Se_3 class with a time-reversal perturbation(b_z) added to make it a WSM [26, 53] -

$$H_0 = \epsilon_k \tau_x - \lambda_z \sin k_z \tau_y - \lambda \tau_z (\sigma_x \sin k_y - \sigma_y \sin k_x) + b_z \sigma_z, \quad (2.1)$$

where $\epsilon_k = \epsilon - 2t \sum_i \cos k_i$ is the kinetic energy, τ represents the orbital (pseudo-spin) degree of freedom, σ represents the spin and λ, λ_z are the strengths of the spin-orbit coupling.

This is a 4 band model where, in the limit where $\lambda_z \ll \epsilon - 6t \ll b_z$, the two middle bands touch at $(0, 0, \pm k_0)$ forming a pair of Weyl nodes. Here, k_0 is defined via $tk_0^2 = b_z - \epsilon + 6t$, and the top-most and lower most bands are far from the touching point and can be ignored at low energies. Thus the model reduces to the the two band model studied in detail in Ref.[54]. We provide details of this derivation in section 2.1.1.

The phase diagram of this model is given in Fig. (2.1).

To compute the current, we will use the lattice version of this four band model. We choose the chemical potential μ_W (measured from the Weyl node) to be sufficiently small, so that the states belonging to the two Weyl nodes are well-separated. Note that our choice of the Weyl nodes along the k_z axis implies that the surface states for this model appear on the surfaces perpendicular to the x or y axes. We will compute current through the WSM both along the z direction, which is the direction of the separation of the Weyl nodes and along the x direction which is perpendicular to the separation. We will compute it explicitly using the lattice version of Eq.2.1 using the Green's function technique. The Green's function for the isolated Weyl semimetal is constructed as $G_W(\omega) = (\omega - H_W)^{-1}$. The two leads on either side of the WSM are coupled via self-energy terms in the full Green's function. Since the attached leads are expected to have very large bandwidths compared to that of the WSM, these self energies are taken to be constant matrices diagonal in the σ and τ indices. The full Green function is then given by

$$G(\omega) = (G_W^{-1} - \Sigma_L - \Sigma_R)^{-1}. \quad (2.2)$$

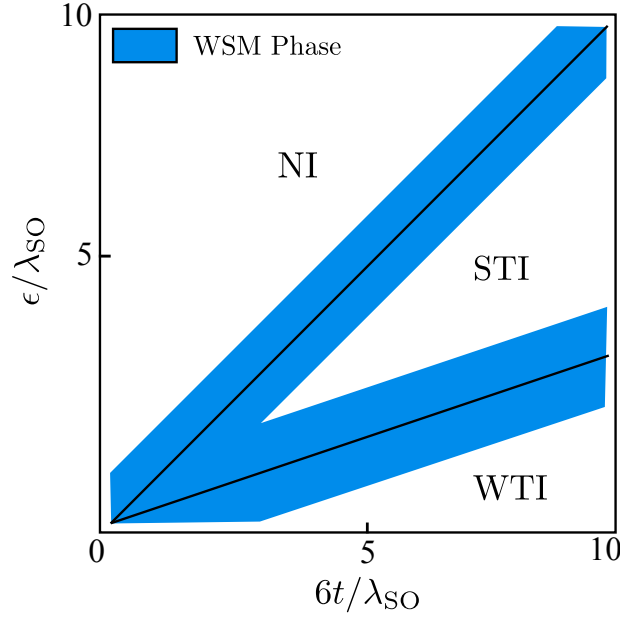


Figure 2.1: A typical phase diagram of our model system. The Weyl semi-metal (WSM) phase appears at the strong topological insulator (STI), normal insulator (NI) ($\epsilon = 6t$) and strong topological insulator (STI), weak topological insulator (WTI) ($\epsilon = 2t$) boundaries with broken time reversal/ parity perturbations. The WSM phase extends with increasing perturbations (blue/filled region). Parameters used here are $\lambda_z = \lambda_{SO}$, and $b = (0.6\lambda_{SO}, 0, 0)$. This figure is taken from [26].

Here $\Sigma_j = -i\tilde{t}_j^2\pi\delta_{\sigma,\sigma'}\delta_{\tau,\tau'}$ with \tilde{t}_j being the hopping amplitude from the Weyl semimetal to the j^{th} lead. The current is then obtained as [18]

$$\langle J \rangle = \frac{2\pi e}{\hbar^2} \int d\omega \text{Tr}[G^\dagger(\omega)\Gamma_R G(\omega)\Gamma_L](f_R(\omega) - f_L(\omega)). \quad (2.3)$$

Here $\Gamma_j = i(\Sigma_j - \Sigma_j^\dagger)$ and f_j is the Fermi function of the j^{th} lead.

In Fig.2.2(a), we show that the current with fixed bias, when measured along the z direction shows oscillations as a function of k_0L , whereas no oscillations are seen in the x direction as shown in the inset of Fig.2.2(a). It is to be noted here that in the transverse direction, most of the contribution to the current comes from oblique incidence due to the presence of the low energy states near the Weyl nodes at $(0, 0, \pm k_0)$. As the dispersion near $(k_x, 0, 0)$ is gapped, normal incidence will have vanishingly small contribution to the low energy transport properties of the bulk. The assumption here is that the leads are sufficiently large in the y and z directions so that k_y and k_z are good quantum numbers.

2.1.1 Low energy subspace

In order to explain the oscillations, we first compute the spin texture of the low energy bands near the two nodes.

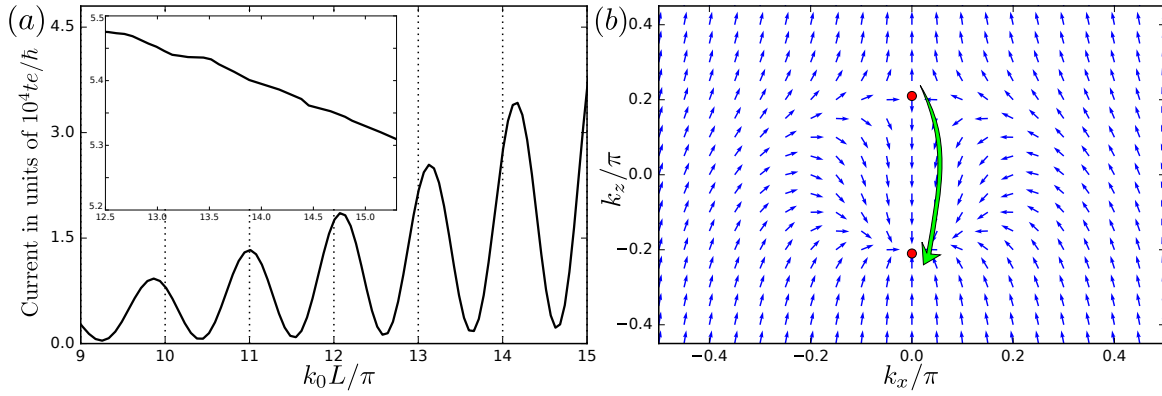


Figure 2.2: (Color online) (a) Oscillations in the current along the direction in which the Weyl nodes are split in the momentum space for the TR symmetry broken WSM bulk as a function of $k_0 L / \pi$. The dotted lines show the theoretically predicted periodicity. The parameters used are $t = 1$, $\lambda_{SO} = \lambda_z = 0.5t$, $\epsilon = 6t$, $\mu_L = 0.3t$, $\mu_R = 0$. The inset shows the behaviour of the current in the perpendicular direction with the same parameter values. It is quite clear that this does not show any oscillations as a function of $k_0 L / \pi$. (b) Spin textures of the second band in the k_x - k_z plane, with the Weyl nodes at $k = k_0 \hat{z}$ and $k = -k_0 \hat{z}$ indicated by red dots. Possible scattering process for a forward moving spin up electron is shown. The spin texture is symmetric under $\{k_x, \sigma_x\} \leftrightarrow \{k_y, \sigma_y\}$.

We begin by identifying the low energy subspace of this four band model.

$$H_0 = \epsilon_k \tau_x - \lambda_z \sin k_z \tau_y - \lambda \tau_z (\sigma_x \sin k_y - \sigma_y \sin k_x) + b_z \sigma_z.$$

We divide the Hamiltonian into three parts:

$$\begin{aligned} h_1 &= \epsilon_k \tau_x - \lambda_z \sin k_z \tau_y \\ h_2 &= -\lambda \tau_z (\sigma_x \sin k_y - \sigma_y \sin k_x) \\ \text{and } h_3 &= b_z \sigma_z. \end{aligned}$$

We diagonalise h_1 using the unitary operator:

$$U = \frac{1}{\sqrt{2}} \begin{pmatrix} \mathbb{I} & \mathbb{I} \\ e^{i\phi} \mathbb{I} & -e^{i\phi} \mathbb{I} \end{pmatrix}, \quad (2.4)$$

where $\phi = -\tan^{-1}(\lambda_z \sin k_z / \epsilon_k)$. Here, the unit matrix \mathbb{I} is in the spin space. Hence,

$$U^\dagger h_1 U = r(\mathbf{k}) \tau_z \mathbb{I}_\sigma \quad (2.5)$$

where, $r(\mathbf{k}) = (\epsilon_k^2 + (\lambda_z \sin k_z)^2)^{1/2}$. The second part of the Hamiltonian h_2 , under this unitary operation, takes the form:

$$U^\dagger h_2 U = -\lambda \tau_x (\sigma_x \sin k_y - \sigma_y \sin k_x)$$

(2.6)

Lastly, the third term of the Hamiltonian does not change because it involves only σ matrices.

Hence, the full Hamiltonian, under the action of U becomes:

$$H_U = U^\dagger H_0 U = \begin{pmatrix} r(\mathbf{k})\mathbb{I} + b_z\sigma_z & -\lambda(\sigma_x \sin k_y - \sigma_y \sin k_x) \\ -\lambda(\sigma_x \sin k_y - \sigma_y \sin k_x) & -r(\mathbf{k})\mathbb{I} + b_z\sigma_z \end{pmatrix}.$$

When $k_x = k_y = 0$, H_U becomes quite trivial and it is easy to identify the low energy subspace to be the one with a relative sign difference between r and b_z , ie, the middle 2×2 block. This gives us the low-energy Hamiltonian:

$$H_L = \begin{pmatrix} r(\mathbf{k}) - b_z & -\lambda(\sin k_y - i \sin k_x) \\ -\lambda(\sin k_y + i \sin k_x) & -r(\mathbf{k}) + b_z \end{pmatrix}. \quad (2.7)$$

This Hamiltonian will have Weyl nodes at $\mathbf{k}_0 = (0, 0, \pm k_0)$ where $k_0 = \cos^{-1}\left(\frac{4t^2 - \sqrt{(4t^2 - \lambda_z^2)b_z^2 + \lambda_z^4}}{4t^2 - \lambda_z^2}\right)$.

2.1.2 Spin preserving selection rule

Near the Weyl nodes, the low energy Hamiltonian Eq.(2.7) can be written as

$$H_{\text{WSM}} = \epsilon_k \tilde{\sigma}_z + \lambda(k_x \tilde{\sigma}_x + k_y \tilde{\sigma}_y). \quad (2.8)$$

Here $\epsilon_k = (\hbar^2/2m_W)(k_x^2 + k_y^2 + k_z^2 - k_0^2)$ is the kinetic energy and m_W is the effective mass and we have chosen the effective spin $\tilde{\sigma} = -\sigma$, in terms of the spin of the original Hamiltonian. Note that the orbital pseudo spin is no longer a good quantum number in this effective model. Also note that this model, when projected to the low energy subspace, breaks inversion symmetry[55]. In the lattice model, we have computed the spin textures of the lower (filled) band of the two middle bands of the 4 band model and as can be seen in Fig.2.2(b), the spin texture at $k = k_0$ is not opposite to the spin texture at $k = -k_0$. Thus, in terms of the two dimensional low energy reduced subspace, the Hamiltonian for the model is given by

$$H = v_x k_x \tilde{\sigma}_x + v_y k_y \tilde{\sigma}_y + s v_z k_z \tilde{\sigma}_z \quad (2.9)$$

where $v_x = \lambda$, $v_y = \lambda$ and $v_z = \hbar^2 k_0 / m_W$, $\tilde{\sigma}_i$ are the effective two component spins and $s = \pm 1$ for the two nodes. We also note that although the spin textures are not opposite, the topological quantum numbers as computed either as the sign of the product of the three velocities ($sv_x v_y v_z$) or from the integrated Berry curvature ($2\pi s$) around the nodes is clearly opposite for the two nodes.

We can now easily understand the oscillations in $k_0 L$ by using the scattering matrix formalism in the reduced two band model. We restrict ourselves to small μ_W , so that the two Weyl

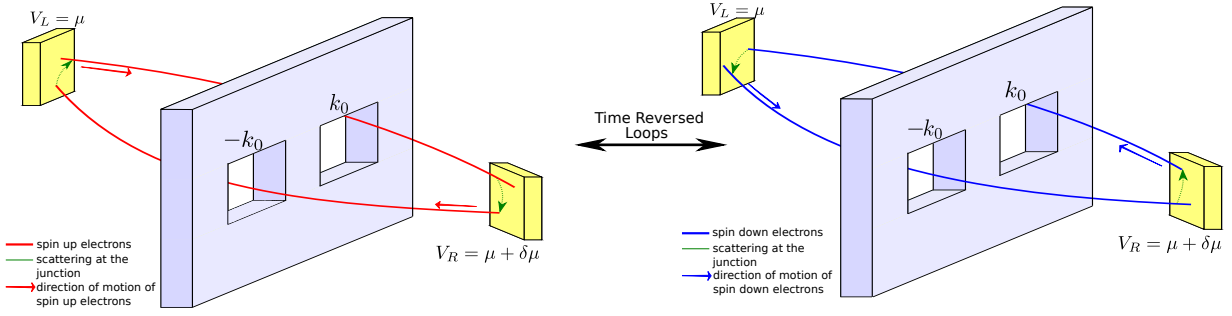


Figure 2.3: (Color online) Diagrammatic representation of the interference process. The diagram on the left shows the closed loop experienced by an electron with up spin (red line). The wall in the middle is representative of the Brillouin zone (BZ) with the holes being the only momentum values that allow low energy scattering states in the TR broken WSM bulk. The scattering processes (green arrows) at the leads take the electron from one Weyl node to the other. The diagram on the right shows the same for an electron with down spin (blue line).

nodes are disconnected at the Fermi energy and the wave-functions can be easily obtained. The scattering matrix problem in this case can be easily solved for a WSM-Normal metal interface. The fact that intra-nodal backscattering is prohibited in chiral electronic systems is well known[1]. Additionally, we find here that there is a small but non-zero probability of internodal backscattering.

This can be repeated for incident electrons in either Weyl nodes and the conclusion is the same : spin conservation during the scattering processes at the leads implies that normal reflection at any interface is inter-nodal and that the probability of scattering to the same node is suppressed. This results in the reflection amplitude picking up a phase equal to $\approx 2k_0L$ for small E when this exercise is repeated for the other boundary of the NWN geometry at $x = L$.

As can be seen from the Fig. 2.3, an electron with spin up entering the WSM from the left lead with an energy close to the Fermi energy of the WSM bulk is automatically forced to occupy a forward moving quantum state close to the Weyl node at $\vec{k} = (0, 0, k_0)$ due to the spin texture of the low lying bands. As the electron travels through the bulk, its chirality is preserved. However, at the right junction, it can either leak into the right lead or can backscatter into a quantum state near the other Weyl node at $\vec{k} = (0, 0, -k_0)$ moving to the left. The electron then travels to the left junction and gets reflected back to the original Weyl node, thus performing a closed loop evolution thereby introducing an interferometric phase. It is to be noted that the closed loop actually comprises of evolution both in real space (traversal from one lead to the other with a fixed momentum) and momentum space (scattering from one Weyl node to the other) processes. In higher orders of reflection amplitude, this fundamental loop repeats itself. The final result is a geometric progression in this loop which can be summed over. It can be easily shown that the phase picked up by the electron during one such loop is $= 2k_0L + \delta\mu L/v_z$ where $\delta\mu$ is the chemical potential of the bulk WSM. This phase relation becomes equal to $2k_0L$ as the chemical potential is tuned closer to the Fermi energy of the WSM bulk. The same structure for the amplitudes is repeated by an electron with down spin but in a time reversed fashion as depicted

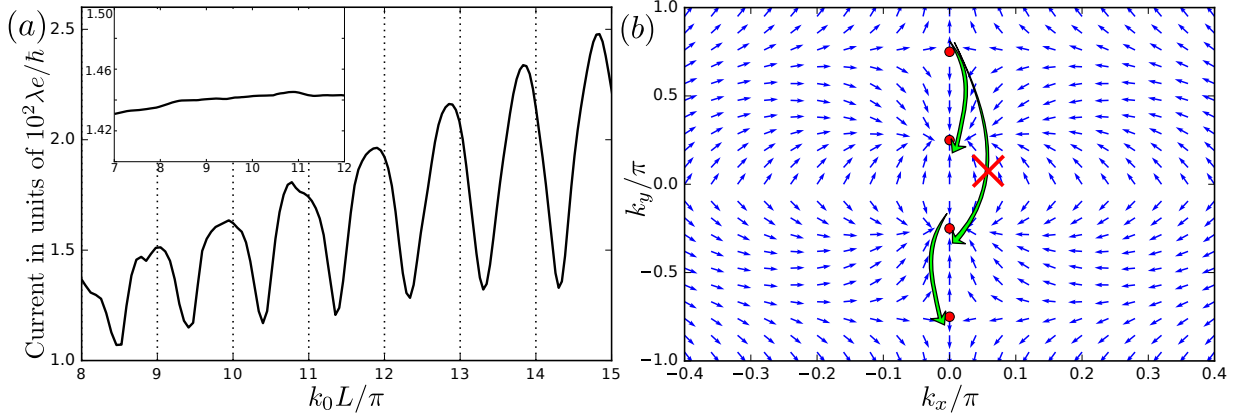


Figure 2.4: (Color online) (a) Current along the direction in which the Weyl nodes are split in the WSM bulk for the inversion symmetry broken WSM as a function of $k_0 L/\pi$. The dotted lines clearly indicate the predicted periodicity due to internodal scattering. The periodicity is a function of only one of the relevant momentum scales of the problem (see main text). The parameters used are $\lambda = 1$, $\mu_L = 0.1\lambda$, $\mu_R = 0$. The number of sites is kept fixed at $L = 60$. The inset shows the variation of current in the perpendicular direction for the same set of parameter values. As expected, it does not exhibit any periodicity. (b) Spin textures of the second band with the Weyl nodes indicated by red dots for the inversion symmetry broken WSM. Possible scattering process for a forward moving spin up electron is shown. The red cross indicates the absence of the corresponding process due to preservation of the orbital degree of freedom. The spin texture is symmetric under $\{k_x, \sigma_x\} \rightarrow \{k_z, \sigma_z\}$.

in Fig. 2.3.

It is to be noted here that the interference happens between the dominant unscattered classical path from the left lead to the right and the subleading loops. This can be thought of as a Fabry-Pérot interferometer with one arm being weakly coupled, where the coupling strength is equal to reflection strength. Since the final states of the spin up and spin down sectors are orthogonal to each other, we do not get any interference from these two time reversed partners.

2.2 Inversion symmetry broken WSM

In this section, we study the same geometry as before, but with the time-reversal symmetry broken WSM replaced by a time-reversal invariant, inversion symmetry broken WSM. A minimal model in this class [56, 57] is given by

$$H_{inv} = \lambda \sum_{\alpha=x,y,z} \sigma_{\alpha} \sin k_{\alpha} + \sigma_y \tau_y M_{\mathbf{k}} - \mu \quad (2.10)$$

where $M_{\mathbf{k}} = (m + 2 - \cos k_x - \cos k_z)$. This model describes a trivial insulator when $m > \lambda$. The bulk gap closes at $m = \lambda$ and two Dirac nodes appear at $\mathbf{k} = (0, \pm\pi/2, 0)$. For $m < \lambda$, each of the Dirac nodes split into two Weyl nodes along the k_y axis, so that the model has four Weyl nodes along the k_y axis at $k_y = \pm(\pi - k_0)$ and $k_y = \pm k_0$ where $k_0 = \sin^{-1}(m/\lambda)$.

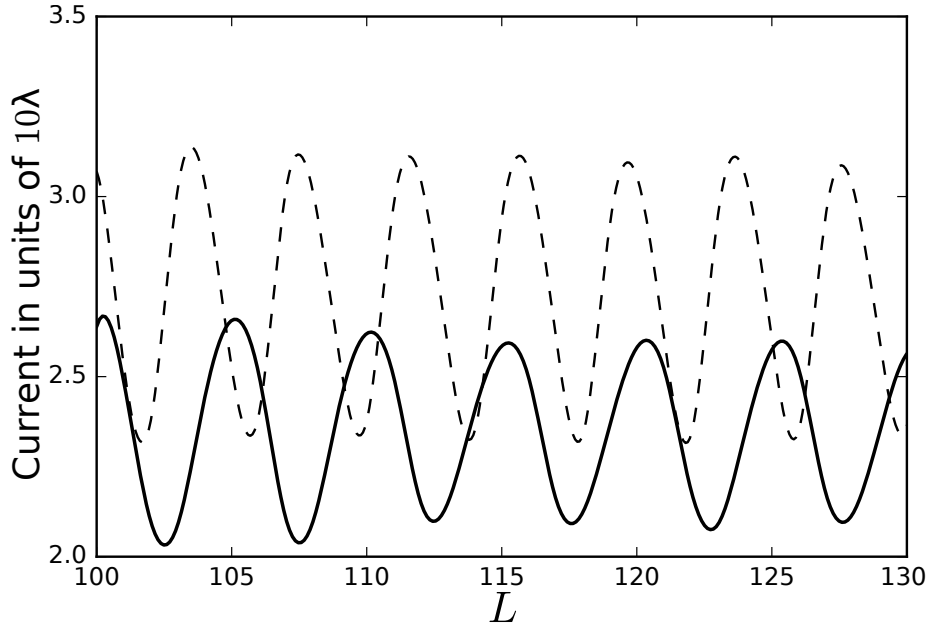


Figure 2.5: (Color online) Variation of current as a function of the number of lattice sites. The dashed line has a periodicity of 4 sites whereas the continuous line has a periodicity of 5 sites. The parameters used are $\lambda = 1$, $\mu_L = 0.1\lambda$, $\mu_R = 0$.

We now compute the current when the leads are placed at $y = -L/2$ and $y = L/2$ - i.e., along the direction of the Weyl nodes in momentum space, and also when the leads are along the x axis, perpendicular to the Weyl nodes. The lead biases are kept fixed at $\mu_L = 0.1\lambda$ and $\mu_R = 0$. The results for the y and x axes are shown in Figs 2.4(a) and its inset. Surprisingly, we find that our results are similar to those found in the time-reversal breaking 2 Weyl node WSM, although here there are four Weyl nodes, and naively, the reflection at each of the junctions with the normal leads can lead to reflection from 2 other possible Weyl nodes, if only spin conservation is taken into account, as can be seen from the spin structures plotted in Fig.2.4(b). However, when we taken into account the conservation of pseudo spin (also called orbital spin), this is no longer true.

Just focusing on the k_y axis, the Hamiltonian in eq.(2.10) reduces to

$$h(k_y) = (\lambda \sin k_y + m \tau^y) \sigma^y = \pm (\lambda \sin k_y + m \tau^y). \quad (2.11)$$

We note that the lower conduction band has lower value of energy ($\lambda \sin k_y - m$) and is thus energetically constrained to have $\langle \tau^y \rangle = -1$ ($+1$) when $k_y > 0$ ($k_y < 0$). This is in fact true for any other axis parallel to the k_y axis. The pseudospin $\langle \tau_y \rangle$ thus forms a domain wall in momentum space. This argument can be repeated in its entirety for the higher among the two valence bands and we find that $\langle \tau^y \rangle$ is constrained to be equal to -1 when $k_y > 0$ and $\langle \tau^y \rangle = +1$ when $k_y < 0$. This is exactly the same as the values for the lower conduction band. This prevents $\langle \tau^y \rangle$ from changing even for the two middle bands across the band touching points.

This implies that for the middle two bands in this four band model, only pseudospin preserving

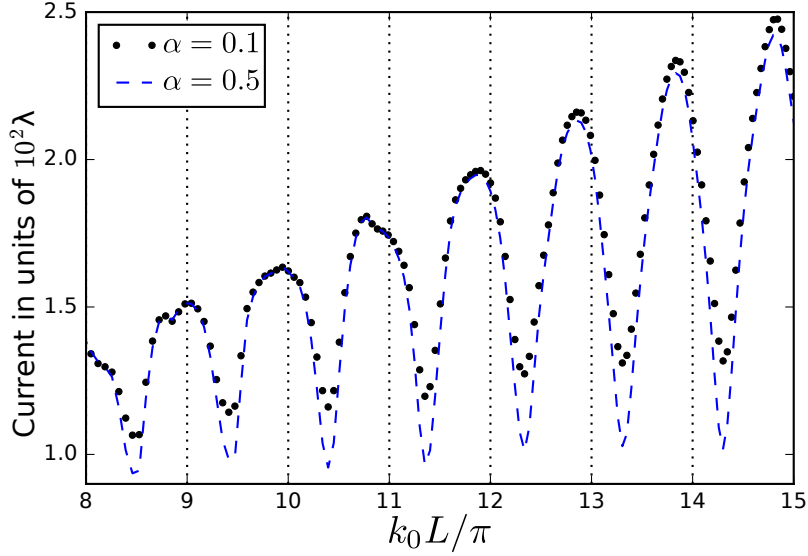


Figure 2.6: (Color online) Variation of current for different values of the scrambling parameter α . All parameters are same as that of Fig. 2.4.

scattering processes can occur between the Weyl nodes at $k_y = \pi - k_0$ and $k_y = k_0$ or between the nodes at $k_y = -\pi + k_0$ and $k_y = -k_0$. This explains why there is a single relevant scale k_0 in the scattering at the junctions even though there are multiple momentum scales in the problem (all possible differences between the nodes, or at least two possible momenta, even if we impose spin conservation).

This is further demonstrated in Fig. 2.5. Here, the value of current along the direction of separation of Weyl nodes is plotted as a function of the length of the system by fixing k_0 . Let us consider an electron with $\langle \sigma_y \rangle = 1$ moving along the k_y axis with momentum $k_y = \pi - k_0 + \delta$ where $\delta \ll k_0$. If spin is conserved, this electron can backscatter to two possible quantum states - one at $k_y = k_0 - \delta$ and the other at $k_y = -k_0 - \delta$ at a junction. The separation in the BZ of the first state with the incoming electron is equal to $\pi - 2k_0$ whereas that of the second state is equal to π .

In Fig. 2.5 the phase picked up for the chosen set of parameter values is equal to $(\pi - 2k_0)L \approx 0.5\pi L$ and πL in the other. Hence, for the first process, we expect a periodicity of ≈ 4 sites whereas, and for the second case, we expect the periodicity to be 2 as a function of the length(L). As we vary the length of the system, we find that there is a repeated pattern after the length of the system is varied by 4 sites. This is given by the dashed lines in Fig. 2.5. The entire process is repeated by changing the parameters of the Hamiltonian such that $(\pi - 2k_0)L \approx 0.4\pi L$. This, as expected, produces a periodicity of ≈ 5 sites as is seen from the continuous line in Fig 2.5. This conclusively establishes that backscattering is allowed only if pseudospin(τ) is preserved.

Thus, although in principle, the description of the multiple scattering processes in the TR-symmetric, inversion symmetry broken WSM could have been quite different from that of the TR broken WSM due to the presence of additional momentum scales, the selection rule introduced

by the preservation of the pseudo-spin degree of freedom(τ) during scattering processes reduces this setup to be exactly two copies of the previously discussed interferometer.

2.3 Summary and Conclusion

In the numerical results presented in the article, the self-energy terms considered are diagonal in the σ and τ basis. We study the possible effects of off-diagonal self-energy by introducing a minimal perturbation of the diagonal Σ given by $\Sigma = -i\tilde{t}_j^2\pi\delta_{\sigma,\sigma'} \otimes (\delta_{\tau,\tau'} + \alpha\tau_x)$. Here, α is the parameter that scrambles the pseudospin(τ) inside the leads. As can be seen from fig.(2.6), we find that the value of the current as well as the oscillations depend very weakly on α . In fact the same analysis for the TR symmetry broken model exhibit no dependence of the current on the α parameter. Hence, it has not been shown here. We thus conclude that the oscillations are quite robust and do not exactly depend on how precisely the WSM bulk is connected to the leads as well as on the nature of the leads and are a consequence of the chirality of the bulk Weyl nodes.

In the next chapter, we will be further exploring similar oscillatory patterns in WSM-superconductor heterojunctions.

Transport through Andreev bound states in a Weyl semimetal quantum dot

A quantum dot made of WSM material in the presence of superconductors is of particular interest due to the distinctive nature of transport at a WSM-Superconductor (SC) interface [54, 55, 57, 58] and provides the possibility of capturing the otherwise elusive physics associated with the chiral excitation in the WSM [58]. In this manuscript we study transport through the Andreev states of a WSM quantum dot in a simple setup where we sandwich the dot in between a superconductor and a normal lead (see Fig. 3.1). Bound levels will form in the dot due to multiple reflections from the two boundaries and these levels will strongly depend on the Fermi-energy mismatch [59] between the dot and the SC, as well as on the size of the dot. One expects some of the physics of a graphene quantum dot [60] to carry over to this case, since the WSMs also have a linear dispersion; however there are differences as well. One of the features of the Dirac dispersion is that the Andreev bound states carry current that oscillates as a function of $\chi = V_0 L / v_F$, where V_0 is the chemical potential of the dot [61, 62], L is its size and v_F is the Fermi velocity. A second oscillation appears as a function of $\delta k L$, where δk is the momentum separation of the nodes that are connected by superconducting pairing. In graphene, an s -wave superconductor couples electrons at one valley with holes at the other valley and the Andreev bound states are hence also dependent on the matching of the valley polarizations [63], with $\delta k = K - K'$ as the separation of the valleys in momentum space. On the other hand in a WSM-SC interface, the s -wave superconductor is required to couple the electrons at one node with the holes at the other node. Hence, reflection processes couple one chiral node to another node of opposite chirality [54] and $\delta k = 2k_0$ where $2k_0$ is the distance between the nodes in momentum space. Coupling between nodes is otherwise forbidden, irrespective of their positions in momentum space. Further, the inter-valley length scale $K - K'$ in graphene is quite large, whereas in WSMs, $2k_0$ is a relevant length scale, because the nodes are typically quite close to each other. At finite bias, however, as we shall see below, the relevant parameter changes from $2k_0 L$, and the nature of the bands becomes important. In the rest of this chapter, our focus is to study and predict the

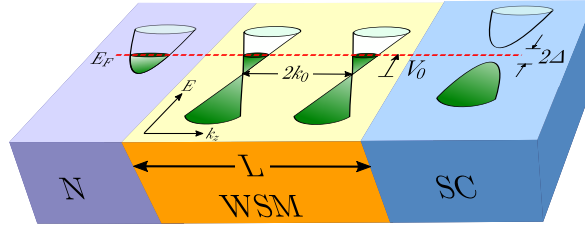


Figure 3.1: Setup of the system. A time-reversal broken Weyl semimetal WSM of length L has been sandwiched between a superconductor (SC) with a gap Δ and a normal/WSM metal lead (N). The momentum separation between the Weyl nodes in the WSM dot is $2k_0$ and the WSM has a bias V_0 .

behavior of the current through the Andreev bound states of the WSM quantum dot at a finite bias.

This chapter is arranged in the following sections. In section 3.1, we start by studying the Fig. 3.1 using the analytical scattering matrix approach. We then introduce a slightly modified Landauer-Buttiker formalism to describe the same setup numerically using Green's functions. We find that at finite bias the conduction peaks follow a periodic pattern of the form $(q_+ \pm q_-)L \approx 2n_{\pm}\pi$, with n_{\pm} being integers. Here q_{\pm} are the Fermi momenta in the quantum dot at finite bias, along the direction of conduction, and are the analogs of k_0 at zero bias. Their values can be determined from the band structure of the system and the bias V_0 present in the dot. At small enough bias, the periodicity reduces to the expected $2k_0L = n\pi$ oscillations. In section 3.1.3, we then study the same geometry with inversion symmetry broken WSM and point out certain key differences from the previous case. Lastly, we summarise our findings in 3.3.

3.1 Modelling a WSM-SC interface for a TRS broken WSM

The simplest model of a WSM with broken time-reversal (TR) symmetry requires two chiral nodes in momentum space, whereas the simplest WSM with broken inversion symmetry requires the presence of four chiral nodes. In this section we restrict ourselves to using the simplest model of a TR-broken WSM, having two nodes, for analytic simplicity. We also consider an inversion symmetry broken model, which has some new aspects beyond what is present in the two node model, later in the chapter.

As described in chapter 2, a two-band TR-broken WSM model was obtained by starting from a four-band Hamiltonian describing a 3D TI in the Bi_2Se_3 family and including a time-reversal breaking perturbation b_z [53]:

$$H_0 = \epsilon_k \tau_x - \lambda_z \sin k_z \tau_y - \lambda \tau_z (\sigma_x \sin k_y - \sigma_y \sin k_x) + b_z \sigma_z + V_0. \quad (3.1)$$

A gate potential V_0 is applied to the dot region which spans a distance L . For sufficiently small

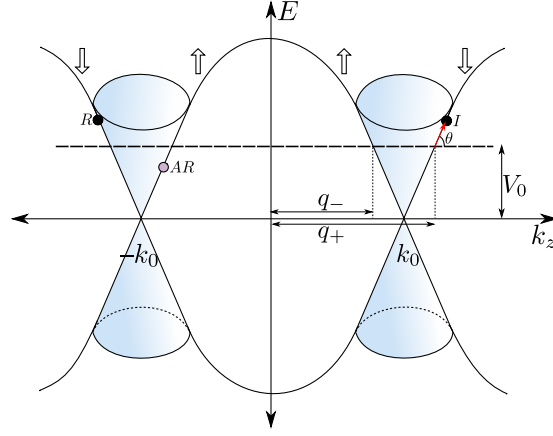


Figure 3.2: Diagrammatic representation of the possible scattering processes showing all the relevant scales. The Weyl nodes are located at $k_z = \pm k_0$ and q_{\pm} are the two possible momenta of electronic excitations above the finite potential barrier V_0 of the WSM. $\tan\theta$ denotes the Fermi velocity v_F of such excitations. I describes an incident electron and R and AR describe normal and Andreev reflected electrons and holes respectively.

V_0 , the low energy excitations can be described by the two-band Hamiltonian

$$H_{\text{WSM}} = \tilde{\epsilon}_k \sigma_z + \lambda(k_x \sigma_x + k_y \sigma_y) + V_0, \quad (3.2)$$

with $\tilde{\epsilon}_k \approx \tilde{t}(p^2 + k_z^2 - k_0^2)$ and with $p^2 = k_x^2 + k_y^2$. In the rest of the chapter, all parameters are scaled with respect to \tilde{t} which is the energy scale. The eigenvalues of Eq. (3.2) are $E_{\pm}(\mathbf{k}) = \pm \sqrt{\tilde{\epsilon}_k^2 + \lambda^2 p^2} + V_0$. This implies that the Fermi velocity is anisotropic - the velocity in the z direction is different from that in the x, y direction. Close to the Weyl nodes $k_z = \pm k_0$, the Fermi velocity along the z -direction $v_z = 2k_0$.

We construct a WSM dot by sandwiching the dot region (with a finite V_0) in between a normal-metal (N) and an s -wave superconductor (S). We then study transport through the quantum dot, first using a scattering matrix approach, where the N region is chosen to be an unbiased WSM ($V_0 = 0$) and we use Eq. (3.2) to solve for the wavefunctions. Next, we further study and verify our findings using a lattice simulation where we model the normal metal using a *flat band* approximation, i.e, by considering a uniform density of states within the relevant energy scales.

The superconducting region can be described in terms of the Bogoliubov-de Gennes (BdG) Hamiltonian:

$$H_{\text{SC}} = \begin{pmatrix} \xi_k I_{2 \times 2} & \Delta i \sigma_y \\ -\Delta i \sigma_y & -\xi_k I_{2 \times 2} \end{pmatrix}, \quad (3.3)$$

where Δ is the pairing potential in the superconductor and $\xi_k = (\hbar^2(k_x^2 + k_y^2 + k_z^2)/2m_S - \mu_S)$. m_S is the effective mass of the electron in the superconductor (we take $m_S \approx m_W$ for simplicity) and μ_S is the chemical potential. The parameter μ_S depends on the details of the superconducting material. In the numerical results we take $\mu_S \gg \Delta$, which is the realistic limit.

3.1.1 Scattering matrix approach

In this section, we describe the derivation of the scattering matrix in a Normal-WSM dot-SC system. The normal Hamiltonian is modelled by a WSM Hamiltonian without any chemical potential whereas the WSM dot is modelled by the same WSM Hamiltonian along with a barrier potential V_0 . We define $V(z) = V_0(\Theta(z) - \Theta(z - L))$ where we assign the locations of the Normal-WSM dot junction and the WSM dot-SC junctions to be at $z = 0$ and $z = L$ respectively. The wavefunction corresponding to energy E in the normal system (for $z < L$) is given by the following energy eigenstates of Eq. 3.2 in the Nambu-Gor'kov space (with the Hamiltonian in the hole space written as $-H_{\text{WSM}}^*(-\mathbf{k})$),

$$\psi_{\text{N}}(z < 0) = \sum_{\sigma=\pm} \left\{ \mathcal{E}^{\sigma} (a_{\text{R}}^{\sigma} e^{\sigma i k_e^{\sigma} z} + a_{\text{L}}^{\sigma} e^{-\sigma i k_e^{\sigma} z}) + \mathcal{H}^{\sigma} (b_{\text{R}}^{\sigma} e^{-\sigma i k_h^{\sigma} z} + b_{\text{L}}^{\sigma} e^{\sigma i k_h^{\sigma} z}) \right\}, \quad (3.4)$$

and similarly, the wavefunction in the WSM dot corresponding to the same energy is given by:

$$\psi_{\text{WSM}}(0 < z < L) = \sum_{\sigma=\pm} \left\{ \mathcal{E}^{\sigma} (c_{\text{R}}^{\sigma} e^{\sigma i k_e^{\sigma} z} + c_{\text{L}}^{\sigma} e^{-\sigma i k_e^{\sigma} z}) + \mathcal{H}^{\sigma} (d_{\text{R}}^{\sigma} e^{-\sigma i k_h^{\sigma} z} + d_{\text{L}}^{\sigma} e^{\sigma i k_h^{\sigma} z}) \right\}. \quad (3.5)$$

Here $\sigma = \pm$ is the band index, $a_i, c_i(b_i, d_i)$ denote the electron (hole) amplitudes with $i \in \{L, R\}$ denoting the left or right moving solution. $\mathcal{E}^{\sigma}(\mathcal{H}^{\sigma})$ are normalized eigenvectors, which are non-zero in electron (hole) sector of the Hamiltonian. In each sector $\mathcal{E}(\mathcal{H})^+ \propto (f_{e(h)}, (-)\lambda_{+(-)})^T$, and $\mathcal{E}(\mathcal{H})^- \propto ((-)\lambda_{- (+)}, f_{e(h)})^T$, with $f_{e(h)} = \mu_W + V(x) + (-)E_i + \sqrt{(\mu_W + V(x) + (-)E_i)^2 - (\lambda p)^2}$, $\lambda_{\pm} = \lambda(k_x + i k_y)$.

In the superconductor, the solutions of Eq. (3.3) are:

$$\psi_{\text{SC}}(z > L) = \begin{pmatrix} u c_{\uparrow} \\ u c_{\downarrow} \\ -v c_{\downarrow} \\ v c_{\uparrow} \end{pmatrix} e^{i q_e z} + \begin{pmatrix} v d_{\downarrow} \\ -v d_{\uparrow} \\ u d_{\uparrow} \\ u d_{\downarrow} \end{pmatrix} e^{-i q_h z},$$

where, with $\Omega = \sqrt{\Delta^2 - E_i^2}$,

$$u(v) = \sqrt{(E_i + (-)i\Omega)/2E_i}$$

and q_e and $-q_h$ are, respectively, the outgoing electron and hole momenta in the superconductor,

defined as (with Fermi momentum k_F)

$$q_{e(h)} = \sqrt{k_F^2 - p^2 + (-)2m_S i\Omega/\hbar^2}.$$

The boundary conditions at $z = \{0, L\}$ are given by the continuity of the wavefunction and its derivative at that point:

$$\begin{aligned} \psi_N(z) &= \psi_{\text{WSM}}(z)|_{z=0} \\ \psi_{\text{WSM}}(z) &= \psi_{\text{SC}}(z)|_{z=L} \\ \partial_z \psi_{\text{WSM}}(z)|_{z=0} &= \partial_z \psi_N(z)|_{z=0} \\ m_S \begin{pmatrix} \sigma_z & 0 \\ 0 & \sigma_z \end{pmatrix} \partial_z \psi_{\text{WSM}}(z) &= m_W \partial_z \psi_{\text{SC}}(z)|_{z=L}, \end{aligned}$$

with σ_z being the Pauli matrix. We take $m_S \approx m_W$ for simplicity. By solving these equations, we get the reflection matrices,

$$\begin{pmatrix} a_L^+ \\ a_L^- \\ b_L^+ \\ b_L^- \end{pmatrix} = \begin{pmatrix} r_{ee} & r_{eh} \\ r_{he} & r_{hh} \end{pmatrix} \begin{pmatrix} a_R^+ \\ a_R^- \\ b_R^+ \\ b_R^- \end{pmatrix}. \quad (3.6)$$

We obtain the net reflection matrix of the form

$$\mathcal{S}(E, \mathbf{p}) = \begin{pmatrix} r_{ee}(E, \mathbf{p}) & r_{he}(E, \mathbf{p}) \\ r_{eh}(E, \mathbf{p}) & r_{hh}(E, \mathbf{p}) \end{pmatrix}, \quad (3.7)$$

where, r_{ee} and r_{hh} are the reflection matrices, and r_{eh} and r_{he} are the Andreev reflection matrices, in the basis of excitations near the two nodes with \pm chirality [54]. E is the incident energy and $\mathbf{p} = (p_x, p_y, 0)$ is the momentum in the transverse direction. The differential conductance is then written as

$$G_{\mathbf{p}}(E) = \frac{e^2}{h} \text{Tr} [I_2 - R_{ee}(E, \mathbf{p})R_{ee}(E, \mathbf{p})^\dagger + R_{he}(E, \mathbf{p})R_{he}(E, \mathbf{p})^\dagger] \quad (3.8)$$

where,

$$R_{ee(he)} = \begin{pmatrix} \sqrt{v_{e(h)}^+} & 0 \\ 0 & \sqrt{v_{e(h)}^-} \end{pmatrix} r_{ee(he)} \begin{pmatrix} \frac{1}{\sqrt{v_e^+}} & 0 \\ 0 & \frac{1}{\sqrt{v_e^-}} \end{pmatrix}$$

where $v_{e(h)}^j$ is the velocity of the electron (hole) channel of the j th node. The nature of processes at the WSM-SC boundary is depicted in Fig. 3.2. The relation in Eq. 3.8 is true for each momentum \mathbf{p} in the transverse direction. Finally, we integrate over the transverse momentum

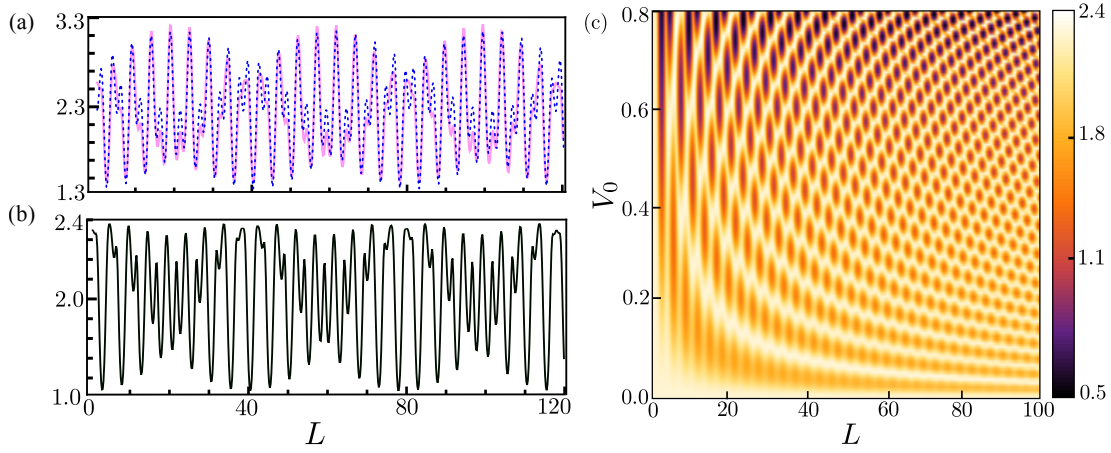


Figure 3.3: (color online) A typical pattern of the current through the WSM dot oscillating with the size of the dot, with beats due to the double periodicity (a) The peaks of conduction, i.e., the map of the Andreev spectrum, appear at lengths d where $(q_+ + q_-)d/\pi$ is an integer, with $q_{\pm} = \sqrt{k_0^2 \pm 2m_W V_0}$ in red(solid) lines. The best fit to this pattern in terms of the simple two frequency function given in Eq. 3.9 with $\alpha = 2.24$ and $\beta = 0.9$ plotted in blue (dotted) lines is also shown. Note the excellent agreement between the numerical data and the formula. The parameters used are $k_0 = 1$, $m_S = m_W = 0.5$, $\mu_S = 4$, $\mu_W = 0$, $\lambda = 0.5$, $\Delta = 0.01$, $V_0 = 0.56$. (Here we only consider normal incidence). (b) Here the current integrated over the transverse momentum is shown, which also peaks at the same lengths d where $(q_+ + q_-)d/\pi$ is an integer. (c) The complete plot of the current through the WSM dot as a function of its bias voltage and its size. Other parameters used are mentioned above.

to obtain the conductance $G(E) = \sum_{\mathbf{p}} G_{\mathbf{p}}(E)$.

We summarize our results from the scattering matrix approach in Fig. 3.3 and we emphasize the following: first, the oscillation in the conductance is present even for normal-incidence, as expected from earlier results [54, 55] which showed that the probability of normal-reflection at a WSM-SC junction is finite at normal incidence. This is further elaborated in the next section 3.2. Next, the oscillations in the conductance appear due to multiple reflection and Andreev reflections in the dot region, similar to those of a quantum mechanical double barrier problem. But for a WSM, such reflections can only take place from one chiral node to the other chiral node of opposite chirality (c.f. Fig. 3.2) as shown in the last chapter. At finite bias, due to the presence of V_0 , the relevant length scale depends on a combined function of k_0 and V_0 , i.e., they depend on $q_{\pm} = \sqrt{k_0^2 \pm 2m_W V}$, which are momenta along the direction of propagation at the Fermi energy in the dot-region. This allows us to predict the oscillation frequencies depending on the symmetry, the positions of the Weyl nodes, the bias, etc. In the present model, the conductance can be fitted well with the functional dependence of the form

$$G = \alpha + \beta \sin [(q_+ + q_-)L] \sin [(q_+ - q_-)L], \quad (3.9)$$

where, α, β are independent of the length L , and can, in principle, be obtained analytically, as shown in the Supplemental. In Fig. 3.3(a), we show the pattern of the conductance obtained

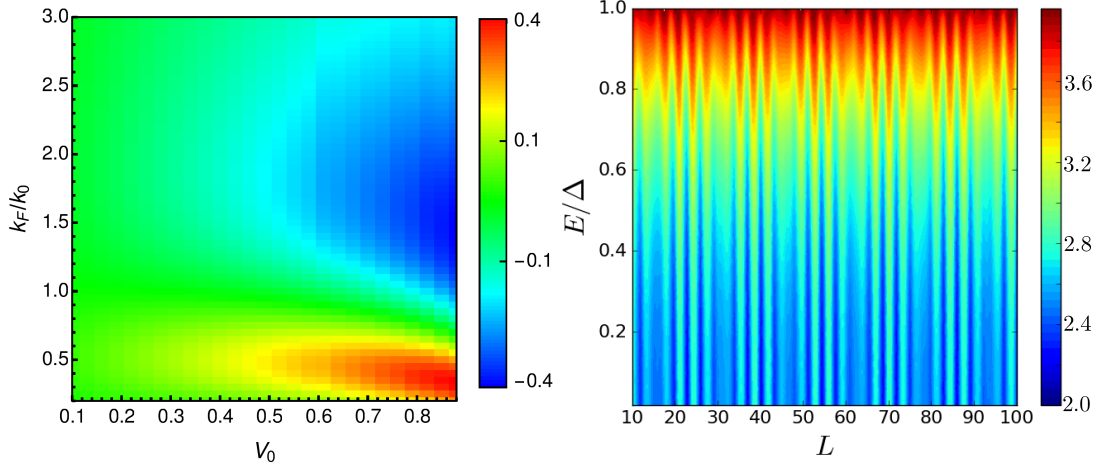


Figure 3.4: (a) Variation of the amplitude of oscillation (β) of the zero-bias conductance with the barrier height along the x axis and the ratio of the Fermi momentum and the separation of Weyl nodes along the y axis. The parameters used are $k_0 = 1$, $m_S = m_W = 0.5$, $\lambda = 0.5$, $\Delta = 0.01$. (Here we only consider normal incidence). (b) Conductance as a function of the length of the barrier along the x axis and the incident energy along the y axis at fixed $V_0 = 0.2$

at *normal incidence*, G_0 , fitted with a function of the form given in Eq. (3.9). The close correspondence shows that the theoretically obtained function can predict all the peaks in the conductance G . In Fig. 3.3(b), we show the full conductance, after integrating over the transverse momenta. The conductance continues to peak at values of L where $(q_+ + q_-)L/\pi$ is an integer. Finally, in Fig. 3.3(c) we show the variation of G_0 as functions of both the barrier height V_0 and k_0 . This pattern can be fully predicted from the functional dependence in Eq. (3.9).

Note that for $V_0 \ll k_0^2$, $q_{\pm} \approx k_0 \pm (m_W V_0/k_0)$. We also note that the amplitude of the velocity at the Fermi energy in the dot-region is $v_F = k_0/m_W$. So, the conductance oscillations have a slow frequency envelope whose period is $V_0 L/v_F = n\pi$ and a faster oscillation characterized by $k_0 L = m\pi$, (where n, m are integers), allowing us to write the conductance as

$$G \approx \alpha + \beta \sin(2k_0 L) \sin(2V_0 L/v_F), \quad (3.10)$$

with corrections to the above equation appearing only at the order $\mathcal{O}(V_0^2/k_0^2)$. Note however, that in Fig. 3.3, we have specifically chosen a value of V_0 , such that condition for Eq. (3.10) is not satisfied. In the regime, where the condition for Eq. (3.10) is satisfied, we find that the periodicity for the conductance shows peaks as a function of L and V_0 whenever $k_0 L = n\pi$ and $V_0 L/v_F = n\pi$ as expected.

Finally, we also note that the amplitude β of conductance oscillations depends strongly on the ratio k_F/k_0 and increases with increasing V_0 . On the other hand, β decreases with increasing incident energy E and the conductance reaches a maximum value of $4e^2/h$, and becomes independent of the barrier height V_0 in the limit $E \rightarrow \Delta$, matching earlier results in

similar systems like graphene [59, 61]. We show the numerical fitting of β in the phase space of $k_F - V_0$ in Fig. 3.4(a).

In passing, we also note that a similar functional dependence (as shown in Eq. (3.9)), of the conductance oscillations would be true for a graphene dot, when $2k_0$ and v_F are respectively replaced by the momentum separation between the two valleys of graphene $K - K'$ and the Fermi velocity near the Fermi energy.

3.1.2 Lattice simulation

In order to study transport in our geometry, we implement a slight modification of the standard Landauer-Buttiker formalism to suit our purpose.

We consider the x, y directions to be translationally invariant, so that the momenta k_x, k_y appear as parameters. After Fourier transforming k_z , our next step is to rewrite the Hamiltonian in the Nambu-Gorkov form -

$$H^W = \frac{1}{2} \sum_{\langle z, z' \rangle} \Psi_{z,i}^\dagger h_{Wij}(k_x, k_y) \Psi_{z',j}, \quad (3.11)$$

using the basis

$$\Psi_z^\dagger = (\psi_{z,\uparrow,1}^\dagger, \psi_{z,\downarrow,1}^\dagger, \psi_{z,\uparrow,2}^\dagger, \psi_{z,\downarrow,2}^\dagger, \psi_{z,\downarrow,1}, -\psi_{z,\uparrow,1}, \psi_{z,\downarrow,2}, -\psi_{z,\uparrow,2}).$$

For each site z , the basis $\Psi_{z,i}$ has 8 components for $i = 1, \dots, 8$. The superconductor is modeled as a 1D superconductor:

$$\begin{aligned} H^S &= \sum_z \Phi_z^\dagger (\epsilon_{SC} \eta^z + \Delta \eta^x) I_\sigma \Phi_z - t_{SC} \sum_{\langle z, z' \rangle} \Phi_z^\dagger \eta^z I_\sigma \Phi_{z'} + hc, \\ &\equiv \frac{1}{2} \sum_{\langle z, z' \rangle} \Phi_{z,i}^\dagger h_{Sij} \Phi_{z',j}. \end{aligned} \quad (3.12)$$

where $\Phi_z^\dagger = (\phi_{z,\uparrow}^\dagger, \phi_{z,\downarrow}^\dagger, \phi_{z,\downarrow}, -\phi_{z,\uparrow})$. The normal lead's Hamiltonian is written as:

$$H^L = \frac{1}{2} \sum_{\langle z, z' \rangle} a_{z,i}^\dagger h_{Lij} a_{z',j}, \quad (3.13)$$

in the basis $a_z^\dagger = (\alpha_{z,\uparrow}^\dagger, \alpha_{z,\downarrow}^\dagger, \alpha_{z,\downarrow}, -\alpha_{z,\uparrow})$.

The tunneling Hamiltonian between the WSM and the superconductor and between the WSM and the normal leads are given respectively by:

$$H^{WS} = \frac{1}{2} \Psi_{N,i}^\dagger \mathbb{V}_{ij}^S \Phi_{1,j} + \frac{1}{2} \Phi_{1,i}^\dagger \mathbb{V}_{ij}^{S\dagger} \Psi_{N,j},$$

$$\text{and } H^{WL} = \frac{1}{2} \Psi_{1,i}^\dagger \nabla_{ij}^L a_{N,j} + \frac{1}{2} a_{N,i}^\dagger \nabla_{ij}^{L\dagger} \Psi_{1,j}. \quad (3.14)$$

Here, ϕ^\dagger and a^\dagger are, respectively, the creation operators at the superconductor and the normal lead, without any orbital index. Also note that we couple both orbitals equally to the superconducting site, which, albeit not the most generic case, represents the simplest coupling.

With this choice of basis,

$$\nabla^{i=SC/L} = \begin{pmatrix} t^i & 0 & t^i & 0 & 0 & 0 & 0 & 0 \\ 0 & t^i & 0 & t^i & 0 & 0 & 0 & 0 \\ 0 & 0 & 0 & 0 & -t^i & 0 & -t^i & 0 \\ 0 & 0 & 0 & 0 & 0 & -t^i & 0 & -t^i \end{pmatrix}^T,$$

where $t^i = t^{SC/L}$ are the hopping matrix elements between the leads and the WSM. The Hamiltonian has an explicit particle-hole symmetry under

$$\Phi_{z,i}^\dagger = \mathbb{C}_{ij} \Phi_{z,j}, \quad a_{z,i}^\dagger = \mathbb{C}_{ij} a_{z,j}, \quad \Psi_{z,i}^\dagger = \mathbb{C}_{ij}^W \Psi_{z,j} \quad (3.15)$$

where, $\mathbb{C} = \sigma^y \otimes \sigma^y$, and, $\mathbb{C}^W = \sigma^y \otimes \mathbb{I} \otimes \sigma^y$.

Now, we wish to compute how the field operators evolve in time. Starting from the Heisenberg equation of motion

$$\dot{a}_{z,i} = \frac{i}{\hbar} [H^L + H^{WL}, a_{z,i}], \quad (3.16)$$

we obtain

$$\begin{aligned} \dot{a}_z &= \frac{i}{\hbar} (-h_L a_z - \nabla^{L\dagger} \Psi_1 \delta_{z,N}) \\ \Rightarrow \left(i\hbar \frac{\partial}{\partial t} - h_L \right) a_z &= \nabla^{L\dagger} \Psi_1 \delta_{z,N}. \end{aligned} \quad (3.17)$$

Here, we have used the identity $\mathbb{C}h\mathbb{C}^\dagger = -h^*$.

The solution for the operator is given by

$$\begin{aligned} a(t) &= i\hbar \mathcal{G}_L(t - t_0) a(t_0) + \int_{t_0}^t dt' \mathcal{G}_L(t - t') \nabla^{L\dagger} \Psi(t') \\ &= \eta_L(t) + \int_{t_0}^t dt' \mathcal{G}_L(t - t') \nabla^{L\dagger} \Psi(t'), \end{aligned} \quad (3.18)$$

where the Green's function \mathcal{G}_L of the uncoupled lead is the solution of the equation

$$\left(i\hbar \frac{\partial}{\partial t} - h_L \right) \mathcal{G}_L(t - t') = \mathbb{I} \delta(t - t'). \quad (3.19)$$

Similarly, for the superconducting lead, one obtains

$$\begin{aligned}\Phi(t) &= i\hbar\mathcal{G}_S(t-t_0)\Phi(t_0) + \int_{t_0}^t dt' \mathcal{G}_S(t-t')\nabla^{S\dagger}\Psi(t') \\ &= \eta_S(t) + \int_{t_0}^t dt' \mathcal{G}_S(t-t')\nabla^{S\dagger}\Psi(t')\end{aligned}\quad (3.20)$$

Finally, for the operators in the Weyl semi-metal, we write:

$$\dot{\Psi} = \frac{i}{\hbar}(-h_W\Psi - \nabla^L a - \nabla^S\Phi).\quad (3.21)$$

In the above equation, we need to substitute the solutions of $a(t)$ and $\Phi(t)$. We define the self energy operators as

$$\begin{aligned}\Sigma_L(t) &= \int_{t_0}^t dt' \nabla^L \mathcal{G}_L(t-t')\nabla^{L\dagger} \\ \text{and } \Sigma_S(t) &= \int_{t_0}^t dt' \nabla^S \mathcal{G}_S(t-t')\nabla^{S\dagger}.\end{aligned}\quad (3.22)$$

Fourier transforming the equation for $\Psi(t)$, we obtain

$$\Psi(\omega) = \mathcal{G}_W(\omega)\Gamma(\omega)$$

where $\mathcal{G}_W = (\omega - h_W/\hbar - \Sigma_L(\omega)/\hbar - \Sigma_S(\omega)/\hbar)^{-1}$ is the Green's function of the whole system and $\Gamma(\omega) = \frac{1}{\hbar}(\nabla^S\eta_S(\omega) + \nabla^L\eta_L(\omega))$.

When the system is finite along the z direction and periodic along x, y :

$$\begin{aligned}\dot{N}_{z \rightarrow z+1} &= \frac{i}{\hbar}[H, N_z] \\ &= \frac{i}{\hbar}(-\tilde{t} + \lambda_z\tau)(\Psi_{z+1, \bar{\tau}, \sigma}^\dagger(t)\Psi_{z, \tau, \sigma}(t) - \Psi_{z, \tau, \sigma}^\dagger(t)\Psi_{z+1, \bar{\tau}, \sigma}(t)).\end{aligned}\quad (3.23)$$

Here we have used the explicit form of the Hamiltonian in the main text of the chapter. So, the current along z from a given site z to $z+1$:

$$J_z(t) = \frac{ie}{\hbar}(-\tilde{t} + \lambda_z\tau)\left(\langle\Psi_{z+1, \bar{\tau}, \sigma}^\dagger(t)\Psi_{z, \tau, \sigma}(t)\rangle - \langle\Psi_{z, \tau, \sigma}^\dagger(t)\Psi_{z+1, \bar{\tau}, \sigma}(t)\rangle\right).\quad (3.24)$$

Now, Fourier transforming the field operators, we have,

$$\langle\Psi_{z, i}^\dagger(t)\Psi_{z+1, j}(t)\rangle = \int_{\omega, \omega'} \langle\Psi_{z, i}^\dagger(\omega)\Psi_{z+1, j}(\omega')\rangle e^{i(\omega-\omega')t},\quad (3.25)$$

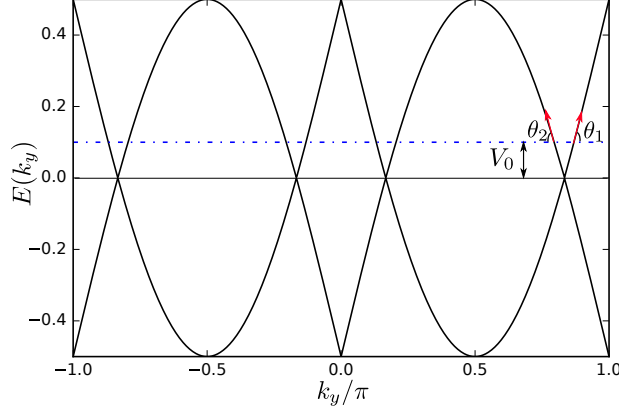


Figure 3.5: Dispersion of the inversion symmetry broken WSM along with the barrier potential V_0 . $v_{F1} = \tan(\theta_1)$ and $v_{F2} = \tan(\theta_2)$ are the Fermi velocities at q^+ and q^- respectively.

with

$$\begin{aligned} \langle \Psi_{z,i}^\dagger(\omega) \Psi_{z+1,j}(\omega') \rangle &= \sum_{PP'} \mathbb{V}_{I';kl}^{P'\dagger} \mathcal{G}_{\mathcal{W}_{I'z,li}^\dagger}(\omega') \mathcal{G}_{\mathcal{W}_{z+1,I;jm}}(\omega) \mathbb{V}_{I,mn}^P \langle \Gamma_k^{P'\dagger}(\omega') \Gamma_n^P(\omega) \rangle \\ &= \sum_{P,P'} \mathcal{G}_{\mathcal{W}_{z+1,I;jm}}(\omega) \zeta_{ml}^P(\omega) \mathcal{G}_{\mathcal{W}_{Iz;li}^\dagger}(\omega) \delta(\omega - \omega') \delta_{PP'}. \end{aligned}$$

Here $\zeta_{ml}^P(\omega) = (\mathbb{V}_I^P \rho^P(\omega) \mathbb{V}_I^{P\dagger})_{ml} f^P(\omega)$ where $\{I, P\}$ is either $\{1, L\}$ or $\{N, SC\}$ denoting either the normal or the superconducting lead respectively and $f^P(\omega)$ denotes the Fermi function of the P -th lead. Lastly, $\rho^P(\omega)$ denotes the density of states of the P -th lead.

Putting everything back in, we can finally evaluate the current

$$J_z(t) = e \text{Im} \int d\omega \sum_P \text{Tr} \left[\mathcal{A} \mathcal{G}_{\mathcal{W}_{z,I}}(\omega) \zeta^P(\omega) \mathcal{G}_{\mathcal{W}_{z+1,I}^\dagger}(\omega) \right], \quad (3.26)$$

where $\mathcal{A}_{31} = \mathcal{A}_{42} = -\tilde{t} + \lambda_z$ and $\mathcal{A}_{13} = \mathcal{A}_{24} = -\tilde{t} - \lambda_z$ and $\mathcal{A}_{ij} = 0$ otherwise. For the superconducting part, we obtained the Greens function by recursively solving for the surface of an s -wave superconductor [64]. Also, we imposed the *flatband* approximation for the normal lead. Hence, $\Sigma_L(\omega) = \mathbb{V}^L \mathcal{G}_L(\omega) \mathbb{V}^{L\dagger} = -i\pi \mathbb{V}^L \mathbb{V}^{L\dagger}$. For this calculation, we have used $t^{SC} = t^L = 0.25$. The values of the other parameters are given in the main text.

A schematic diagram that represents this process is presented in Fig.3.6(a). The information about the chemical potential of the leads (and the temperature, in principle) is included when averaging over the lead states.

We obtain the current as a function of k_0 and V_0 with the chemical potential on the left lead kept fixed at $\Delta/2$, and summarize the results in Figs. 3.6(b) and (c), where we have also taken the transverse momentum to be zero. As in the scattering matrix calculation, here again, the current oscillates as a function of both $k_0 L/\pi$ and $V_0 L/\pi v_F$, which clearly confirms the

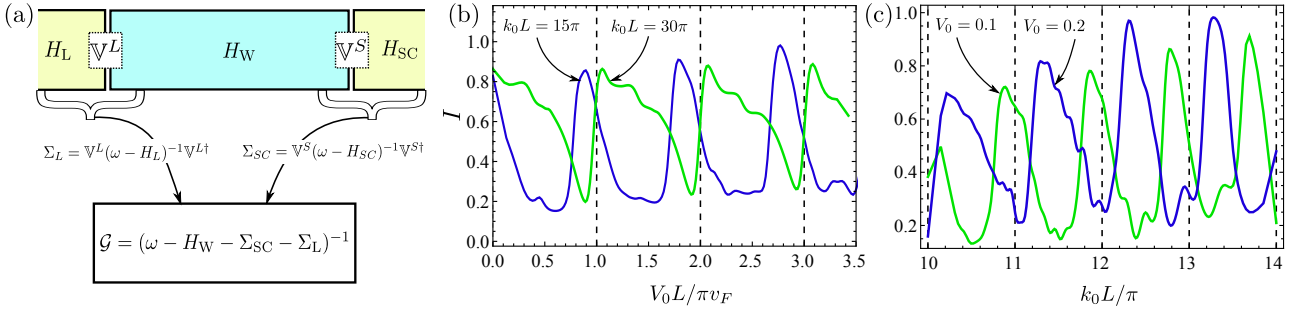


Figure 3.6: (color online) (a) The schematic of the procedure used for the lattice simulation. After integrating out the two leads, one superconducting and one normal metal, the full Green's function of the system, \mathcal{G} , contains the corresponding self energies. The final current through the system is obtained after averaging over the lead states, which include the information of the Fermi function of the leads (b), (c) Results of the lattice based simulation, verifying the oscillation dependence of the current as a function of V_0 and k_0 respectively. Here, the dotted lines show the periodicity expected from Eq. 3.10. The parameters used are $\Delta = 0.1$, $\epsilon = 6$, $\lambda_Z = \lambda = 0.5$, $\mu_L = 0.05$, $\mu_R = 0$. The length of the WSM dot is kept fixed at 60 in units of lattice spacing.

central result of our chapter that inter-node Andreev reflection, if not prohibited by additional symmetries of the problem [55], plays a crucial role in determining transport properties of the Weyl semimetal-superconducting interface. In order to find the Fermi velocity, we first determine q^+ and q^- , the points of intersection of the barrier potential with that of the energy dispersion, as shown in Fig.3.5. The Fermi velocities at these points are given by v_{F1} and v_{F2} respectively and are obtained by taking the derivative of the dispersion with the momentum. The Fermi velocity used to obtain Fig.3.7(a) is given by the mean of these two velocities $v_F = (v_{F1} + v_{F2})/2$. As we vary V_0 , v_F also changes due to nonlinearity of the dispersion beyond a small value of the potential V_0 . We scale the V_0 axis of Fig.3.6 and Fig.3.7 by a factor of $1/v_F$.

3.1.3 Inversion symmetry broken WSM

The distinct unambiguous signatures of WSM systems can be further clarified if one takes an inversion symmetry broken WSM. An inversion broken WSM requires the presence of at-least four chiral nodes in the Brillouin zone.

The Hamiltonian used to describe an inversion symmetry broken WSM is the same as chapter 2 written in the Nambu basis:

$$H_{\text{inv}} = \lambda \sum_{\alpha=x,y,z} \sigma_{\alpha} \eta_z \sin k_{\alpha} + \sigma_y \tau_y \eta_z M(\mathbf{k}), \quad (3.27)$$

where, just like the last chapter, $M(\mathbf{k}) = m + 2 - \cos k_x - \cos k_z$. We remind ourselves that this model describes a normal insulator when $m > \lambda$ and a Dirac semi-metal when $m = \lambda$ with two nodes at $k_y = \pm\pi/2$. When $m < \lambda$, each of the two nodes split into two Weyl nodes forming a Weyl semi-metal with 4 nodes. Note that for this model, $k^+ + k^- = \pi$ is fixed.

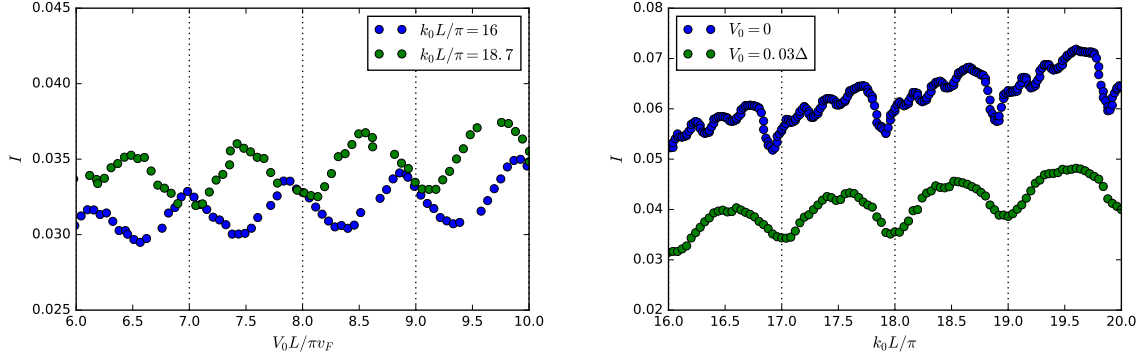


Figure 3.7: (a) Variation of the current as a function of the barrier height for an inversion symmetry broken WSM. The length of the Weyl semimetal is kept fixed at 100 sites. The values of the other parameters are $\lambda = 1$, $\mu_L = 0.5\Delta$ and $\mu_R = 0$. Here, $k_0 = \pi/2 - \sin^{-1}(m/\lambda)$ is kept fixed. (b) The same as a function of the separation of Weyl nodes (m is varied to change the separation of the Weyl nodes) in the Brillouin zone for fixed barrier height. The dotted lines indicate the periodicity expected from the ideas of the main text.

In this simplest situation, the nodes can be co-linear in momentum space, and without loss of generality, can be placed at momentum $\mathbf{k}_1 = (-k^+, 0, 0)$, $\mathbf{k}_2 = (-k^-, 0, 0)$, $\mathbf{k}_3 = (k^-, 0, 0)$, $\mathbf{k}_4 = (k^+, 0, 0)$ with $k^+ = \sin^{-1}(m/\lambda)$ and $k^- = (\pi - \sin^{-1}(m/\lambda))$. Time reversal symmetry requires the first and last nodes to have the same chirality, and the two nodes in the middle to have opposite chirality. If the chirality of the nodes were not relevant -i.e., if we were working with a 3 dimensional Dirac metal, then proximity to an s-wave superconductor would couple nodes of opposite momenta through Andreev processes. So we would expect the relevant momentum scales to be $2k^\pm$. But in a WSM the coupling is only allowed between nodes 1-2, and 3-4, giving the relevant momentum scale $k^+ - k^-$ and between nodes 1-3, and 2-4, giving the relevant momentum scale $k^+ + k^-$. Thus the relevant scales of the conductance oscillations strongly distinguishes between a dot made of a Dirac metal from a dot made of a WSM. However, working with a 4-band model is cumbersome in the scattering matrix framework.

The relevant inter-nodal distance is $k^+ - k^- = 2k_0$. We keep the x and z directions periodic and the y direction finite. Repeating the calculations for this setup, we end up with the same expression for the current (i.e, Eq.3.26) with \mathcal{A} redefined such that $\mathcal{A}_{21} = \mathcal{A}_{43} = \lambda$ and $\mathcal{A}_{12} = \mathcal{A}_{34} = -\lambda$ and $\mathcal{A}_{ij} = 0$ otherwise. The results are summarized in Fig. 3.7, and clearly, the two basic periodicities of the current as emphasized in the previous section are also seen here.

3.2 Oscillations in the Josephson current in Weyl semimetals

In this section we study the current in a simple Josephson junction setup. We show that unlike in a normal metal-SC interface, the inter-nodal ‘normal’ (electron to electron) reflection process in

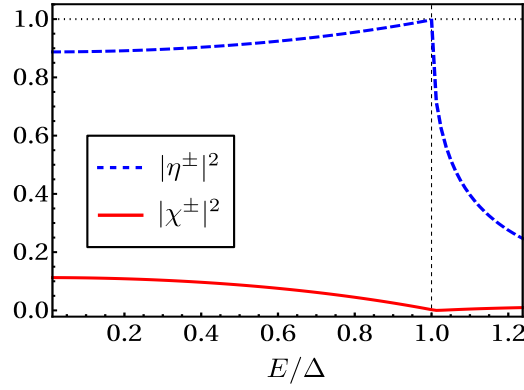


Figure 3.8: (Color online) The probability that an electron will be reflected as an electron ($|\chi^\pm|^2$) or as a hole ($|\eta^\pm|^2$) at a WSM-SC interface, discussed in Eq. (3.28). Note that the probability of reflection as an electron is finite. The parameters used are $\hbar^2 k_0^2 / 2m_W = 10\mu_W = 10^3\Delta = \mu_S/2$, $p \ll k_0$ and $m_S = m_W$.

a WSM-SC interface is not suppressed even for energies close to Fermi-energy, due to the broken time-reversal symmetry separating the Weyl nodes. The Josephson current, flowing through the bound levels formed by multiple inter-nodal ‘normal’ and Andreev (electron to hole) processes in a SC-WSM-SC system, consequently, acquires a specific periodicity as a function of the length of the WSM which depends only on the separation of the Weyl nodes in the momentum space (see Fig. 3.10).

This oscillation in the Josephson current and the resulting changes of sign of the critical current at arbitrary values of ϕ (or the 0 - π transition) is an inherent property of the SC-ferromagnet-SC junction [65–70] and has also been experimentally observed[71]. Since our model also explicitly violates time-reversal invariance, our results show quite a strong similarity with the Josephson current in similar systems[72] as well in semiconductor nanowires with Zeeman coupling[73].

Since this work has been incorporated in a previous thesis, we briefly quote the key results before moving on.

3.2.1 WSM-SC junction

For the case of a WSM-SC junction, the WSM and the superconducting wavefunctions on the two sides of the junction can be matched at the junction by requiring the continuity of the wavefunction and its first derivative. As is shown earlier in this chapter, this leads to the net reflection matrix \mathcal{R}^j from the WSM-SC junction, which connects the left and right-moving solutions at the interface with the j th superconductor.

For the case of near-normal incidence ($k_0 \gg p$) of an electron, the reflection matrices reduce to the form:

$$r_{ee}^j = \begin{pmatrix} \chi^+ & 0 \\ 0 & \chi^- \end{pmatrix}, \quad r_{he}^j = e^{-i\phi_j} \begin{pmatrix} 0 & \eta^+ \\ \eta^- & 0 \end{pmatrix}. \quad (3.28)$$

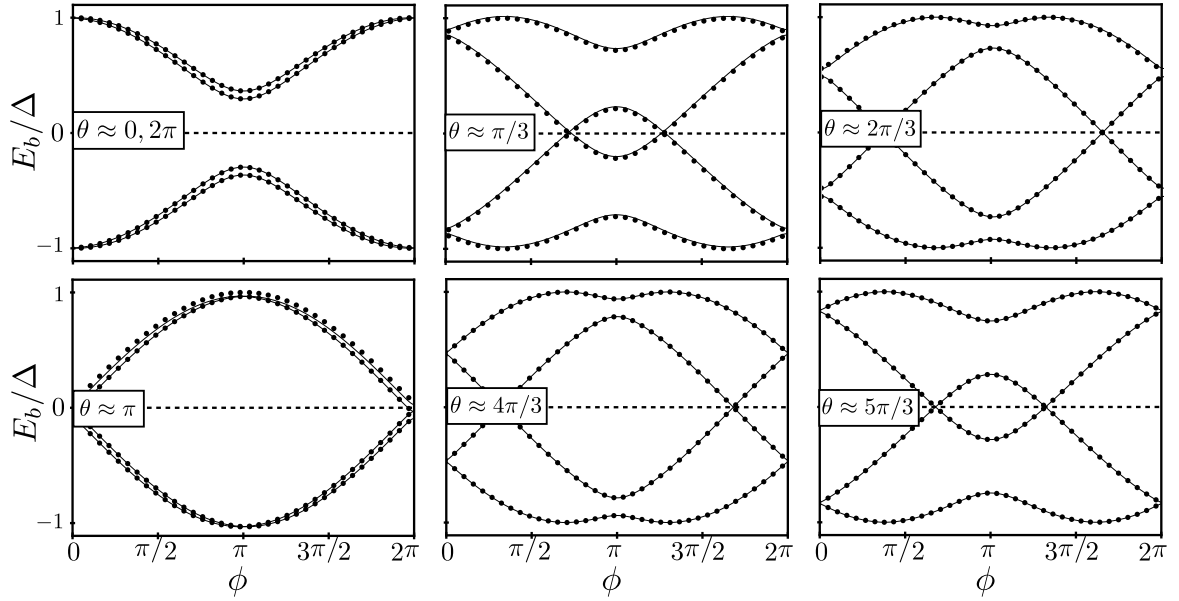


Figure 3.9: The variation of the bound levels (solutions of Eq. (3.29)) near the chemical potential with the length L of the WSM for various values of θ , where $\theta = 2k_0L \bmod(2\pi)$. The parameters used are the same as in Fig. 3.8.

In this simplified form it is immediately clear that both the reflection and the Andreev reflection change the chirality and can only take place from one node to the other because of the chiral nature of the nodes. We plot the probabilities of normal and the Andreev reflection in Fig. 3.8. We note that even at energies close to the Fermi energy, normal reflection is not suppressed as the existence of the new momentum scale $k_0 \neq k_F$, allows the incident electron momentum to be different from the Fermi momentum of the superconductor [74].

3.2.2 Bound levels in the SC-WSM-SC geometry

Multiple reflections at the *WSM-SC* boundaries lead to bound electronic levels in the *SC-WSM-SC* geometry. The bound levels E_b can be found by solving

$$\det [I_{4 \times 4} - \mathcal{R}^L \mathcal{M} \mathcal{R}^R \mathcal{M}] |_{E=E_b} = 0, \quad (3.29)$$

where \mathcal{M} is the matrix which accounts for the phase the electron/hole acquires while moving from one junction to another. Writing

$$\mathcal{R}^L \mathcal{M} \mathcal{R}^R \mathcal{M} = \begin{pmatrix} \mathcal{T}_{ee} & \mathcal{T}_{eh} \\ \mathcal{T}_{he} & \mathcal{T}_{hh} \end{pmatrix}, \quad (3.30)$$

in the limit of near normal incidence with $k_0^2/2m_W$ much larger than incident energy E and μ_S much larger than pairing potential Δ , the \mathcal{T} matrices have the simplified form (with $m_S = m_W$):

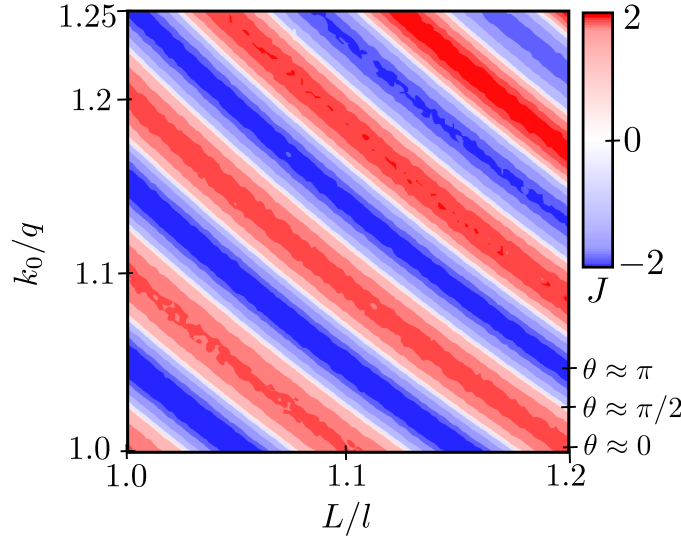


Figure 3.10: (Color online) The Josephson current as a function of both L and k_0 is shown at the value of $\phi \approx \pi/2$. The initial value at the origin is $(k_0, L) = (q, l)$, $ql \approx 10\pi$. The contours of constant current follow a set of (approximate) hyperbolas for constant $\theta = 2k_0L \bmod(2\pi)$, a few of which are shown in the right margin (with the minimum and the maximum current occurring near $\theta = \pi$ and $\theta = 0$ respectively). Other parameters used are the same as in Fig. 3.8.

$$\mathcal{T}_{ee} = \begin{pmatrix} \alpha^+ & 0 \\ 0 & \alpha^- \end{pmatrix}, \quad \mathcal{T}_{he} = \begin{pmatrix} 0 & \beta^+ \\ \beta^- & 0 \end{pmatrix}, \quad (3.31)$$

$$\text{with} \quad \alpha^\pm \approx e^{\pm 2ik_0L} (1 + 4iE\delta),$$

$$\beta^\pm \approx \pm e^{\mp 2ik_0L} 2i(1 + e^{-i\phi})\Delta,$$

where $\delta = \sqrt{2m_W\mu_S}/k_0\Omega$ and $\phi = \phi_R - \phi_L$.

This immediately shows the periodicities: $\mathcal{T}(2k_0L) = \mathcal{T}(2k_0L \rightarrow 2k_0L + 2\pi)$, which implies that the bound levels E_b , the solutions of Eq. 3.29 are periodic in both ϕ and $2k_0L$. The periodicities of E_b in the difference of the superconducting phases ϕ and in $2k_0L$, in the limit of $k_0 \gg p$ is shown in Fig. 3.9. This is our central result.

3.2.3 Periodic oscillations in the Josephson current

The Josephson current for the system with the total Hamiltonian H is written as $J_{\text{jos}} = \frac{2e}{\hbar} \left\langle \frac{\partial H}{\partial \phi} \right\rangle$, where the average is taken over the filled states of the system. For the non-interacting system, where the length L is much smaller than the coherence length in superconductors, the Josephson current flows through the bound levels (neglecting the continuum contribution) and can be estimated as [75]

$$J(\mu_W) = \frac{2e}{\hbar} \sum_b \frac{\partial E_b}{\partial \phi} f(E_b - \mu_W), \quad (3.32)$$

where f is the Fermi-distribution function. Apart from the 2π periodicity of the Josephson current in ϕ , as the bound levels E_b are periodic in L with the periodicity of π/k_0 , the Josephson current also inherits the same periodicity.

The Josephson current as a function of both k_0 and L is also shown in Fig. 3.10, where the locus of constant current approximately follows $\theta = 2k_0L \bmod(2\pi)$. This is another of our main results.

3.3 Summary

To summarise, we have discussed transport through a Weyl semimetal quantum dot, in a normal-metal-WSM-superconductor geometry, that captures a number of features unique to the presence of chiral nodes in the WSM. We took a simple time-reversal broken WSM and studied it in the scattering matrix approach as well as by using tight-binding simulations. The key result of our work, Eq. (3.9), differentiates the effect of Klein tunneling in the Dirac system from that due to the presence of chiral nodes in the WSM. An experimental setup should be similar in essence to that shown in Ref. [60], but the details of the prediction would depend on the material used.

Lastly, we have demonstrated the presence of an unusual periodicity in the Josephson current that results in the striking $0 - \pi$ transition that the critical Josephson current goes through as a function of only the separation of the two Weyl nodes and the size of the sample. This provides a direct path for possible observations of the manifestation of inter-nodal reflection in Weyl semimetals.

Spin-dependent Andreev reflection in spin-orbit coupled systems by breaking time-reversal symmetry

In this chapter we take a model system that represents a number of 2D systems (like silicene, germanene, stanene), typically in a honeycomb lattice, with a small time-reversal (TR) invariant spin-orbit coupling and optionally a sub-lattice staggered potential [76–80]. Andreev reflection, among other transport phenomena, has been studied extensively in these systems [81, 82, 82, 82–89]. As the spin-symmetry is typically not broken, AR is not suppressed as long as the band gap remains smaller than the superconducting gap. Following the discussion by Haldane [33], time-reversal symmetry (TRS) can be broken in such 2D systems by introducing complex next-nearest-neighbor (NNN) hopping (in addition to existing real-spin orbit coupling, which does not break TRS), which acts like a pseudo spin-orbit coupling in the orbital space. This, physically, may result from the orbital effect of a magnetic field in the system. In cold-atomic setup, such a system is, interestingly, realized through periodic drive. Such *Floquet manipulation* of band-structures, by driving a quantum system periodically, has been of much interest in recent times [56, 57, 90–106] in a number of contexts including topological insulator [90, 100–102], fractional chern insulators [97], Majorana modes [106], phosphorene [98], spintronics [99], engineered gauge fields [96], disordered systems [104], nano-wire as well as Weyl semimetals [56, 57]. Under certain conditions the dynamics of a periodically driven system can be described in terms of an effective static Hamiltonian [107–110]. The central idea is to have the driving off-resonant and to project the time-periodic Hamiltonian into the zero-photon sector. The effective Hamiltonian is often topologically non-trivial and opens the door towards controlling the band-structure by means of external fields. Such ideas have been tested experimentally in solid-state [111], photonic [112] and also cold-atomic [113–115] systems, where it has been particularly successful and generated much excitement in theorists and experimentalists alike.

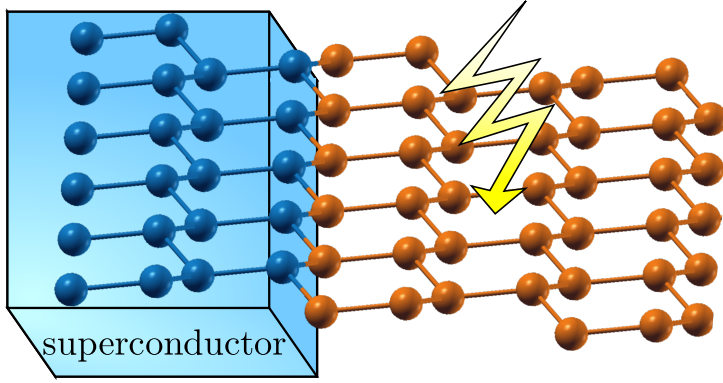


Figure 4.1: A setup where the model we discuss can be realized. On the right side ($x > 0$), the \mathcal{N} region is modeled with spin-orbit coupled two dimensional material (say silicene). Time reversal symmetry is broken with either a complex next-nearest-neighbor hopping term or with circularly polarized light. The left side ($x < 0$), the \mathcal{S} is modeled with a proximity induced superconductor of the same material (without the radiation).

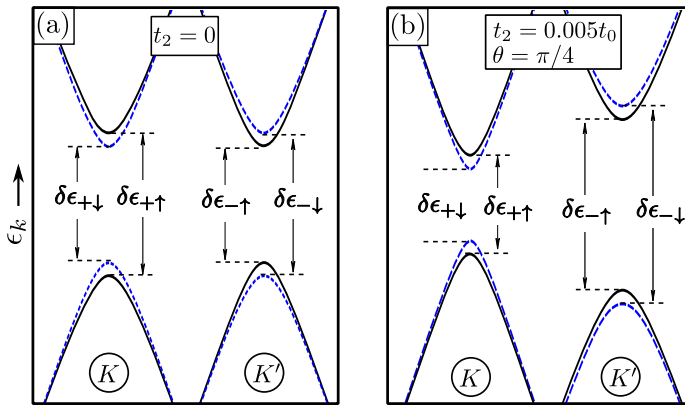


Figure 4.2: Spin asymmetry in band structure created by next-nearest-neighbor hopping as shown in Eq. (4.4). The Hamiltonian of the time reversal symmetric system with $\delta\epsilon_{\eta\sigma} = \delta\epsilon_{-\eta-\sigma}$ is shown in (a) Such symmetry is broken for finite t_2 and θ , as shown (b). The parameters used are $lE_z = 0.005t_0$ and $\lambda = 0.05t_0$.

The setup we consider is shown in Fig. 4.1, where a part of the system has proximity induced superconductivity (the \mathcal{S} region) and the other part (the \mathcal{N} region) has broken TRS due to complex NNN hopping, representing a system with spin-orbit as well as pseudo spin-orbit coupling. The effective Hamiltonian of the system \mathcal{N} , in presence of TRS breaking, would include an additional mass term [33]. In this chapter we explore how the competition between the spin-orbit coupling and the TR breaking mass term can give rise to spin dependent AR reflection probability in certain parameter regimes.

In the case of generating the NNN coupling by periodically driving the system, the \mathcal{N} region in Fig. 4.1, is irradiated with circularly polarized light with frequency much larger than any other energy scale of the system (such as the natural band-width). Apart from the driving amplitude and the frequency of the drive, it is also possible to control this probability by collimation of the incident angle of the electrons. Further, as the spin-orbit coupling in the relevant system is

typically of the order of only a few millielectron-volt [116], the required driving amplitude for the spin polarised conductance to show up is also relatively small.

4.1 Pseudo Spin-Orbit Coupled system

A two dimensional honeycomb lattice with spin-orbit coupling is represented by the low-energy Hamiltonian

$$\mathcal{H}_\sigma^0 = \begin{pmatrix} H_{+, \sigma}^0 & 0 \\ 0 & H_{-, \sigma}^0 \end{pmatrix} \quad (4.1)$$

where

$$H_{\eta, \sigma}^0 = \frac{3t_0 a_0}{2} (\eta k_x \tau_x + k_y \tau_y) + (lE_z + \eta \sigma \lambda) \tau_z - \mu \mathbb{I}. \quad (4.2)$$

The nearest neighbour hopping, t_0 , is independent of the spins. a_0 is the lattice spacing, $\sigma = \pm$ refers to the up/down spin and τ_i are Pauli matrices in the sublattice basis. In a buckled structure, the atoms of the sub-lattices are separated in the direction perpendicular to the plane of the lattice. $2l$ is the separation between the a and b sublattices and E_z is the applied electric field. The energy separation lE_z acts as a staggered potential between the sub-lattices. The term λ controls the strength of the spin-orbit coupling and μ is the chemical potential. We note that λ only describes the time-reversal (TR) invariant intrinsic spin-orbit interaction and not the Bychkov-Rashba effect, since we expect the latter to be small for such systems [116, 117]. This description can apply to a variety of topical models such as graphene, silicene, germanene and stanene in honeycomb lattice. The above low-energy Hamiltonian can be derived by expanding the lattice Hamiltonian H^{hc} of such systems near the two inequivalent Dirac points (marked by $\eta = \pm$) in the Brillouin zone.

When complex NNN hopping is introduced, the Hamiltonian gets modified[33]:

$$H_{\text{Hal}, \eta, \sigma}^{\mathcal{N}} = \frac{3t_0 a_0}{2} (\eta k_x \tau_x + k_y \tau_y) + (lE_z + 3\sqrt{3}\eta \Xi_\sigma) \tau_z - \mu \mathbb{I}. \quad (4.3)$$

Here,

$$\Xi_\sigma = \frac{\sigma \lambda}{3\sqrt{3}} - t_2 \sin(\theta), \quad (4.4)$$

where t_2 is the NNN hopping amplitude and $+(-)\theta$ is phase associated with the hopping from A to A (B to B) sub-lattices. The Hamiltonian results in a similar band-structure

$$\epsilon_{\eta, \sigma}(k) = -\mu \pm \sqrt{t_0^2 (k_x^2 + k_y^2) + \mathcal{D}_{\eta\sigma}^2}, \quad (4.5)$$

with $\mathcal{D}_{\eta\sigma} = lE_z + 3\sqrt{3}\Xi_\sigma$ is the gap introduced by the TRS breaking. Fig. 4.2 describes the band structure before and after the time reversal symmetry is broken by introducing the NNN hopping term.

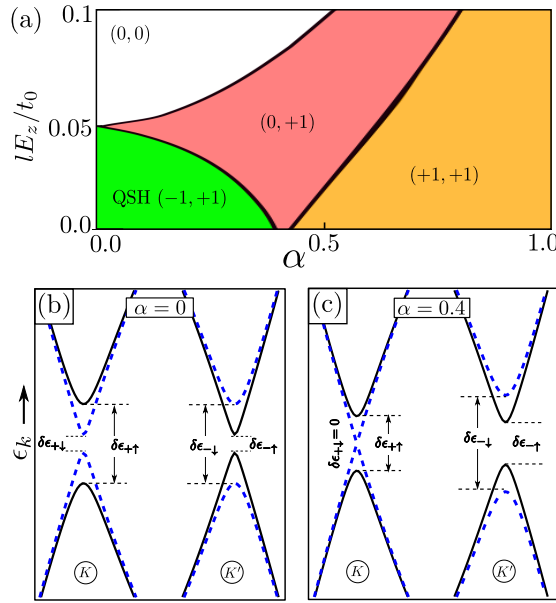


Figure 4.3: The topological phases of the system Eq. (4.8) is shown above in (a), where the Chern number of up and down spin bands are shown in parenthesis. The quantum spin-hall system is particularly marked. Periodic drive created spin asymmetry in band structure is shown in (b) and (c). The Hamiltonian of the pristine system ($\alpha = 0$), representing silicene is time reversal symmetric giving the relation $\delta\epsilon_{\sigma}^{\eta} = \delta\epsilon_{-\sigma}^{-\eta}$ among the gaps of the system. Such symmetry is broken for finite α , as shown in the right. An Andreev reflection process is allowed for an incident electron with energy E , spin σ and valley index η , only when $\epsilon \geq \max\{\delta\epsilon_{\sigma\eta}, \delta\epsilon_{-\sigma-\eta}\}$. $lE_z = 0.08$ for both (a), (b) and $\omega = 10t_0$ for (c).

In Fig. 4.1, the \mathcal{N} region, $x > 0$, is described by the Eq. (4.3). On the other hand, the region \mathcal{S} is modeled by the system along with proximity induced s -wave superconductivity. For $x < 0$ (region \mathcal{S}) we take the Hamiltonian Eq. (4.2) and set $lE_z = 0$ for simplicity. Further we need to take a large doping U_0 for the mean-field description of the superconducting part to remain valid. The pair potential Δ (which we consider to be real) couples the time-reversed electron and hole states in the superconductor. Hence, we arrive at the low-energy Hamiltonian of the \mathcal{S} side [81]:

$$H_{\eta,\sigma}^{SC} = \begin{pmatrix} H_{\eta,\sigma}^0 & \sigma\Delta\mathbb{I} \\ \sigma\Delta\mathbb{I} & -H_{\eta,\sigma}^0 \end{pmatrix}. \quad (4.6)$$

where $H_{\eta,\sigma}^0$ is the Hamiltonian of the static system in Eq. (4.2). For our numerical simulations we have used $U_0 = 2t_0$.

Either θ or t_2 can be varied to control $\mathcal{D}_{\eta\sigma}$. This gap will compete with the real spin-orbit coupling energy scale λ and in suitable situation spin-dependent Andreev reflection might be observed.

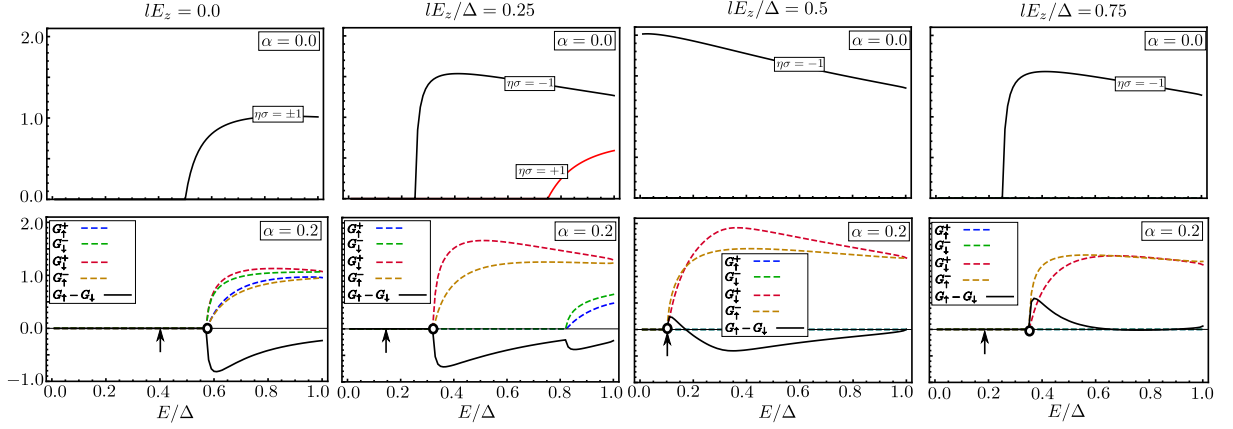


Figure 4.4: Top panel: The conductances of an electron in the static ($\alpha = 0$) system for various values of the staggered potential (lE_z). Out of the four channels ($\eta = \pm 1, \sigma = \pm 1$) the AR probabilities are the same for channels with same value of $\eta\sigma$. For certain values of lE_z , only two of the channels with $\eta\sigma = -1$ contribute in transport. Bottom panel: For similar values of lE_z , the driven system with $\alpha = 0.2$ and $\omega = 10t_0$, significant difference in AR probability arises, even when it remains sufficient to consider only two of the channels ($\eta\sigma = -1$). In these figures the arrows on the E axis denote the minimum gaps of the system and the minimum energies E that satisfies Eq. (4.15) are marked by circles. The parameters used are $\lambda = 0.5\Delta$, $\Delta = 0.1t_0$.

4.2 Time Reversal symmetry breaking by Periodic drive

As a physical realization of the model discussed in the previous section, we next turn our attention to a similar two dimensional systems with spin orbit coupling. Time reversal symmetry in this system is now broken when circularly polarized light of frequency ω is irradiated on it. This high frequency drive is represented by a time dependent vector potential $A(t) = A_0(\cos \omega t, \sin \omega t, 0)$.

The irradiation can be treated in the perturbative high-frequency approximation where ω is the largest energy scale of the system. In the presence of the radiation, the hopping elements of the honeycomb lattice Hamiltonian of Eq. (4.2), H^{hc} , are modified by Peierls substitution, making the Hamiltonian $H^{\text{hc}}(t)$ time periodic with the n th Fourier component being $H^{\text{hc}(n)}$. In the high-frequency limit, the effective Hamiltonian that controls the dynamics of the system is given by $H_{\text{eff}}^{\text{hc}} \approx H^{\text{hc}(0)} + \sum_{n \neq 0} H^{\text{hc}(-n)} H^{\text{hc}(n)} / n\omega$. Expanding this effective Hamiltonian near the Dirac points provides us with a low-energy Hamiltonian for the \mathcal{N} region:

$$\mathcal{H}_{\sigma}^{\mathcal{N}} = \begin{pmatrix} H_{+, \sigma}^{\mathcal{N}} & 0 \\ 0 & H_{-, \sigma}^{\mathcal{N}} \end{pmatrix} \quad (4.7)$$

where [110]

$$H_{\eta, \sigma}^{\mathcal{N}} = \frac{3t_{\sigma}a_0}{2}(\eta k_x \tau_x + k_y \tau_y) + (lE_z + 3\sqrt{3}\eta\Lambda_{\sigma}^0)\tau_z - \mu\mathbb{I}, \quad (4.8)$$

with

$$t_{\sigma} = t_0 J_0(\alpha) - \frac{4t\sigma\lambda}{3\omega} \sum_{n \neq 0} \frac{J_n(\alpha) J_n(\alpha\sqrt{3})}{\sqrt{3}n} \times$$

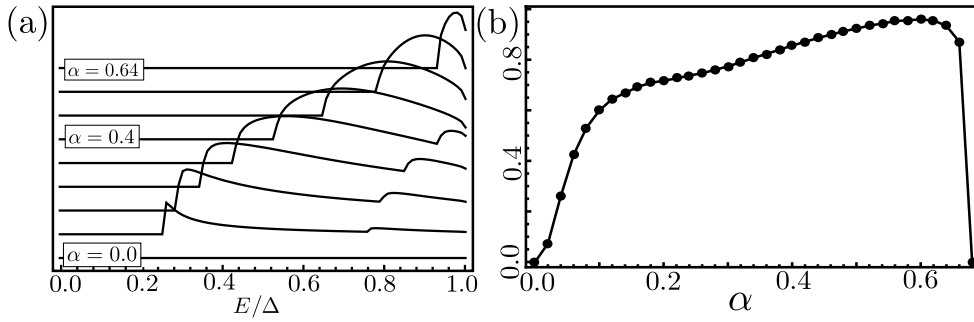


Figure 4.5: The amplitude of the difference in conductances $\sum_{\eta} (G_{\eta\downarrow} - G_{\eta\uparrow})$ plotted against E/Δ . As α increases the system develops a gap at the K and K' points and consequently with larger α , the sub-gap conductance vanishes, giving rise to zero spin-dependent value. For the choice of our parameters: $lE_z = 0.25\Delta$, $\lambda = 0.5\Delta$ and $\Delta = 0.1t_0$, the critical value of α is 0.64. The value of the driving frequency is chosen to be $\omega = 10t_0$. Surprisingly, the maximum value of the spin-dependent conductance, as a function of E/Δ (E being the incident energy) remains partly constant with α , shown in the second figure.

$$\times \left(2 \sin \frac{n\pi}{2} + \sin \frac{\pi n}{6} \left(1 + \frac{1}{2}(-1)^n \right) \right), \quad (4.9)$$

$$\Lambda_{\sigma}^0 = \frac{\sigma \lambda J_0(\alpha \sqrt{3})}{3\sqrt{3}} - \sum_{n \neq 0} \frac{t_0^2 J_n^2(\alpha)}{\omega n} \sin \frac{2\pi n}{3}, \quad (4.10)$$

where $\alpha = a_0 A_0$ characterizes the strength of the drive and J_n is the Bessel function of order n . We have $t_{\sigma} \sim t_0$ for small α and large ω . It is important to note that the spin symmetry of the static system (i.e, the energy-dispersion of Eq. (4.2) remaining the same under transformation $\sigma, \eta \rightarrow -\sigma, -\eta$) is now broken in the presence of the periodic driving. The polarization of the time dependent field breaks the TR symmetry of the Hamiltonian. The energy spectrum is thus given by

$$\epsilon_{\eta, \sigma}(k) = -\mu \pm \sqrt{t_{\sigma}^2 (k_x^2 + k_y^2) + \mathcal{D}_{\eta\sigma}^2}, \quad (4.11)$$

with the redefined mass term $\mathcal{D}_{\eta\sigma} = lE_z + 3\sqrt{3}\Lambda_{\sigma}^0$.

From this it is evident that in the region \mathcal{N} we have a tunable gap between the conduction and valence band given by $\delta\epsilon_{\eta\sigma} = 2|\mathcal{D}_{\eta\sigma}|$. The presence of three energy scales: the spin-orbit coupling, the staggered potential and the TR breaking mass from the driving gives rise to a rich topological phase diagram, where one can have trivial insulating, Chern insulating as well as spin hall insulating states, with topological phase transitions separating one phase from another [110]. In Fig. 4.3 we briefly summarize these points. It is also known that in this situation it is possible to achieve purely spin polarized low-energy band-structures [79], that would result in the suppression of AR.

4.3 Scattering matrix formalism

The quantum states can be found in both \mathcal{N} and \mathcal{S} region by solving the BdG equations in the respective regions. To compute the probability of Andreev reflection we match the wavefunctions for regions \mathcal{N} and \mathcal{S} at the boundary $x = 0$ in familiar fashion [59]:

$$\Psi^{e^-} + r\Psi^{e^+} + r_A\Psi^{h^+} = b\Psi^{S^+} + d\Psi^{S^-} \quad (4.12)$$

where Ψ^{e^-} and Ψ^{e^+} are the wave functions of the incident and reflected electron (in band η, σ). Ψ^{h^+} is the wavefunction of the reflected hole (in band $-\eta, -\sigma$):

$$\begin{aligned} \Psi^{e^\mp} &= \frac{e^{i(\mp k_e x + k_y y)}}{\sqrt{\cos \phi_i}} \begin{pmatrix} \xi_{\eta,\sigma}^{\frac{1}{4}} \\ \mp \frac{1}{\theta_{\eta,\sigma}} e^{\pm \frac{i\phi_i}{2}} \\ \eta \frac{\theta_{\eta,\sigma}^{\frac{1}{4}}}{\xi_{\eta,\sigma}^{\frac{1}{4}}} e^{\mp \frac{i\phi_i}{2}} \\ 0, 0 \end{pmatrix}^T, \\ \Psi^{h^+} &= \frac{e^{i(k_h x + k_y y)}}{\sqrt{\cos \phi'}} \begin{pmatrix} 0, 0, -\frac{\theta_{-\eta,-\sigma}^{\frac{1}{4}}}{\xi_{-\eta,-\sigma}^{\frac{1}{4}}} e^{-\frac{i\phi'}{2}}, \eta \frac{\xi_{-\eta,-\sigma}^{\frac{1}{4}}}{\theta_{-\eta,-\sigma}^{\frac{1}{4}}} e^{\frac{i\phi'}{2}} \end{pmatrix}^T, \end{aligned}$$

where

$$\xi_{\eta,\sigma} = \epsilon_{\eta,\sigma} + \mathcal{D}_{\eta\sigma}, \quad \theta_{\eta,\sigma} = \epsilon_{\eta,\sigma} - \mathcal{D}_{\eta\sigma}.$$

ϕ_i is the angle of incidence of the electron and ϕ' is the angle of the reflected hole given by

$$\begin{aligned} \cos \phi_i &= \frac{t_\sigma k_e}{\sqrt{\xi_{\eta,\sigma}} \sqrt{\theta_{\eta,\sigma}}}, \quad \tan \phi_i = \eta k_y / k_e, \\ \cos \phi' &= \frac{t_{-\sigma} k_h}{\sqrt{\xi_{-\eta,-\sigma}} \sqrt{\theta_{-\eta,-\sigma}}}, \quad \tan \phi' = \eta k_y / k_h. \end{aligned}$$

Here we have set $\mu = 0$. The incident angle ϕ_i has an upper limit for Andreev reflection to take place. This *critical angle* is given by

$$\phi_c = \sin^{-1} \frac{t_\sigma \sqrt{\xi_{-\eta,-\sigma}} \sqrt{\theta_{-\eta,-\sigma}}}{t_{-\sigma} \sqrt{\xi_{\eta,\sigma}} \sqrt{\theta_{\eta,\sigma}}}. \quad (4.13)$$

In the \mathcal{S} region, the relevant wavefunctions are

$$\Psi^{S^\pm} = e^{i((\pm k_0 - i\kappa)x + k_y y)} \begin{pmatrix} e^{\mp i\beta} \\ \pm \eta r_\pm e^{i(\pm \gamma \pm \mp \beta)} \\ 1 \\ \pm \eta r_\pm e^{\pm i\gamma \pm} \end{pmatrix}$$

with

$$\begin{aligned}\sin \gamma_{\pm}^{\eta,\sigma} &= \frac{(3/2)a_0\eta t_0 k_y}{\sqrt{\eta\sigma\lambda - U_0 \mp iQ}\sqrt{-\eta\sigma\lambda - U_0 \mp iQ}}, \\ r_{\pm}^{\eta,\sigma} &= \sqrt{\frac{-\eta\sigma\lambda - U_0 \mp iQ}{\eta\sigma\lambda - U_0 \mp iQ}}, \quad Q = \sqrt{|\Delta|^2 - \epsilon_{\eta,\sigma}^2}, \\ k_0 &= \frac{2\sqrt{M}}{3a_0\eta t_0}, \quad \kappa = \frac{2U_0Q}{3a_0\eta t_0\sqrt{M}}, \\ M &= U_0^2 - Q^2 - (\eta\sigma\lambda)^2 - \left(\frac{3a_0\eta t_0 k_y}{2}\right)^2.\end{aligned}$$

β is the phase associated with Andreev reflection and $\beta = \cos^{-1}(\epsilon/|\Delta|)$ for $\epsilon < \Delta$ and $\beta = -i \cosh^{-1}(\epsilon/|\Delta|)$ for $\epsilon > \Delta$. The solved parameters r and r_A , for each of the band, are elements of the scattering matrix of the system, where the probability of reflection and Andreev reflection are, respectively, $|r|^2$ and $|r_A|^2$. Finally, the differential conductance at the \mathcal{NS} junction is given by the Blonder-Tinkham-Klapwijk formula

$$G_{\eta,\sigma} = \int_0^{\pi/2} f_{\eta,\sigma}(\phi_i) \cos \phi_i d\phi_i, \quad (4.14)$$

where $f_{\eta,\sigma}(\phi_i) = (1 - |r|^2 + |r_A|^2)$ for each incident channel. For sub-gap conductance, as in our case, one can equivalently write $f_{\eta,\sigma}(\phi_i) \equiv 2|r_A|^2$, as $|r|^2 + |r_A|^2 = 1$ for each channel. Also, we note that G is measured with respect to the ballistic conductance of the \mathcal{N} system in absence of the superconductor.

Lastly, we would like to point out that under redefinition of parameters, the two Hamiltonians given in Eq. (4.3) and Eq. (4.8) are the same. So, the formalism of this section can be easily used to study the differential conductance in the geometries described in both Sec (4.1) and (4.2).

4.4 Spin-dependent Andreev reflection

For $\mu = 0$, in order for Andreev reflection to occur, the excitation gap in region \mathcal{N} must be smaller than the superconducting gap Δ . Thus, at $\alpha = 0$ and for a large-enough $lE_z \sim \mathcal{O}(\Delta)$, it is enough to consider only one pair of bands ($\eta\sigma = -1$) to participate in Andreev processes [81] and for incident energy larger than the gap of this pair of bands one expects AR to occur. Such a simplification is not possible for finite α as the degeneracy among the bands is now lifted. An electron coming in the band of η, σ Andreev reflects to the band with indices $-\eta, -\sigma$. This provides us with a condition that the AR is allowed only when

$$\Delta \geq E \geq \max\{\delta\epsilon_{\sigma\eta}, \delta\epsilon_{-\sigma-\eta}\}. \quad (4.15)$$

As an example, for the case considered in Fig. 4.3, for $\alpha = 0.4$, although the band $\sigma =$

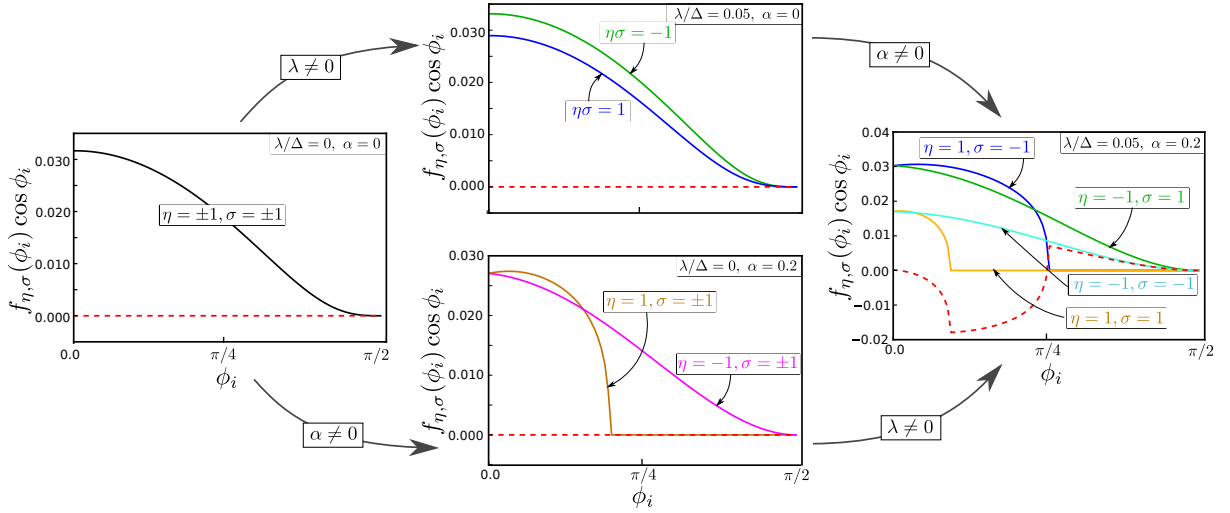


Figure 4.6: Appearance of spin-dependent AR in presence of both the spin-orbit coupling ($\lambda \neq 0$) and periodic driving ($\alpha \neq 0$). We plot the angle resolved sub-gap ($E/\Delta = 0.4$) conductance $f_{\eta,\sigma}(\phi_i)$ (c.f. Eq. (4.14)) as a function of the incident angle ϕ_i for all the channels available ($\eta = \pm 1, \sigma = \pm 1$), as marked individually. The resultant spin-current is plotted in dashed (red) line. Non-vanishing λ prefers two (given by $\eta\sigma = -1$) out of the four channels. Whereas, non-vanishing α prefers one valley (here, $\eta = +1$). In combination of both present, we observe spin-dependent AR. $lE_z = 0.25\Delta$, $\omega = 10t_0$ and $\Delta/t_0 = 0.1$ are kept fixed.

$-1, \eta = +1$ is gapless (i.e., $\delta\epsilon_{+\downarrow} = 0$), the AR takes place only when $E \geq \delta\epsilon_{-\uparrow}$. This simply implies that in a purely spin-polarized band-structure AR is prohibited (i.e., in a range of energy from $\min\{\delta\epsilon_{\sigma\eta}, \delta\epsilon_{-\sigma-\eta}\}$ to $\max\{\delta\epsilon_{\sigma\eta}, \delta\epsilon_{-\sigma-\eta}\}$). Any occurrence of spin-dependent AR is still not evident yet. However, this does not prohibit the probabilities of the AR in various channels to differ from each other as long as E satisfies Eq. (4.15).

Before we discuss the Haldane model, we first study the case of the driven system. We start by briefly summarizing the results of the static system in the upper panel of Fig. 4.4. Introduction of the spin-orbit coupling term λ breaks the four-fold degeneracy of the Dirac points, but keeps the band-structure symmetric with respect to $\eta, \sigma \rightarrow -\eta, -\sigma$. Further, due to the presence of the sub-lattice staggered potential lE_z , the two branches $\eta\sigma = \pm 1$ are now separated by a gap. Consequently, for $lE_z \sim \lambda$, it becomes sufficient to consider only one of the $\eta\sigma$ branches for low-energy transport. The λ term in Eq. (4.2) does not break the TR symmetry and for $lE_z < \lambda$, the system is a spin-hall insulator with opposite Chern numbers for up and down-spin valence bands. For $lE_z > \lambda$ the system becomes a trivial insulator. As the spin-valley symmetry remains intact, the AR probability remains independent of spin. One can compare these results with that of Ref. [81].

Breaking the TR symmetry by introducing the driving (characterized by the amplitude α) has dramatic consequence in Andreev reflection. We summarize the results depicting spin-dependent AR probabilities in the lower panel of Fig. 4.4 and in Fig. 4.5. In the presence of $\alpha \neq 0$, the four bands ($\sigma = \pm 1, \eta = \pm 1$) are now split and there exists a range of energy that does not satisfy Eq. (4.15). When the energy E is larger than this forbidden energy, each of the previously

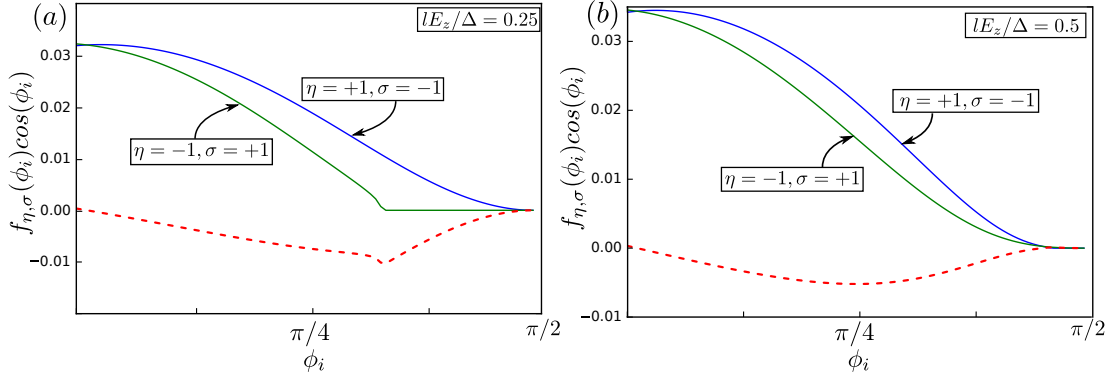


Figure 4.7: (a) The angle resolved sub-gap conductance $f_{\eta,\sigma}(\phi_i)$ is plotted as a function of the incident angle ϕ_i and the resultant spin-resolved conductance is plotted with dashed lines. Only $\eta\sigma = -1$ branches contribute for our choice of parameters: $E = 0.6\Delta$, $\lambda = 0.5\Delta$, $\Delta = 0.1t_0$, $lE_z = 0.25\Delta$. (b) Same plot for $lE_z = 0.5\Delta$. Other parameter values remain unchanged from Fig. 4.4.

equivalent spin channels labeled by the value of $\eta\sigma$ acquires different probabilities of Andreev reflection. Consequently the conductance G becomes spin-dependent. Even for $lE_z = 0$, the four channels $\eta = \pm 1$, $\sigma = \pm 1$ are now split and a significant spin-conductance can be observed. With increasing lE_z , only two channels, given by $\eta\sigma = -1$ remain relevant in the subgap regime, which continue to carry large spin conductance. For our numerical results, we keep $\omega = 10t_0$, which is almost double of the band-width of the system. This is well within the regime where the high-frequency approximation is expected to be valid.

Our results show spin-dependent conductance even for a comparatively small value of α/t_0 . This is because a finite spin-dependent AR appears due to the competition between the two terms in Eq. (4.10) (see the discussion below). The second term appearing in Λ_σ (see Eq. (4.10)) needs to be of the order of λ (the spin-orbit coupling strength) for this spin dependence to show up. In our simulation we have taken $\lambda = 0.05t_0$. In typical systems, λ is quite small, for example, the value of λ in silicene is only 3.9 meV whereas $t_0 \approx 1.6$ eV [116], giving a value $\lambda/t_0 \approx 2.5 \times 10^{-3}$. We expect the relevant value of α/t_0 to be of the same order for such a system.

With increasing α , the system eventually develops a gap (a topological insulator with Chern number = ± 2 , see Fig. 4.3) bigger than Δ and consequently the sub-gap conductance vanishes. Interestingly, the maximum spin-conductance observed depends only weakly on α . These results are summarized in Fig. 4.5.

Now we turn to further analysis of the origin of spin-dependent AR in our system. For that, we study how the angle dependent differential conductance $f_{\eta,\sigma}(\phi_i)$ behaves as a function of the incident angle ϕ_i . As shown in Fig. 4.6, a finite value of λ and α is achieved via two different intermediate states. The action of a finite λ prefers two channels ($\eta\sigma = -1$ for this case) out of four. Whereas, a finite α results in a critical angle $\phi_c < \pi/2$ for channels belonging to one of the valley ($\eta = 1$), giving rise to net conductance dominated by channels of the other valley

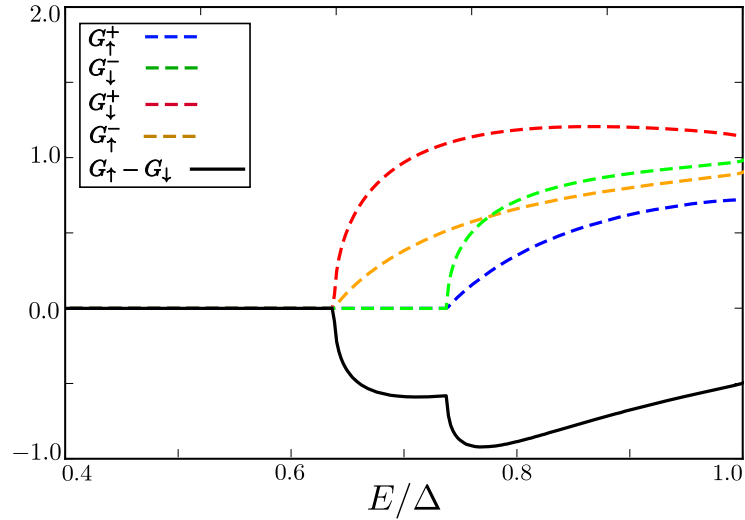


Figure 4.8: The conductances of an electron when the TRS is broken by complex NNN hoppings as is shown in Eq. (4.3). The parameters taken are $t_2 = 0.005t_0$, $\theta = \pi/4$, $lE_z = 0.005t_0$, $\Delta = 0.1t_0$, $\lambda = 0.05t_0$.

($\eta = -1$). Now, in the $\eta\sigma = -1$ channel consisting $\eta = 1, \sigma = -1$ and $\eta = -1, \sigma = 1$, the effect of driving, for the parameter range presented in Fig. 4.6, is a finite critical angle of the $\eta = 1, \sigma = -1$ channel, making the net conductance spin-dependent. Thus, when both the effects are present, it becomes clear that the sub-gap conductance has spin-dependence. The angle resolved conductance study also hints at achieving a purely spin polarized sub-gap transport at a range of collimation angle of the incident electron. The angle-resolved sub-gap conductance in the parameter range of Fig. 4.4 is presented in Fig. 4.7 for a sample value of the incident energy.

In case of generating the mass in a periodically driven setup, we neglect any other degrees of freedom present in the system (such as phonon and the effect of the substrate), which may limit our prediction for a realistic setup. The heating, when driving with frequency larger than the band width is likely to be negligible [107, 118–120] but may require appropriate cooling of the substrate. Despite the advantage of periodic drive in terms of the tunability of the time-reversal broken mass term, the time dependent drive has significant limitation in solid state systems, where a periodic drive, in presence of interaction, can heat the system eventually.

Lastly, the same study is repeated for the Haldane model introduced in Sec. 4.1. The results are summarized in Fig. 4.8. As expected, the spin asymmetry due to the next-nearest-neighbor hopping, results in spin-dependent Andreev reflection amplitudes which can be tuned by t_2 and θ .

4.5 Summary

To summarize, we consider a simple Dirac system in the presence of a number of mass terms that may compete with one another. In such a system the Andreev reflection probability, hence

the sub-gap conductance, at the interface with a superconductor becomes spin-dependent. It is possible to achieve, as we see in Fig. 4.6, sub-gap spin dependent transport. If we consider the case where the time-reversal broken mass term is introduced by circularly polarized light, it is possible to control the spin-dependence, by controlling the amplitude of drive α , frequency ω and the handedness of the radiation. Our work is a proof of concept how spin-dependent AR can be achieved and has direct implication in practical systems like silicene, germanene and stanene, as well as in cold-atomic setup.

Chapter 5

Spin waves in MoS₂

Recently, it has been argued that for strong enough interactions, TMD systems develop a spontaneous imbalance of spin/valley populations [121, 122], which leads to actual ferromagnetic spin order in the groundstate. It thus becomes interesting to consider how one might probe and distinguish these orderings. One possible strategy is to investigate the spin response of the system, both to search for sharp collective modes that are a hallmark of ferromagnets, and to understand broader features of the response that demonstrate the ordering present in these materials. This is the subject of our study.

At higher dopings the valence bands will support two Fermi surfaces in each valley, indicating that they contain holes of both spins. Because of the opening of the second Fermi surface the system now supports gapless spin-flip excitations, albeit at finite wavevector. Regions in frequency and wavevector where these exist are illustrated in Fig. 5.2, along with the spin wave dispersion for these parameters. Observation of such a continuum of gapless modes would allow a direct demonstration of the spin-split Fermi surfaces in this system. In practice, because these modes appear above wavevectors of order $q \lesssim 1/a$ with a the lattice constant, their presence may be difficult to observe by direct electromagnetic absorption because of momentum conservation. In real systems, disorder relaxes this constraint and may make their detection feasible [123].

This chapter is organized as follows. In Section 5.1 we describe both the single particle Hamiltonian and the interaction model we adopt for this system. Section 5.2 describes a static Hartree-Fock analysis of the system, demonstrating that the effective single-particle Hamiltonian is rather similar to the non-interacting one, with renormalized parameters. In Section 5.3 we carry out a time-dependent Hartree-Fock analysis of the spin response function, and show how one can identify poles that signal allowed spin-flip excitations of the system. In Section 5.4 we carry out an analytic analysis of the equations generated in the previous section, appropriate for low hole doping. Section 5.5 provides results one finds from numerical solutions for the spin response functions. We conclude with a summary in Section 5.6.

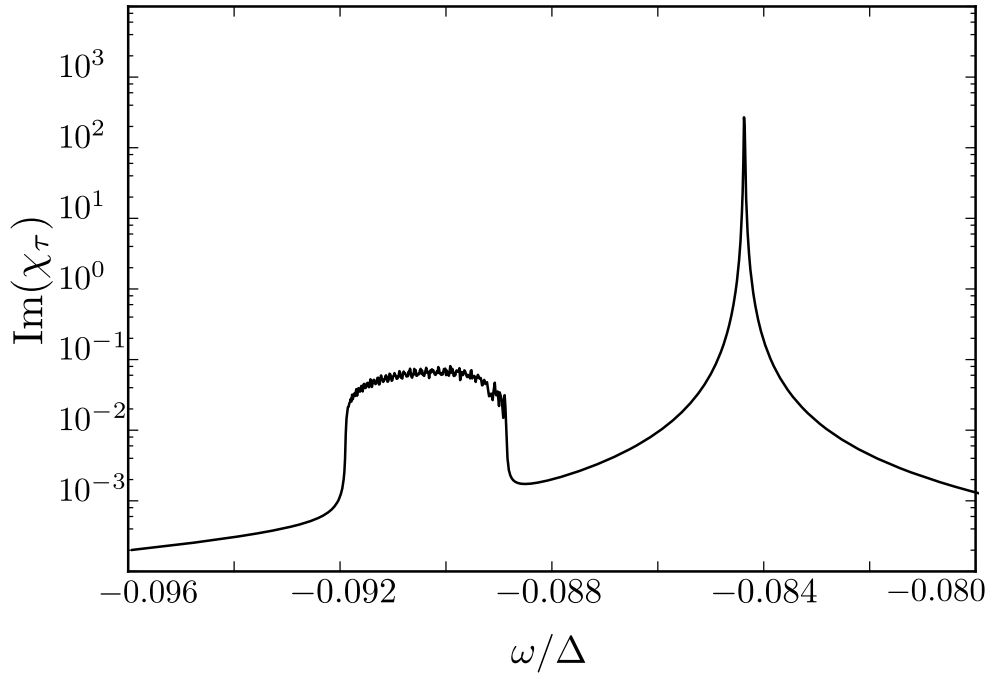


Figure 5.1: Absorptive part of spin response function $\text{Im } \chi_\tau(\mathbf{q}, \omega)$ for $\mathbf{q} = 0$, chemical potential $\mu_0 = -0.49\Delta$ and $U_0 = 0.2\text{eV}$ with $\tau = +1$. Model parameters for band structure in Table I. A sharp collective mode near $\omega \approx -0.0845\Delta$ is prominent above a particle-hole continuum in the interval $-0.092 \lesssim \omega/\Delta \lesssim -0.087$.

5.1 Model of the system

Our starting point is a simple two-band Hamiltonian for the monolayer MX_2 , such as MoS_2 , developed through several numerical, symmetry-based analyses [12] which capture the electronic properties near the $K, -K$ valleys. In the absence of interactions this has the form

$$H_0^\tau(\mathbf{k}) = \begin{bmatrix} \Delta/2 & at(\tau k_x - ik_y) \\ at(\tau k_x + ik_y) & -\Delta/2 + s\tau\lambda \end{bmatrix}, \quad (5.1)$$

which is written in the basis $|\psi_c^\tau\rangle = |d_{z^2}\rangle$ and $|\psi_v^\tau\rangle = \frac{1}{\sqrt{2}}(|d_{x^2-y^2}\rangle + i\tau|d_{xy}\rangle)$, where $\tau = \pm$ is the valley index and $d_{z^2}, d_{x^2-y^2}, d_{xy}$ are orbitals of the M atoms. (Here and throughout this chapter we take $\hbar = 1$.) Spin is a good quantum number, denoted by $s = 1$ for \uparrow and $s = -1$ for \downarrow . The strength of spin-orbit coupling is encoded in the parameter λ . In the ground state of this Hamiltonian, states up to the chemical potential μ_0 , which is tunable in principle via gating, are filled. Estimates [36] for the parameters relevant to MoS_2 are listed in Table I.

a	t	Δ	λ
3.190 Å	1.059 eV	1.66 eV	0.075 eV

Table 5.1: Values of various parameters for MoS_2 from Ref. [12].

The energy eigenstates of the full Hamiltonian with momentum \mathbf{k} and spin s will be denoted

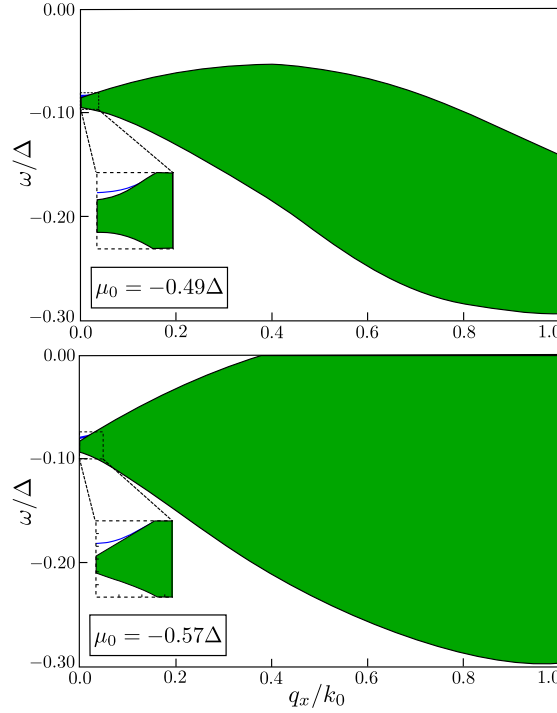


Figure 5.2: The top panel, for $\mu_0 = -0.49\Delta$, in which there is only a single Fermi surface in the valley, has a continuum of particle-hole excitations (shown in green) below some minimum frequency. The lower panel has $\mu_0 = -0.57\Delta$ for which there are two Fermi surfaces in the valley, giving rise to the continuum modes with vanishingly small energies for $q_x > 0.4k_0$ with $k_0 = \Delta/2ta$. For both panels, $U_0 = 0.2\text{eV}$ and $\tau = +1$. Other parameters are listed in Table I. Blue lines illustrate the collective spin wave mode dispersion.

by $\phi_{l,s}(\mathbf{k})$, with $l = \{\tau, \alpha\}$ ($\alpha = \pm$ for conduction/valence bands), and have the form

$$\phi_{l,s}(\mathbf{k}) = \frac{1}{\sqrt{2}} \begin{pmatrix} \tau e^{-i\tau\phi} \sqrt{1 + \frac{\alpha m_{s\tau}}{\sqrt{m_{s\tau}^2 + a^2 t^2 k^2}}} \\ \alpha \sqrt{1 - \frac{\alpha m_{s\tau}}{\sqrt{m_{s\tau}^2 + a^2 t^2 k^2}}} \end{pmatrix}, \quad (5.2)$$

with corresponding eigenvalues

$$\epsilon_{l,s}^\alpha(\mathbf{k}) = \frac{\tau s \lambda}{2} + \alpha \sqrt{m_{s\tau}^2 + (atk)^2}, \quad (5.3)$$

where $m_{s\tau} = \frac{\Delta - \tau s \lambda}{2}$ and $k = \sqrt{k_x^2 + k_y^2}$. The bands near the K ($\tau = 1$) valley, shown in Fig. 5.3, illustrate the distinct spin structure of the system. The valence and conduction band are separated by a relatively large gap $E_g = (\Delta - \lambda)$ at $k = 0$, whereas the two spin valence bands are further separated by a smaller gap of magnitude $E_\lambda = 2\lambda$. This gap between the spin-split valence bands remains almost constant for a range of k until $akt \gg \Delta$. Note that the two conduction bands of the model are nearly degenerate. The K and $-K$ valleys of the system are related by time-reversal, so that the spins of the two bands are reversed in going from one to the other.

To write down an effective interaction, it is convenient to define field operators of spin s

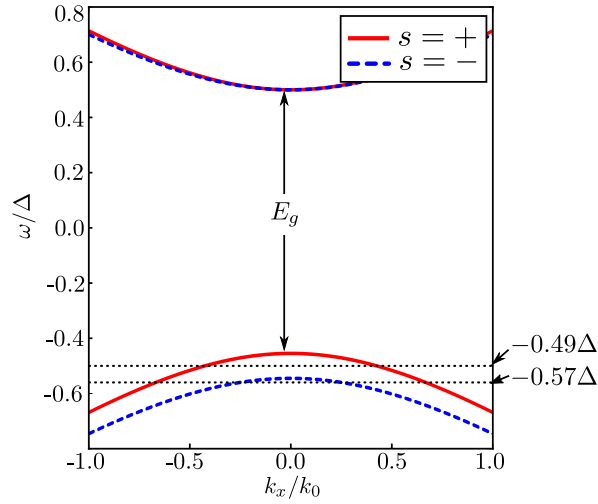


Figure 5.3: The band dispersion of Hamiltonian (5.1) showing a direct band gap E_g between the valence and the conduction band and the separation of spin polarized bands in the conduction band. Position for two of μ_0 are marked on the right margin. $k_0 = \Delta/2ta$ is the scale of momentum. The parameters used are listed in Table 1 and $\tau = +1$.

projected into the set of states defined in our model,

$$\Psi_s(\mathbf{r}) = \frac{1}{\sqrt{L_x L_y}} \sum_{\mathbf{k}, l} e^{i(\mathbf{k} + \mathbf{K}_{\tau_l}) \cdot \mathbf{r}} \phi_{l,s}(\mathbf{k}) c_{l,s}(\mathbf{k}), \quad (5.4)$$

where $c_{l,s}(\mathbf{k})$ is the annihilation operator for the l, s state at momentum \mathbf{k} relative to the valley minima/maxima at $\mathbf{K}_{\tau_l} = \tau_l \mathbf{K}$, with the sign determined by the τ index implicit in l , and $L_x L_y$ is the area of the system. A repulsive interaction among the band-electrons can then be represented in the form

$$H_{\text{int}} = \frac{1}{2} \sum_{s,s'} \int d^2 \mathbf{r} d^2 \mathbf{r}' V(\mathbf{r} - \mathbf{r}') : \Psi_s^\dagger(\mathbf{r}) \Psi_s(\mathbf{r}) \Psi_{s'}^\dagger(\mathbf{r}') \Psi_{s'}(\mathbf{r}') :, \quad (5.5)$$

with V represents a finite-range repulsive interaction. Physically this arises from Coulomb interactions among the band electrons; the finite range can be provided by a screening gate or by carriers in the layer itself (although we will not treat the screening dynamically in what follows). We assume the screening length is large on the scale of the lattice constant so that inter-valley contributions to the density $\Psi_s^\dagger(\mathbf{r}) \Psi_s(\mathbf{r})$ oscillate rapidly, and can be ignored when integrated over \mathbf{r} . This leads to the replacement

$$H_{\text{int}} \rightarrow \frac{1}{2} \sum_{s,s'} \sum_{\tau,\tau'} \int d^2 \mathbf{r} d^2 \mathbf{r}' V(\mathbf{r} - \mathbf{r}') : \Psi_{s\tau}^\dagger(\mathbf{r}) \Psi_{s\tau}(\mathbf{r}) \Psi_{s'\tau'}^\dagger(\mathbf{r}') \Psi_{s'\tau'}(\mathbf{r}') :, \quad (5.6)$$

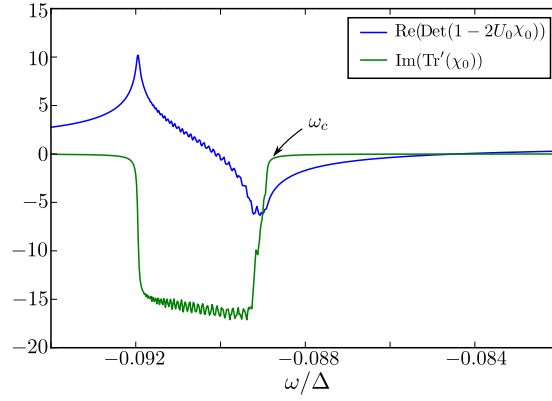


Figure 5.4: Plot of a typical $\chi(\mathbf{q}, \omega)$, Eq. (5.27), showing the particle-hole excitations of the spin-split valence bands below an energy ω_c . There is a single collective mode visible for which the real part of the denominator of Eq. (5.27) is zero. Here we have used $\mathbf{q} = \mathbf{0}$, $\mu_0 = -0.49\Delta$, $\tau = +1$ and $U_0 = 0.2\text{eV}$.

with

$$\Psi_{s\tau}(\mathbf{r}) = \frac{1}{\sqrt{L_x L_y}} \sum_{\mathbf{k}, l} e^{i\mathbf{k}\cdot\mathbf{r}} \phi_{l,s}(\mathbf{k}) c_{l,s}(\mathbf{k}) \delta_{\tau, \tau_l}, \quad (5.7)$$

where τ_l is the valley content of the composite l index. At this point we can make the approximation $V(\mathbf{r} - \mathbf{r}') = 2U_0\delta^2(\mathbf{r} - \mathbf{r}')$, and arrive at an interaction form

$$H_{\text{int}} = U \sum_{\{l_i, \mathbf{k}_i, \mathbf{q}\}} \sum_{s, s'} \phi_{l_1 s}^\dagger(\mathbf{k}_1) \phi_{l_2 s'}^\dagger(\mathbf{k}_2) \phi_{l_3 s'}(\mathbf{k}_2 + \mathbf{q}') \phi_{l_4 s}(\mathbf{k}_1 - \mathbf{q}') \\ c_{l_1 s}^\dagger(\mathbf{k}_1) c_{l_2 s'}^\dagger(\mathbf{k}_2) c_{l_3 s'}(\mathbf{k}_2 + \mathbf{q}') c_{l_4 s}(\mathbf{k}_1 - \mathbf{q}') \delta_{\tau_1, \tau_4} \delta_{\tau_2, \tau_3}, \quad (5.8)$$

where $U = \frac{U_0}{L_x L_y}$. This is the interaction Hamiltonian that we use in the Hartree-Fock analyses that follow.

5.2 Hartree-Fock Approximation

In order to carry out an analysis of the spin response in this system within the time-dependent Hartree-Fock approximation, it is first necessary to find the density matrix of the system within the static Hartree-Fock (HF) approximation. This has the form

$$\langle c_{l_s}^\dagger(\mathbf{k}) c_{l' s'}(\mathbf{k}') \rangle = n_{l_s}(\mathbf{k}) \delta_{ll'} \delta_{ss'} \delta_{\mathbf{k}, \mathbf{k}'}. \quad (5.9)$$

Note in writing this, we have assumed that neither interband nor intervalley coherence have formed in the system spontaneously. Performing a HF decomposition on Eq. (5.8) gives a

potential for an effective single-body Hamiltonian,

$$H_{\text{int}}^{\text{HF}} = -2U \sum_{l',ss',\mathbf{k}} \delta_{ss'} \sum_{a,b=A/B} c_{l's}^{\dagger} \phi_{l's}^{a*}(\mathbf{k}) \times \left(\sum_{l''} \phi_{l's}^a(\mathbf{k}) n_{l''s}(\mathbf{k}) \phi_{l''s}^{b*}(\mathbf{k}) \right) \phi_{l's}^b(\mathbf{k}) c_{l's}. \quad (5.10)$$

where, for notational simplicity, we have used the a, b indices to denote the orbital degree of freedom ($A \equiv |d_{z^2}\rangle$ and $B \equiv \frac{1}{\sqrt{2}}(|d_{x^2-y^2}\rangle + i\tau|d_{xy}\rangle$). The full HF Hamiltonian for electrons with wavevector \mathbf{k} then becomes

$$H_{l_s, l'_s}^{0, \text{HF}}(\mathbf{k}) = H_{l_s, l'_s}^0(\mathbf{k}) - 2U \sum_{ab} \phi_{l_s}^{a*}(\mathbf{k}) n_s^{ab} \phi_{l'_s}^b(\mathbf{k}), \quad (5.11)$$

with $n_{s\tau_i}^{ab} = \sum_{\mathbf{k}l} \phi_{l_s}^a(\mathbf{k}) n_{l_s}(\mathbf{k}) \phi_{l_s}^{b*}(\mathbf{k})$. The quantities n_{l_s} need to be determined self-consistently. Note in writing $H_{l_s, l'_s}^{0, \text{HF}}(\mathbf{k})$, we have dropped a term proportional to the total fermion number which is a constant. In the orbital basis (l, l') one may write

$$H^{0, \text{HF}}(\mathbf{k}) = \begin{bmatrix} \tilde{m}_{s\tau} & at\tau k e^{-i\tau\phi} \\ at\tau k e^{i\tau\phi} & -\tilde{m}_{s\tau} \end{bmatrix} + \tau s \lambda / 2 - U(n_{s\tau}^{AA} + n_{s\tau}^{BB}), \quad (5.12)$$

with renormalized mass $\tilde{m}_{s\tau} = \frac{\Delta - \tau s \lambda}{2} - U(n_{s\tau}^{AA} - n_{s\tau}^{BB})$. For a fixed density (obtained by fixing μ_0), the value of $\tilde{m}_{s\tau}$ is found numerically using the requirement that the values $n_{l_s}(k)$ used to generate Eq. (5.12) yield wavefunctions that produce the very same values – i.e., the density matrix used to generate the HF Hamiltonian is the same as what one finds from its eigenvectors and eigenvalues. In the present case, the wavefunctions have a functional form that is the same as that of the free wavefunctions, Eq. (5.2), with modified parameters:

$$\phi_{l,s}(\mathbf{k}) = \frac{1}{\sqrt{2}} \begin{pmatrix} \tau e^{-i\tau\phi} \sqrt{1 + \frac{\alpha \tilde{m}_{s\tau}}{\sqrt{\tilde{m}_{s\tau}^2 + a^2 t^2 k^2}}} \\ \alpha \sqrt{1 - \frac{\alpha \tilde{m}_{s\tau}}{\sqrt{\tilde{m}_{s\tau}^2 + a^2 t^2 k^2}}} \end{pmatrix}. \quad (5.13)$$

The energy eigenvalues then become

$$\tilde{\epsilon}_{l,s}(\mathbf{k}) = \frac{\tau s \lambda}{2} + \alpha \sqrt{\tilde{m}_{s\tau}^2 + (atk)^2} - U(n_{\tau s}^{AA} + n_{\tau s}^{BB}), \quad (5.14)$$

which is similar but not identical to the non-interacting energy eigenvalues, Eq. (5.3). Here, in analogy with the previous section, the index $l = \{\tau, \alpha\}$ implicitly contains the valley index τ as well as the conduction/valence band index $\alpha = \pm 1$. In the remainder of this chapter, we will use these as the basis states for our analysis.

5.3 Time dependent Hartree-Fock Approximation

Our focus in this study is the spin-spin response function

$$\chi_\tau(\mathbf{r} - \mathbf{r}', t) = -i\Theta(t)\langle[\rho_\tau^{+-}(\mathbf{r}, t), \rho_\tau^{-+}(\mathbf{r}', 0)]\rangle, \quad (5.15)$$

with $\rho_\tau^{\sigma\sigma'}(\mathbf{r}, t) = \Psi_{\sigma\tau}^{\text{HF}\dagger}(\mathbf{r}, t)\Psi_{\sigma'\tau}^{\text{HF}}(\mathbf{r}, t)$, with field operators

$$\Psi_{s\tau}^{\text{HF}}(\mathbf{r}) = \frac{1}{\sqrt{L_x L_y}} \sum_{\mathbf{k}, l} e^{i\mathbf{k}\cdot\mathbf{r}} \phi_{l,s}(\mathbf{k}) c_{l,s}(\mathbf{k}) \delta_{\tau, \tau_l}. \quad (5.16)$$

The single particle states appearing in this expression are the HF wavefunctions, Eq. (5.13). We do not consider intervalley particle-hole operators as this would involve large momentum imparted to the system. Assuming translational invariance, in momentum space the response function has the form

$$\begin{aligned} \chi_\tau(\mathbf{q}, t) &= -\frac{i\Theta(t)}{L_x L_y} \sum_{\{\mathbf{k}_i, \mathbf{q}_i, l_i\}} f_{l_1 l_2, \uparrow\downarrow}(\mathbf{k}_1 + \mathbf{q}, \mathbf{k}_1) f_{l_3 l_4, \downarrow\uparrow}(\mathbf{k}_2 - \mathbf{q}, \mathbf{k}_2) \\ &\quad \langle [e^{iHt} c_{l_1 \uparrow}^\dagger(\mathbf{k}_1 + \mathbf{q}) c_{l_2 \downarrow}(\mathbf{k}_1) e^{-iHt}, c_{l_3 \downarrow}^\dagger(\mathbf{k}_2 - \mathbf{q}) c_{l_4 \uparrow}(\mathbf{k}_2)] \rangle \\ &\equiv \frac{1}{L_x L_y} \sum_{\{\mathbf{k}_i, \mathbf{q}_i, l_i\}} f_{l_1 l_2, \uparrow\downarrow}(\mathbf{k}_1 + \mathbf{q}, \mathbf{k}_1) f_{l_3 l_4, \downarrow\uparrow}(\mathbf{k}_2 - \mathbf{q}, \mathbf{k}_2) \tilde{\chi}_{l_1 l_2 l_3 l_4}(\mathbf{k}_1, \mathbf{k}_2, \mathbf{q}, t), \end{aligned} \quad (5.17)$$

with

$$\tilde{\chi}_{l_1 l_2 l_3 l_4}(\mathbf{k}_1, \mathbf{k}_2, \mathbf{q}, t) = -i\Theta(t)\langle [e^{iHt} c_{l_1 \uparrow}^\dagger(\mathbf{k}_1 + \mathbf{q}) c_{l_2 \downarrow}(\mathbf{k}_1) e^{-iHt}, c_{l_3 \downarrow}^\dagger(\mathbf{k}_2 - \mathbf{q}) c_{l_4 \uparrow}(\mathbf{k}_2)] \rangle. \quad (5.18)$$

It is implicit that the τ_l content of each l index on the right hand side of this equation is a single value of τ , and the Hamiltonian appearing in the $e^{\pm iHt}$ factors is $H = H_0 + H_{\text{int}}$, using Eqs. (5.1) and (5.8). The weights $f_{l_i l_j, \sigma\sigma'}(\mathbf{k}_1, \mathbf{k}_2) \equiv \phi_{l_i \sigma}^\dagger(\mathbf{k}_1) \phi_{l_j \sigma'}(\mathbf{k}_2)$ are wavefunction overlap factors, and the indices l_i have allowed values $\tau_l = \pm 1$ and $\alpha_l = \pm 1$.

The equation of motion of $\tilde{\chi}$, Eq. (5.18), is

$$\begin{aligned} i\partial_t \tilde{\chi}_{l_1 l_2 l_3 l_4}(\mathbf{k}_1, \mathbf{k}_2, \mathbf{q}, t) &= \{n_{l_1 \uparrow}(\mathbf{k}_1 + \mathbf{q}) - n_{l_2 \downarrow}(\mathbf{k}_1)\} \delta_{l_1 l_4} \delta_{l_2 l_3} \delta_{\mathbf{k}_1, \mathbf{k}_2 - \mathbf{q}} \\ &\quad + i\Theta(t) \langle [[H_0, c_{l_1 \uparrow}^\dagger(\mathbf{k}_1 + \mathbf{q}) c_{l_2 \downarrow}(\mathbf{k}_1)](t), c_{l_3 \downarrow}^\dagger(\mathbf{k}_2 - \mathbf{q}) c_{l_4 \uparrow}(\mathbf{k}_2)] \rangle \\ &\quad + i\Theta(t) \langle [[H_{\text{int}}, c_{l_1 \uparrow}^\dagger(\mathbf{k}_1 + \mathbf{q}) c_{l_2 \downarrow}(\mathbf{k}_1)](t), c_{l_3 \downarrow}^\dagger(\mathbf{k}_2 - \mathbf{q}) c_{l_4 \uparrow}(\mathbf{k}_2)] \rangle. \end{aligned} \quad (5.19)$$

The first commutator reads

$$[H_0, c_{l_1\uparrow}^\dagger(\mathbf{k}_1 + \mathbf{q})c_{l_2\downarrow}(\mathbf{k}_1)] = \sum_l h_{ll_1,\uparrow}^0(\mathbf{k}_1 + \mathbf{q})c_{l_1\uparrow}^\dagger(\mathbf{k}_1 + \mathbf{q})c_{l_2\downarrow}(\mathbf{k}_1) - \sum_{l'} h_{l_2l',\downarrow}^0(\mathbf{k}_1)c_{l_1\uparrow}^\dagger(\mathbf{k}_1 + \mathbf{q})c_{l'\downarrow}(\mathbf{k}_1). \quad (5.20)$$

The first commutator appearing in the last term of Eq. (5.19) is

$$\begin{aligned} & \left[H_{\text{int}}, c_{l_1\uparrow}^\dagger(\mathbf{k}_1 + \mathbf{q})c_{l_2\downarrow}(\mathbf{k}_1) \right] \\ &= 2U \sum_{\{l_i, \mathbf{k}_i\}} \left[f_{l_6l_7,\uparrow\uparrow}(\mathbf{k}_6, \mathbf{k}_6 + \mathbf{q}')f_{l_5l_8,\uparrow\uparrow}(\mathbf{k}_5, \mathbf{k}_5 - \mathbf{q}')c_{l_5\uparrow}^\dagger(\mathbf{k}_5)c_{l_6\uparrow}^\dagger(\mathbf{k}_6)c_{l_7\uparrow}(\mathbf{k}_6 + \mathbf{q}')c_{l_2\downarrow}(\mathbf{k}_1)\delta_{l_1,l_8}\delta_{\mathbf{k}_5-\mathbf{q}',\mathbf{k}_1+\mathbf{q}} \right. \\ & \quad + f_{l_6l_7,\downarrow\downarrow}(\mathbf{k}_6, \mathbf{k}_6 + \mathbf{q}')f_{l_5l_8,\downarrow\downarrow}(\mathbf{k}_5, \mathbf{k}_5 - \mathbf{q}')c_{l_1\uparrow}^\dagger(\mathbf{k}_1 + \mathbf{q})c_{l_5\downarrow}^\dagger(\mathbf{k}_5)c_{l_7\downarrow}(\mathbf{k}_6 + \mathbf{q}')c_{l_8\downarrow}(\mathbf{k}_5 - \mathbf{q}')\delta_{l_2,l_6}\delta_{\mathbf{k}_1,\mathbf{k}_6} \\ & \quad - f_{l_6l_7,\uparrow\uparrow}(\mathbf{k}_6, \mathbf{k}_6 + \mathbf{q}')f_{l_5l_8,\downarrow\downarrow}(\mathbf{k}_5, \mathbf{k}_5 - \mathbf{q}')c_{l_5\downarrow}^\dagger(\mathbf{k}_5)c_{l_6\uparrow}^\dagger(\mathbf{k}_6)c_{l_8\downarrow}(\mathbf{k}_5 - \mathbf{q}')c_{l_2\downarrow}(\mathbf{k}_1)\delta_{l_1,l_7}\delta_{\mathbf{k}_1+\mathbf{q},\mathbf{k}_6+\mathbf{q}'} \\ & \quad \left. - f_{l_6l_7,\uparrow\uparrow}(\mathbf{k}_6, \mathbf{k}_6 + \mathbf{q}')f_{l_5l_8,\downarrow\downarrow}(\mathbf{k}_5, \mathbf{k}_5 - \mathbf{q}')c_{l_1\uparrow}^\dagger(\mathbf{k}_1 + \mathbf{q})c_{l_6\uparrow}^\dagger(\mathbf{k}_6)c_{l_7\uparrow}(\mathbf{k}_6 + \mathbf{q}')c_{l_8\downarrow}(\mathbf{k}_5 - \mathbf{q}')\delta_{l_2,l_5}\delta_{\mathbf{k}_1,\mathbf{k}_6} \right]. \end{aligned} \quad (5.21)$$

Here, for notational simplicity, we have absorbed the $\delta_{\tau_i\tau_j}$ factors inside the $f_{l_i l_j}$ s. Hence, we end up with terms involving 2, 4, and 6 fermion operators. We approximate the last of these using a HF decomposition [124] and find that the $\mathbf{q}' = 0$ terms cancel each other. The other terms are

$$\begin{aligned} & \left[H_{\text{int}}, c_{l_1\uparrow}^\dagger(\mathbf{k}_1 + \mathbf{q})c_{l_2\downarrow}(\mathbf{k}_1) \right] \\ \rightarrow & -2U \sum_{\{l_i, \mathbf{k}_i\}} \left[f_{l_6l_5,\uparrow\uparrow}(\mathbf{k}_1 + \mathbf{q}, \mathbf{k}_1 + \mathbf{q} + \mathbf{q}')f_{l_5l_1,\uparrow\uparrow}(\mathbf{k}_1 + \mathbf{q} + \mathbf{q}', \mathbf{k}_1 + \mathbf{q})n_{l_5\uparrow}(\mathbf{k}_1 + \mathbf{q} + \mathbf{q}')c_{l_6,\uparrow}^\dagger(\mathbf{k}_1 + \mathbf{q})c_{l_2,\downarrow}(\mathbf{k}_1) \right. \\ & \quad + f_{l_2l_5,\downarrow\downarrow}(\mathbf{k}_1, \mathbf{k}_1 + \mathbf{q}')f_{l_5l_8,\downarrow\downarrow}(\mathbf{k}_1 + \mathbf{q}', \mathbf{k}_1)n_{l_5\downarrow}(\mathbf{k}_1 + \mathbf{q}')c_{l_1,\uparrow}^\dagger(\mathbf{k}_1 + \mathbf{q})c_{l_8,\downarrow}(\mathbf{k}_1) \\ & \quad - f_{l_6l_1,\uparrow\uparrow}(\mathbf{k}_1 + \mathbf{q} - \mathbf{q}', \mathbf{k}_1 + \mathbf{q})f_{l_2l_8,\downarrow\downarrow}(\mathbf{k}_1, \mathbf{k}_1 - \mathbf{q}')n_{l_2\downarrow}(\mathbf{k}_1)c_{l_6,\uparrow}^\dagger(\mathbf{k}_1 + \mathbf{q} - \mathbf{q}')c_{l_8,\downarrow}(\mathbf{k}_1 - \mathbf{q}') \\ & \quad \left. + f_{l_2l_8,\downarrow\downarrow}(\mathbf{k}_1, \mathbf{k}_1 - \mathbf{q}')f_{l_6l_1,\uparrow\uparrow}(\mathbf{k}_1 + \mathbf{q} - \mathbf{q}', \mathbf{k}_1 + \mathbf{q})n_{l_1\uparrow}(\mathbf{k}_1 + \mathbf{q})c_{l_6,\uparrow}^\dagger(\mathbf{k}_1 + \mathbf{q} - \mathbf{q}')c_{l_8,\downarrow}(\mathbf{k}_1 - \mathbf{q}') \right]. \end{aligned} \quad (5.22)$$

At this point, we would like to point out that because $f_{l_i l_j} \propto \delta_{\tau_i\tau_j}$ and $\tau_1 = \tau_2$, all the electronic operators have the same valley index τ in this expression.

Finally, we introduce $\rho_{s_1 s_2}^{ab}(\mathbf{q}) = \sum_{l\mathbf{k}} \phi_{l s_1}^{a*}(\mathbf{k} + \mathbf{q})c_{l\uparrow}^\dagger(\mathbf{k} + \mathbf{q})c_{l\downarrow}(\mathbf{k})\phi_{l s_2}^b(\mathbf{k})$ and $n_s^{ab} = \sum_{\mathbf{k}l} \phi_{l s}^a(\mathbf{k})n_{l s}(\mathbf{k})\phi_{l s}^{b*}(\mathbf{k})$ to write

$$\begin{aligned} & \left[H_{\text{int}}, c_{l_1\uparrow}^\dagger(\mathbf{k}_1 + \mathbf{q})c_{l_2\downarrow}(\mathbf{k}_1) \right] \\ \rightarrow & -2U \sum_{abl'} \left[n_{\uparrow}^{ab}\phi_{l_1\uparrow}^b(\mathbf{k}_1 + \mathbf{q})\phi_{l_1\uparrow}^{a*}(\mathbf{k}_1 + \mathbf{q})c_{l_1\uparrow}^\dagger(\mathbf{k}_1 + \mathbf{q})c_{l_2\downarrow}(\mathbf{k}_1) \right. \\ & \quad \left. - n_{\downarrow}^{ab}\phi_{l_2\downarrow}^b(\mathbf{k}_1)\phi_{l_2\downarrow}^{a*}(\mathbf{k}_1)c_{l_1\uparrow}^\dagger(\mathbf{k}_1 + \mathbf{q})c_{l_2\downarrow}(\mathbf{k}_1) \right] \end{aligned}$$

$$+ 2U \sum_{ab} \phi_{l_1\uparrow}^a(\mathbf{k}_1 + \mathbf{q}) \left[n_{l_1\uparrow}(\mathbf{k}_1 + \mathbf{q}) - n_{l_2\downarrow}(\mathbf{k}_1) \right] \phi_{l_2\downarrow}^{b*}(\mathbf{k}_1) \rho_{\uparrow\downarrow}^{ab}(\mathbf{q}). \quad (5.23)$$

Substituting Eq. (5.20) and Eq. (5.23) in Eq. (5.19) we obtain a closed expression for the response function that involves elements of the static density matrix described in the last subsection. This is the form in which we carry out the time-dependent Hartree-Fock approximation. The resulting equation may be expressed as

$$\begin{aligned} i\partial_t \tilde{\chi}_{l_1 l_2 l_3 l_4}(\mathbf{k}_1, \mathbf{k}_2, \mathbf{q}, t) = & \{n_{l_1\uparrow}(\mathbf{k}_1 + \mathbf{q}) - n_{l_2\downarrow}(\mathbf{k}_1)\} \delta_{l_1 l_4} \delta_{l_2 l_3} \delta_{\mathbf{k}_1, \mathbf{k}_2 - \mathbf{q}} \\ & - \left[\tilde{\epsilon}_{l_1, \uparrow}(\mathbf{k}_1 + \mathbf{q}) - \tilde{\epsilon}_{l_2, \downarrow}(\mathbf{k}_1) \right] \tilde{\chi}_{l_1 l_2 l_3 l_4}(\mathbf{k}_1, \mathbf{k}_2, \mathbf{q}, t) \\ & + 2U \sum_{ab} \left[\phi_{l_1\uparrow}^a(\mathbf{k}_1 + \mathbf{q}) \left(n_{l_2\downarrow}(\mathbf{k}_1) - n_{l_1\uparrow}(\mathbf{k}_1 + \mathbf{q}) \right) \phi_{l_2\downarrow}^{b*}(\mathbf{k}_1) \right] \tilde{\chi}_{\uparrow\downarrow l_3 l_4}^{ab}(\mathbf{k}_1, \mathbf{k}_2, \mathbf{q}, t), \end{aligned} \quad (5.24)$$

where

$$\tilde{\chi}_{s_1 s_2 l_3 l_4}^{ab}(\mathbf{k}_2, \mathbf{q}, t) \equiv \sum_{l_1 l_2 \mathbf{k}_1} \phi_{l_1 s_1}^{a*}(\mathbf{k}_1 + \mathbf{q}) \phi_{l_2 s_2}^b(\mathbf{k}_1) \tilde{\chi}_{l_1 l_2 l_3 l_4}(\mathbf{k}_1, \mathbf{k}_2, \mathbf{q}, t)$$

defines $\tilde{\chi}_{\uparrow\downarrow l_3 l_4}^{ab}$ and $\phi_{l, s}^a$ is the amplitude for the a th orbital (see Eq. (5.13)). Fourier transforming Eq. (5.24) with respect to time, with further work it may be cast in the form

$$-\chi_0^{cd, c'd'}(\mathbf{q}, \omega) = \chi^{cd, c'd'}(\mathbf{q}, \omega) - 2U_0 \sum_{ab} \chi_0^{cd, ab}(\mathbf{q}, \omega) \chi^{ab, c'd'}(\mathbf{q}, \omega). \quad (5.25)$$

Here $U_0 = L_x L_y U$, $\chi^{cd, c'd'}(\mathbf{q}, \omega) \equiv \frac{1}{L_x L_y} \sum_{l_3, l_4, \mathbf{k}} \tilde{\chi}_{\uparrow\downarrow l_3 l_4}^{cd}(\mathbf{k}, \mathbf{q}, \omega) \phi_{l_4\uparrow}^c(\mathbf{k}) \phi_{l_3\downarrow}^{d'*}(\mathbf{k} - \mathbf{q})$, and

$$\chi_0^{ab, cd}(\mathbf{q}, \omega) = -\frac{1}{L_x L_y} \sum_{l_3, l_4, \mathbf{k}_2} \frac{n_{l_4\uparrow}(\mathbf{k}_2) - n_{l_3\downarrow}(\mathbf{k}_2 - \mathbf{q})}{\omega + i\delta + \tilde{\epsilon}_{l_4, \uparrow}(\mathbf{k}_2) - \tilde{\epsilon}_{l_3, \downarrow}(\mathbf{k}_2 - \mathbf{q})} \phi_{l_4\uparrow}^{a*}(\mathbf{k}_2) \phi_{l_3\downarrow}^b(\mathbf{k}_2 - \mathbf{q}) \phi_{l_4\uparrow}^c(\mathbf{k}_2) \phi_{l_3\downarrow}^{d*}(\mathbf{k}_2 - \mathbf{q}) \quad (5.26)$$

is the susceptibility associated with the single-particle Hamiltonian $H^{0, HF}$, which may be viewed as a 4×4 matrix written in the basis AA, BB, AB, BA .

Finally, we write Eq. (5.25) in matrix form and relate it to the physical response function in Eq. (5.17), yielding

$$\chi_\tau(\mathbf{q}, \omega) = -\text{Tr}' \left[\left(1 - 2U_0 \chi_0(\mathbf{q}, \omega) \right)^{-1} \chi_0(\mathbf{q}, \omega) \right]. \quad (5.27)$$

In this equation, all the matrices are 4×4 . but the Tr' is taken only over the ‘‘diagonal’’ elements, $\text{Tr}' \chi^{ab, cd} = \sum_{a, c=A, B} \chi^{aa, cc}$. Eq. (5.27) is one of our main results.

When $\text{Im}\chi(\mathbf{q}, \omega) \neq 0$ the system may absorb energy from a perturbation that flips an electron spin, so that the system has spin excitations with energy ω at momentum q ; as a function of ω for fixed q this either comes over a range of frequencies, where there is a continuum of excitations, or as sharp poles where there is a collective mode [124]. The latter case is characterized by

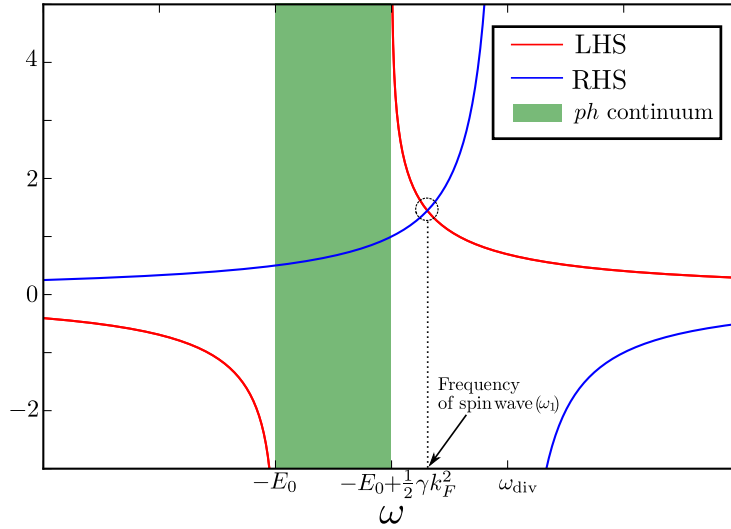


Figure 5.5: Schematic representation of the left and right hand sides of Eq. (5.37) as functions of ω , shown in red and blue respectively. For low enough k_F , an isolated spin wave mode is always present.

$\text{Det}(1 - 2U_0\chi_0(\mathbf{q}, \omega)) = 0$. An example of $\chi(\mathbf{q}, \omega)$ is illustrated in Fig. 5.1, where both a continuum and a sharp collective mode are evident. Fig. 5.4 shows the same example on a linear scale. In this case a sharp collective mode is expected at the point where the relevant determinant vanishes. This mode is separated from the “incoherent” particle-hole excitations whose edge is denoted by ω_c .

In addition to the collective mode that is evident in Fig. 5.4, a second mode arises very close to the particle-hole continuum edge, which is rather difficult to discern in the response function due to its close proximity to the continuum excitations. The presence of such a mode can be demonstrated explicitly by examining the low hole-doping limit. We now turn to this discussion.

5.4 Spin-wave modes for small hole-doping

For small densities of holes, it is possible to make analytical progress on finding zeros of $\text{Det}(1 - 2U\chi_0(\mathbf{q}, \omega))$ in the limit $q \rightarrow 0$, indicating the location of sharp, collective spin-wave modes. Specifying $\tau = 1$ as the valley we will focus upon, the valence bands are indexed by $\alpha = -1$ in Eq. (5.14). The dominant contributions to χ_0 in Eq. (5.26) come from $l_3 = l_4 = \{\tau = 1, \alpha = -1\}$. This leads to the approximate expression

$$\tilde{\chi}_0^{ab,cd}(\mathbf{q} = 0) = -\frac{1}{L_x L_y} \sum_{\mathbf{k}} M^{ab,cd}(\mathbf{k}) \frac{\Delta n(k)}{\omega + i\delta + \Delta\tilde{\epsilon}(k)}, \quad (5.28)$$

where $\Delta n(k) = n_{\uparrow}(k) - n_{\downarrow}(k)$ and $\Delta\tilde{\epsilon}(k) = \lambda - (\tilde{m}_{\uparrow} - \tilde{m}_{\downarrow}) - U(n_{\uparrow}(k) - n_{\downarrow}(k)) - \frac{1}{2} \left(\frac{1}{\tilde{m}_{\uparrow}} - \frac{1}{\tilde{m}_{\downarrow}} \right) (atk)^2 \equiv E_0 - \frac{1}{2}\gamma k^2$, where $E_0 = \lambda - (\tilde{m}_{\uparrow} - \tilde{m}_{\downarrow}) - U_0(n_{\uparrow}(k) - n_{\downarrow}(k))$ and $\gamma = \left(\frac{1}{\tilde{m}_{\uparrow}} - \frac{1}{\tilde{m}_{\downarrow}} \right) (at)^2$. Notice we have employed a small k expansion of $\tilde{\epsilon}(k)$, which works well because $\Delta n(k)$ differs

from zero only at small k in the low hole doping limit. The particle-hole continuum is identified by the interval of ω for which $\omega + \Delta\tilde{\epsilon}(k)$ vanishes for some k where $\Delta n(k) \neq 0$. This range is given in the present approximation by $-E_0 < \omega < -E_0 + \frac{1}{2}\gamma k_F^2 \equiv \omega_c$, where k_F is the Fermi wavevector for the pocket of holes in the valence band.

The matrix elements $M^{ab,cd}(\mathbf{k}) = \phi_{\uparrow}^{a*}(\mathbf{k})\phi_{\downarrow}^b(\mathbf{k})$ can be obtained by similarly expanding the Hartree-Fock wave functions for small k ,

$$\tilde{\phi}_s(\mathbf{k}) \approx \begin{bmatrix} e^{-i\phi} \frac{atk}{2\tilde{m}_s} \\ -[1 - \frac{(atk)^2}{8\tilde{m}_s^2}] \end{bmatrix}, \quad (5.29)$$

where only up to second order terms in k are kept. To this order the only relevant non-vanishing elements of the M matrix are

$$\begin{aligned} M^{AA,BB} &= M^{BB,AA} = \frac{(atk)^2}{4\tilde{m}_{\uparrow}\tilde{m}_{\downarrow}}, \\ M^{BB,BB} &= 1 - \frac{(atk)^2}{4\tilde{m}_{\uparrow}^2} - \frac{(atk)^2}{4\tilde{m}_{\downarrow}^2}, \\ M^{AB,BA} &= M^{BA,AB} = \frac{(atk)^2}{4\tilde{m}_{\uparrow}^2}. \end{aligned}$$

Except for $M^{AA,AA}$ which vanishes to $\mathcal{O}(k^2)$, all the other entries of M contain phases of the form $e^{-i\phi}$, with ϕ the angle of \mathbf{k} with respect to the k_x -axis, which vanishes upon integration over momentum. Thus these do not contribute to $\tilde{\chi}_0$. At $\mathbf{q} = 0$, $\tilde{\chi}_0$ has a block-diagonal form and $\text{Det}(1 - 2U\chi_0(\mathbf{q}, \omega))$ can be written as the product of two subdeterminants, D_1 and D_2 , given by

$$\begin{aligned} D_1 &= (1 - 2U_0\tilde{\chi}_0^{AA,AA})(1 - 2U_0\tilde{\chi}_0^{BB,BB}) \\ &\quad - 4U_0^2\tilde{\chi}_0^{AA,BB}\tilde{\chi}_0^{BB,AA}, \end{aligned} \quad (5.30)$$

$$D_2 = 1 - 4U_0^2\tilde{\chi}_0^{AB,BA}\tilde{\chi}_0^{BA,AB}. \quad (5.31)$$

If either of these vanishes at an ω outside the particle-hole continuum frequency interval, there is a sharp collective mode at that frequency. Note that particular response functions appearing in D_1 and D_2 indicate that the former is associated with spin flips in which electrons remain in the same orbital, while the latter arises due to electrons which both flip spin and change orbital.

Using the integrals

$$\begin{aligned} I_0 &= \frac{1}{L_x L_y} \sum_{|\mathbf{k}| < k_F} \frac{1}{\omega + E_0 - \frac{1}{2}\gamma k^2} \\ &= \int_0^{k_F} \frac{k dk}{2\pi} \frac{1}{\omega + E_0 - \frac{1}{2}\gamma k^2} \\ &= -\frac{1}{2\pi\gamma} \ln \left(\frac{\omega + E_0 - \frac{1}{2}\gamma k_F^2}{\omega + E_0} \right) \end{aligned} \quad (5.32)$$

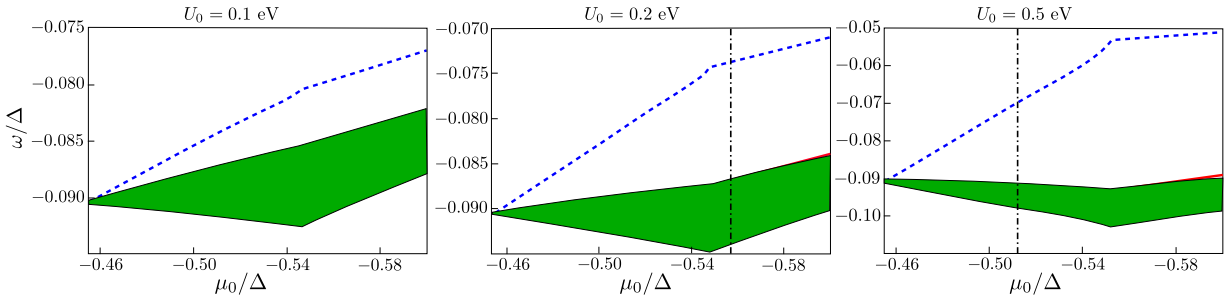


Figure 5.6: Spin wave excitations and the particle-hole continuum as a function of the chemical potential (μ_0) shown for three different values of the interaction strength U_0 when $\mathbf{q} = \mathbf{0}$. The blue dashed line corresponds to the mode described in Fig. 5.5. The mode corresponding to Eq. (5.40) is barely visible as a red line. The vertical lines indicate the boundary beyond which the stability condition is violated.

and

$$\begin{aligned}
 I_1 &= \frac{1}{L_x L_y} \sum_{|\mathbf{k}| < k_F} \frac{k^2}{\omega + E_0 - \frac{1}{2}\gamma k^2} \\
 &= \frac{1}{2\pi\gamma} \left[-\frac{\omega + E_0}{\gamma} \ln \left(\frac{\omega + E_0 - \frac{1}{2}\gamma k_F^2}{\omega + E_0} \right) - k_F^2 \right], \tag{5.33}
 \end{aligned}$$

the condition $D_1 = 0$ reduces to

$$1 - 2U_0 \left(I_0 - \frac{(at)^2}{4} \left(\frac{1}{\tilde{m}_\uparrow^2} + \frac{1}{\tilde{m}_\downarrow^2} \right) I_1 \right) = \frac{U_0^2 (at)^4}{4\tilde{m}_\uparrow^2 \tilde{m}_\downarrow^2}. \tag{5.34}$$

Similarly, $D_2 = 0$ can be simplified to

$$I_1 = \pm \frac{2\tilde{m}_\uparrow \tilde{m}_\downarrow}{U_0 (at)^2}. \tag{5.35}$$

The condition Eq. (5.34) will be met for some value of ω outside the particle-hole continuum, for small interaction strength U_0 . This can be understood as follows. For small U_0 , we approximate the equation as

$$\frac{(at)^2}{4} \left(\frac{1}{\tilde{m}_\uparrow^2} + \frac{1}{\tilde{m}_\downarrow^2} \right) I_1 \approx I_0 - \frac{1}{2U_0}. \tag{5.36}$$

Using the fact that

$$I_1 = \frac{\omega + E_0}{\gamma} I_0 - \frac{k_F^2}{2\pi\gamma}$$

this equation can be recast as

$$I_0 = \frac{(at/2)^2 \left(\frac{1}{\tilde{m}_\uparrow^2} + \frac{1}{\tilde{m}_\downarrow^2} \right) \frac{k_F^2}{2\pi\gamma} - \frac{1}{2U_0}}{(at/2)^2 \left(\frac{1}{\tilde{m}_\uparrow^2} + \frac{1}{\tilde{m}_\downarrow^2} \right) \frac{E_0 + \omega}{\gamma} - 1}. \quad (5.37)$$

The numerator of the right hand side of this equation is negative for small U_0 . As ω increases from large negative values, the right hand side is positive and increases in magnitude, diverging at

$$\omega = \omega_{\text{div}} \equiv -E_0 + \frac{4\gamma}{a^2 t^2} \left(\frac{1}{\tilde{m}_\uparrow^2} + \frac{1}{\tilde{m}_\downarrow^2} \right)^{-1}. \quad (5.38)$$

Importantly, $\omega_{\text{div}} > \omega_c$ in the low doping limit, so the divergence is above the particle-hole continuum. Above ω_{div} the right hand side increases uniformly from arbitrarily large negative values, eventually vanishing at large positive ω . By contrast, I_0 diverges to large negative values as $\omega \rightarrow -E_0$ from below, and comes down from arbitrarily large positive values starting at the particle-hole continuum edge ω_c . This guarantees there will be a crossing of the left and right hand sides of Eq. (5.37) between this edge and ω_{div} , and a collective mode with frequency ω_1 in this interval. This is qualitatively shown in Fig. 5.5. Note that for decreasing U_0 this solution moves closer to the particle-hole continuum, which we indeed find numerically, as illustrated in Fig. 5.6. As is shown in the next section, for small U_0 and small hole doping, one can show that for $\mathbf{q} = 0$

$$\omega_1 \approx -E_0 + \frac{1}{2}\gamma k_F^2 \left(1 + e^{-\pi\gamma/U_0} \right). \quad (5.39)$$

The second condition Eq. (5.35), for small U_0 , can only be satisfied for the negative sign of the right hand side. The position of the spinwave mode at $\mathbf{q} = 0$ can be approximately evaluated to be

$$\omega_2 \approx -E_0 + \frac{1}{2}\gamma k_F^2 \left(1 + e^{-\epsilon_0/k_F^2 U_0} \right), \quad (5.40)$$

where $\epsilon_0 = 8\pi\tilde{m}_\uparrow\tilde{m}_\downarrow/a^2 t^2$. It is clear from Eqs. (5.39) and (5.40) that the separation of ω_2 from the particle-hole continuum is very small when compared to that of ω_1 for small hole doping and for the relevant parameter range. This result is again consistent with our numerical solutions, as illustrated in Fig. 5.6.

We conclude this section with two comments on these results. First, the appearance of a sharp collective mode with arbitrarily small U_0 supports the interpretation of the non-interacting groundstate as being effectively polarized in a ‘‘pseudospin’’ spin variable, $\sigma_z \tau_z$, as discussed in the Introduction. When interactions are introduced, incoherent particle-hole excitations are pushed up in energy via a loss of exchange energy which, for repulsive interactions, generically

lowers the groundstate energy for a polarized state. However, an appropriate linear combination of particle-hole pair states can minimize this loss of exchange energy, leading to the sharp collective mode.

Secondly, although we have demonstrated the existence of two discrete modes, the second of these (at $\omega = \omega_2$) lies exceedingly close to the particle-hole continuum edge. This means that small perturbations can easily admix these different kinds of modes together, making the detection of the second mode challenging. Indeed, in our own numerics the introduction of broadening in our discrete wavevector sum, introduced to simulate the thermodynamic limit, typically mixes this mode with the continuum. In this situation the mode does not show up sharply in the response function we focus upon. We note that our analysis shows the mode to be associated with simultaneous spin flip *and* a change of orbital, $A \leftrightarrow B$, so that we expect this second mode should show up more prominently in more complicated response functions that simultaneously probe both of these.

5.5 Numerical Results and Discussion

In general, to compute χ_τ we need to know χ_0 . This can be obtained numerically, and we accomplish this by approximating the integral in Eq. (5.26) as a discrete sum. For our calculations we discretize momenta onto a 100×100 two dimensional grid, with each momentum component running from $-k_0$ to $+k_0$. We have checked that the contribution to χ_0 dies off quickly within the range of momentum integration. We also discretize ω to a set of 5000 points, within which we compute physical response functions. A small but non-vanishing imaginary η is retained, of the order of the spacing of the ω values, to produce the continuity expected in the thermodynamic limit (where the momentum grid over which we sum becomes arbitrarily fine). Figs. 5.1 and 5.4 depict typical results.

The response function Eq. (5.15) qualitatively describes the dynamics of an electron-hole pair between bands of opposite spins. The lowest energy excitations necessarily involve the bands nearest the chemical potential μ . When μ is within the gap so that the system is insulating, such an excitation will have energy comparable to the band gap $E_g \sim 1\text{eV}$ [125–127]. On the other hand, when hole-doped, the chemical potential falls below the top of the valence band, electron-hole pairs from the two spin species in the valence band become available (see Fig. 5.3). The resulting excitations can have energy of order $\lambda \sim 0.1\text{eV}$, a considerably lower energy scale. Discrete poles in χ have infinite lifetime and represent the collective spin-wave modes of the system; these only can arise when interactions are included in the model. A set of representative plots illustrating both the spin-wave dispersion and the particle-hole continuum are shown in Fig. 5.7 for both the valleys. Note the clear symmetry apparent between the two valley responses when $\omega \rightarrow -\omega$. This is a manifestation of time-reversal symmetry, and indicates that strong absorption from a perturbation with one helicity in one of the two valleys implies equally strong absorption in the other valley when the helicity is reversed.

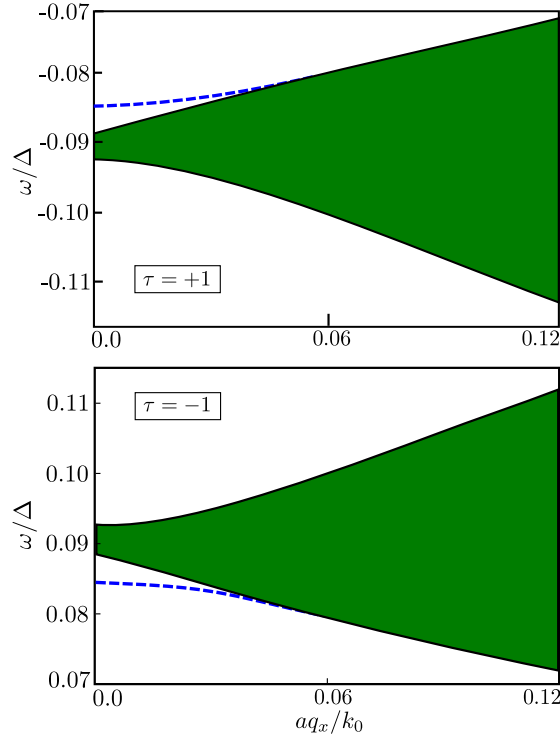


Figure 5.7: The blue line depicts the dispersion of the isolated spin wave excitation, i.e., the ω, q_x points for which the real part of the denominator of the spin susceptibility given by Eq. (5.27) vanishes. The green continuum represents the particle-hole excitations for which the denominator of Eq. (5.27) has a nonvanishing imaginary component. Here we have taken $U_0 = 0.2\text{eV}$.

It is interesting to consider the possible consequences of this if the system develops true ferromagnetism, which is thought to occur above some critical interaction strength U_c [121, 122]. In the simplest description, this leads to different self-consistent exchange fields and different hole populations for each valley [122]. The computation of spin-response in this situation is essentially the same as carried out in our study, but the effective chemical potential would be different for each valley. In this case we expect the spin response to be different for the two possible perturbations, reflecting the broken time-reversal symmetry in the groundstate. Such behavior has indeed been observed for *electron-doped* TMD's [121].

Another feature apparent in Fig. 5.6 is a cusp in the continuum spectrum, which appears at $\mu_0 = \mu_c \approx -0.55\Delta$. This is the point at which the chemical potential touches the top of the lower valence band (Fig. 5.3). For $\mu_0 > \mu_c$, a particle-hole continuum is only present at non-vanishing frequencies determined by the difference in energy between the highest occupied and the lowest unoccupied bands of opposite spins. However, for $\mu_0 \leq \mu_c$, low energy particle-hole excitations set in for processes in which (for one of the valleys) a spin-down valence band electron is excited to the spin-up valence band at finite wave vector, but vanishing frequencies. This is further illustrated in Fig. 5.2, in which one finds the continuum excitations reaching down to zero energy, at a finite q_x , only when the chemical potential is below this critical value.

As is apparent from Fig. 5.4 the first spin-wave mode from the condition Eq. (5.37) appears above the continuum. Further, for a given U_0 , the separation from the continuum increases linearly

with increasing hole doping, as illustrated in Fig. 5.7, until the chemical potential touches the top of the lower valence band. At this point a similar cusp as for the continuum appears in the spin wave dispersion. The linear increase of the separation between the spin wave mode and the top of the particle-hole continuum at small hole doping can be understood in the following way.

For small U_0 , assuming that the renormalized masses \tilde{m}_s to be close to their non-interacting values, we can write

$$\frac{1}{\tilde{m}_\uparrow^2} + \frac{1}{\tilde{m}_\downarrow^2} \approx \left(\frac{2}{\Delta - \lambda}\right)^2 + \left(\frac{2}{\Delta + \lambda}\right)^2 \approx \frac{8}{\Delta^2}. \quad (5.41)$$

Furthermore, we note

$$\frac{\gamma}{(at)^2} = \frac{1}{\tilde{m}_\uparrow} - \frac{1}{\tilde{m}_\downarrow} \approx 4\frac{\lambda}{\Delta^2}. \quad (5.42)$$

These allow Eq. (5.37) for small U_0 and small hole doping to be written as:

$$\frac{-1}{2\pi\gamma} \ln \left(\frac{\omega - \omega_c}{\omega - \omega_c + \frac{1}{2}\gamma k_F^2} \right) \approx \frac{\frac{k_F^2}{2\pi} - \frac{\lambda}{U_0}}{\omega - \omega_c - 2\lambda + \frac{1}{2}\gamma k_F^2}, \quad (5.43)$$

where $\omega_c = -E_0 + \frac{1}{2}\gamma k_F^2$ is the boundary of the continuum of particle-hole excitations. Moreover, again for small U_0 , assuming the upper valence band to have spin up (which is the case for $\tau = +1$), we can write the chemical potential as $\mu_0 \approx -\frac{1}{2}\Delta + \lambda - \frac{1}{2}\frac{(at)^2 k_F^2}{m_\uparrow}$, so that the change in μ_0 due to hole doping can be written as $\delta\mu = \frac{1}{2}\frac{(at)^2 k_F^2}{m_\uparrow}$. Using this in the above equation we get

$$\frac{-1}{2\pi\gamma} \ln \left(\frac{\omega - \omega_c}{\omega - \omega_c + c_0\delta\mu} \right) \approx \frac{1}{2U_0}, \quad (5.44)$$

where, for small $\delta\mu$, $\omega - \omega_c$ and $\frac{1}{2}\gamma k_F^2$ are neglected compared to λ . As the right-hand side is independent of $\delta\mu$, the solution $\omega - \omega_c$ should also scale as $\delta\mu$.

When U_0 is small, the above equation can be solved for $\omega = \omega_1 \approx -E_0 + \frac{1}{2}\gamma k_F^2(1 + e^{-\pi\gamma/U_0})$. Note that this result differs from that of Eq. (5.40) in that k_F^2 appears in the exponential in the latter. This renders $|\omega_2 - \omega_c|$ much smaller than $|\omega_1 - \omega_c|$ in the low hole-doping limit.

As discussed in the previous section, the second spin wave solution of Eq. (5.40) lies extremely close to the continuum, and so is almost invisible in our numerical solutions for the range of the parameters we consider. One expects this mode to be visible for larger U_0 and larger hole doping. However, in our calculations we find that the stability condition [124] $\omega(-\text{Im}\chi_\tau) > 0$ fails for some range of ω for U_0 large enough that we are able to numerically resolve the mode from the continuum. An example of this is shown in Fig. 5.8. The point beyond which this stability condition is not satisfied is indicated by vertical lines in Fig. 5.6. Note that, physically, the instability we find in the response functions indicates that the symmetry of the ground-state we are assuming is broken, very likely into a state with inter-orbital coherence. Whether such a

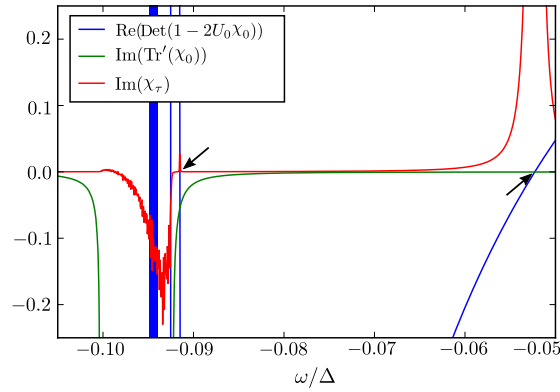


Figure 5.8: Spin susceptibility for $U_0 = 0.5\text{eV}$, $\tau = +1$ and $\mu_0 = -0.57\Delta$. Two discrete spin wave modes (indicated by arrows) are visible near $\omega = -0.055\Delta$ and $\omega = -0.092\Delta$, with the second mode very close to the continuum. However, the positivity $\omega(-\text{Im}\chi) > 0$ does not hold for all ω implying that our assumed Hartree-Fock state is not the true ground state.

state exists at large U , or is preempted by a first-order transition into a state with different hole populations in the valleys, requires a more general Hartree-Fock study than we have presented in this work, and is left for future study.

5.6 Summary

Our calculations indicate that with strong enough interaction the system becomes unstable. Within our model this would likely be to a state with inter-orbital coherence, but first order instabilities in which the system spontaneously forms unequal valley and spin populations are also possible, which may preempt any instability indicated in linear response. Whatever the true groundstate of the system, our formalism in principle allows a calculation of the density matrix associated with it, and of collective modes around it. Moreover, the approach we present can be extended to more general response functions (for example, involving spin and orbital simultaneously) which could reveal further and perhaps clearer signatures of the two collective modes we find in our analysis. Exploration of these represent interesting directions for future work.

Summary and Future Directions

To summarise, in Chapters 2 and 3, we have proposed setups to explore the nature of chiral nodes in WSM by studying transport through a WSM heterostructures. We have considered the minimal models of both inversion symmetry broken and TR symmetry broken WSM-s. We have identified the oscillations that we observe in each of the cases to be closely related to the preservation of the symmetries of the microscopic models. For the TR broken WSM, spin plays the role of the conserved quantity that leads to selection rules for scattering processes in the boundary. For the inversion symmetry broken WSM, the orbital degree of freedom plays an important role along with the spin. In fact, these selection rules lead to the interferometry that we have explored in Chapters 2 and 3.

As far as the relevance of our findings in these chapters to experimental observations are concerned, it should be noted that there are various theoretical proposals for manipulation of the bulk band structure in a WSM. For us, the parameter of relevance is the separation of the Weyl nodes and one way of changing this is by shining high frequency light which has been explored in Ref.[57]. Another interesting way of doing the same could be by straining the sample[128]. The separation can also be tuned by adjusting the magnetic doping [129–131]. In fact, an important point to note is that one of our models requires creating junctions of WSM with normal leads which should be much simpler experimentally than creating junctions of WSM with superconductors. Note also that unlike the $K - K'$ scale in graphene, the k_0 scale in Weyl semimetals is much smaller and does not require very large momentum transfer. Hence, small wiggles in the interfaces will not be able to wash out the signal. Moreover, even atomically sharp junctions are not a bottle-neck with the present day technology of growing thin films of topologically materials[132, 133].

In the predicted WSM material TaAs [134, 135], chiral node pairs (formed by breaking inversion symmetry) are separated in momentum space by a distance $\sim 0.02\text{\AA}^{-1}$. Assuming standard electron mass, the relevant energy scale is about a milli electronvolt, which only becomes larger if the effective mass is smaller. Combining this with the fact that large momentum scattering (from $-k_0$ to k_0) is needed to break the topological protection of the chiral nodes,

helical excitations in WSM are expected to be robust against disorder in a relatively clean sample. The periodicity of the Josephson current as well as the bound levels that we have discussed are, in principle, observable in tunneling experiments. The periodic variation of the bound-levels can also be probed in Andreev spectroscopy. For a typical sample, the length scales for such periodic variations would be of the order of few tens of nanometers.

The effect of having many Weyl nodes complicates the theoretical modeling and presents a weakness in our proposal. But, as long as the transport takes place along a pair of Weyl nodes, a similar periodicity in the transport properties is expected. It is not clear whether these oscillations are present in WSMs with higher Chern numbers. Such studies are left for the future.

In chapter 5, we have studied collective excitations of a simple TMD model, showing that even without the formation of spontaneous magnetic order, interactions induce sharp collective modes that are commonly associated with such order. The presence of these modes can be understood as a consequence of intrinsic order induced by the strong spin-orbit interaction that yields different energetic orderings of spins in different valleys, and arises when the system is doped. The presence of these modes is a direct analog of “Silin-Leggett modes” present in a simple Fermi liquid subject to a magnetic field, such that the Fermi wavevector becomes spin-dependent. Our analysis is developed using the time-dependent Hartree-Fock approximation of a physical spin response function, and reveals two sharp modes in addition to a continuum of particle-hole excitations. While one of these modes (associated with spin flips for electrons maintaining their orbital index) breaks out from the continuum in a clear way, the other (associated with electrons changing both spin and orbital) remains very close to the continuum edge and is difficult to distinguish independently. Signatures of how the subbands are populated can be seen in properties of the spin response functions when the chemical potential is modified, which in principle can be accomplished by gating the system.

Lastly, we sketch some problems for future studies. Apart from transport signatures of the chiral nodes in WSM, the appearance of surface states, and the consequent Fermi arc dispersion is another remarkable feature of WSMs. Their transport characteristics in the Josephson current would be interesting to study. Quantitative investigations of the effects of disorder and interactions on transport in the WSM are also left for future studies. The TDHFA formalism developed in Chapter 5 is very general and studies of collective modes in other topological systems can be done.

In closing, we summarise by pointing out that most of the phenomena discussed in this thesis is a consequence of the nontrivial spin texture of the ground state which in itself, is a consequence of the Dirac equation. Hence, we expect these results to be quite general and should be seen in other systems with similar band structures, thus opening avenues for future research.

Bibliography

- [1] T. Wehling, A. Black-Schaffer, and A. Balatsky, *Advances in Physics* **63**, 1 (2014), <https://doi.org/10.1080/00018732.2014.927109>.
- [2] K. S. Novoselov, A. K. Geim, S. V. Morozov, D. Jiang, Y. Zhang, S. V. Dubonos, I. V. Grigorieva, and A. A. Firsov, *Science* **306**, 666 (2004), <http://science.sciencemag.org/content/306/5696/666.full.pdf>.
- [3] M. C. Lemme, T. J. Echtermeyer, M. Baus, and H. Kurz, *IEEE Electron Device Letters* **28**, 282 (2007).
- [4] X. Wan, A. M. Turner, A. Vishwanath, and S. Y. Savrasov, *Phys. Rev. B* **83**, 205101 (2011).
- [5] A. V. Balatsky, I. Vekhter, and J.-X. Zhu, *Rev. Mod. Phys.* **78**, 373 (2006).
- [6] M. Z. Hasan and C. L. Kane, *Rev. Mod. Phys.* **82**, 3045 (2010).
- [7] Z. Jincheng, X. Xun, F. Haifeng, L. Zhi, W. Xiaolin, and D. Yi, *Science Bulletin* **60**, 1551 (2015).
- [8] G.-B. Liu, W.-Y. Shan, Y. Yao, W. Yao, and D. Xiao, *Phys. Rev. B* **88**, 085433 (2013).
- [9] Y. Du, J. Zhuang, H. Liu, X. Xu, S. Eilers, K. Wu, P. Cheng, J. Zhao, X. Pi, K. W. See, G. Peleckis, X. Wang, and S. X. Dou, *ACS Nano* **8**, 10019 (2014), <https://doi.org/10.1021/nn504451t>, PMID: 25248135.
- [10] J.-A. Yan, S.-P. Gao, R. Stein, and G. Coard, *Phys. Rev. B* **91**, 245403 (2015).
- [11] M. Ezawa, *Journal of the Physical Society of Japan* **84**, 121003 (2015), <https://doi.org/10.7566/JPSJ.84.121003>.
- [12] D. Xiao, G.-B. Liu, W. Feng, X. Xu, and W. Yao, *Phys. Rev. Lett.* **108**, 196802 (2012).
- [13] A. M. Turner and A. Vishwanath, *ArXiv e-prints* (2013), [1301.0330](https://arxiv.org/abs/1301.0330).

- [14] M. Z. Hasan, S.-Y. Xu, I. Belopolski, and S.-M. Huang, Annual Review of Condensed Matter Physics **8**, 289 (2017), <https://doi.org/10.1146/annurev-conmatphys-031016-025225>.
- [15] A. A. Zyuzin and A. A. Burkov, Phys. Rev. B **86**, 115133 (2012).
- [16] J. F. Steiner, A. V. Andreev, and D. A. Pesin, Phys. Rev. Lett. **119**, 036601 (2017).
- [17] M. Z. Hasan, S.-Y. Xu, I. Belopolski, and S.-M. Huang, Annual Review of Condensed Matter Physics **8**, 289 (2017), <https://doi.org/10.1146/annurev-conmatphys-031016-025225>.
- [18] Y. Meir and N. S. Wingreen, Phys. Rev. Lett. **68**, 2512 (1992).
- [19] D. Kanti Mukherjee, S. Rao, and S. Das, ArXiv e-prints (2017), [1710.06873](https://arxiv.org/abs/1710.06873).
- [20] D. K. Mukherjee, S. Rao, and A. Kundu, Phys. Rev. B **96**, 161408 (2017).
- [21] U. Khanna, D. K. Mukherjee, A. Kundu, and S. Rao, Phys. Rev. B **93**, 121409 (2016).
- [22] D. Kanti Mukherjee, J. Hutchinson, and A. Kundu, ArXiv e-prints (2017), [1708.06773](https://arxiv.org/abs/1708.06773).
- [23] D. Kanti Mukherjee, A. Kundu, and H. A. Fertig, ArXiv e-prints (2018), [1805.08223](https://arxiv.org/abs/1805.08223).
- [24] A. H. Castro Neto, F. Guinea, N. M. R. Peres, K. S. Novoselov, and A. K. Geim, Rev. Mod. Phys. **81**, 109 (2009).
- [25] S. Rao, ArXiv e-prints (2016), [1603.02821](https://arxiv.org/abs/1603.02821).
- [26] U. Khanna, A. Kundu, S. Pradhan, and S. Rao, Phys. Rev. B **90**, 195430 (2014).
- [27] Proceedings of the Royal Society of London A: Mathematical, Physical and Engineering Sciences **117**, 610 (1928), <http://rspa.royalsocietypublishing.org/content/117/778/610.full.pdf>.
- [28] H. Weyl, Proc Natl Acad Sci U S A **15**, 323 (1929), 16587474[pmid].
- [29] E. Majorana, Il Nuovo Cimento (1924-1942) **14**, 171 (1937).
- [30] Proceedings of the Royal Society of London A: Mathematical, Physical and Engineering Sciences **392**, 45 (1984), <http://rspa.royalsocietypublishing.org/content/392/1802/45.full.pdf>.
- [31] D. J. Thouless, M. Kohmoto, M. P. Nightingale, and M. den Nijs, Phys. Rev. Lett. **49**, 405 (1982).
- [32] P. Mallet, I. Brihuega, S. Bose, M. M. Ugeda, J. M. Gómez-Rodríguez, K. Kern, and J. Y. Veuillen, Phys. Rev. B **86**, 045444 (2012).

-
- [33] F. D. M. Haldane, *Phys. Rev. Lett.* **61**, 2015 (1988).
- [34] K. F. Mak, C. Lee, J. Hone, J. Shan, and T. F. Heinz, *Phys. Rev. Lett.* **105**, 136805 (2010).
- [35] A. Splendiani, L. Sun, Y. Zhang, T. Li, J. Kim, C.-Y. Chim, G. Galli, and F. Wang, *Nano Letters* **10**, 1271 (2010), <http://dx.doi.org/10.1021/nl903868w>, pMID: 20229981.
- [36] D. Xiao, G.-B. Liu, W. Feng, X. Xu, and W. Yao, *Phys. Rev. Lett.* **108**, 196802 (2012).
- [37] G.-B. Liu, W.-Y. Shan, Y. Yao, W. Yao, and D. Xiao, *Phys. Rev. B* **88**, 085433 (2013).
- [38] T. Cao, G. Wang, W. Han, H. Ye, C. Zhu, J. Shi, Q. Niu, P. Tan, E. Wang, B. Liu, and J. Feng, *Nature Communications* **3**, 887 (2012).
- [39] H. Zeng, J. Dai, W. Yao, D. Xiao, and X. Cui, *Nature Nanotechnology* **7**, 490 (2012).
- [40] K. Mak, K. He, J. Shan, and T. Heinz, *Nature Nanotechnology* **7**, 494 (2012).
- [41] K. F. Mak, K. L. McGill, J. Park, and P. L. McEuen, *Science* **344**, 1489 (2014), <http://science.sciencemag.org/content/344/6191/1489.full.pdf>.
- [42] E. Witten, *Nuovo Cimento Rivista Serie* **39**, 313 (2016), [1510.07698](https://doi.org/10.1007/978-94-007-6998-8_15).
- [43] A. A. Soluyanov, D. Gresch, Z. Wang, Q. Wu, M. Troyer, X. Dai, and B. A. Bernevig, *Nature* **527**, 495 EP (2015).
- [44] C. Fang, M. J. Gilbert, X. Dai, and B. A. Bernevig, *Phys. Rev. Lett.* **108**, 266802 (2012).
- [45] D. Hsieh, Y. Xia, L. Wray, D. Qian, A. Pal, J. H. Dil, J. Osterwalder, F. Meier, G. Bihlmayer, C. L. Kane, Y. S. Hor, R. J. Cava, and M. Z. Hasan, *Science* **323**, 919 (2009), <http://science.sciencemag.org/content/323/5916/919.full.pdf>.
- [46] Y. L. Chen, J.-H. Chu, J. G. Analytis, Z. K. Liu, K. Igarashi, H.-H. Kuo, X. L. Qi, S. K. Mo, R. G. Moore, D. H. Lu, M. Hashimoto, T. Sasagawa, S. C. Zhang, I. R. Fisher, Z. Hussain, and Z. X. Shen, *Science* **329**, 659 (2010), <http://science.sciencemag.org/content/329/5992/659.full.pdf>.
- [47] J.-J. Zhu, D.-X. Yao, S.-C. Zhang, and K. Chang, *Phys. Rev. Lett.* **106**, 097201 (2011).
- [48] L. A. Wray, S.-Y. Xu, Y. Xia, D. Hsieh, A. V. Fedorov, Y. S. Hor, R. J. Cava, A. Bansil, H. Lin, and M. Z. Hasan, *Nature Physics* **7**, 32 EP (2010).
- [49] S.-Y. Xu, M. Neupane, C. Liu, D. Zhang, A. Richardella, L. Andrew Wray, N. Alidoust, M. Leandersson, T. Balasubramanian, J. Sánchez-Barriga, O. Rader, G. Landolt, B. Slomski, J. Hugo Dil, J. Osterwalder, T.-R. Chang, H.-T. Jeng, H. Lin, A. Bansil, N. Samarth, and M. Zahid Hasan, *Nature Physics* **8**, 616 EP (2012), article.
-

- [50] X.-L. Qi and S.-C. Zhang, *Rev. Mod. Phys.* **83**, 1057 (2011).
- [51] S. Roy and S. Das, *Phys. Rev. B* **93**, 085422 (2016).
- [52] S. Roy, K. Roychowdhury, and S. Das, *New Journal of Physics* **18**, 073038 (2016).
- [53] M. M. Vazifeh and M. Franz, *Phys. Rev. Lett.* **111**, 027201 (2013).
- [54] S. Uchida, T. Habe, and Y. Asano, *Journal of the Physical Society of Japan* **83**, 064711 (2014), <https://doi.org/10.7566/JPSJ.83.064711>.
- [55] N. Bovenzi, M. Breitzkreiz, P. Baireuther, T. E. O'Brien, J. Tworzydło, i. d. I. Adagideli, and C. W. J. Beenakker, *Phys. Rev. B* **96**, 035437 (2017).
- [56] A. Chen and M. Franz, *Phys. Rev. B* **93**, 201105 (2016).
- [57] U. Khanna, S. Rao, and A. Kundu, *Phys. Rev. B* **95**, 201115 (2017).
- [58] T. E. O'Brien, C. W. J. Beenakker, and i. d. I. Adagideli, *Phys. Rev. Lett.* **118**, 207701 (2017).
- [59] C. W. J. Beenakker, *Phys. Rev. Lett.* **97**, 067007 (2006).
- [60] T. Dirks, T. L. Hughes, S. Lal, B. Uchoa, Y.-F. Chen, C. Chialvo, P. M. Goldbart, and N. Mason, *Nature Physics* **7**, 386 EP (2011).
- [61] S. Bhattacharjee and K. Sengupta, *Phys. Rev. Lett.* **97**, 217001 (2006).
- [62] S. Bhattacharjee, M. Maiti, and K. Sengupta, *Phys. Rev. B* **76**, 184514 (2007).
- [63] A. R. Akhmerov and C. W. J. Beenakker, *Phys. Rev. Lett.* **98**, 157003 (2007).
- [64] M. P. L. Sancho, J. M. L. Sancho, J. M. L. Sancho, and J. Rubio, *Journal of Physics F: Metal Physics* **15**, 851 (1985).
- [65] L. N. Bulaevskii, V. V. Kuzii, and A. A. Sobyenin, *Soviet Journal of Experimental and Theoretical Physics Letters* **25**, 290 (1977).
- [66] A. I. Buzdin, L. N. Bulaevskii, and S. V. Panyukov, *ZhETF Pisma Redaktsiiu* **35**, 147 (1982).
- [67] A. I. Buzdin and M. Y. Kupriyanov, *JETP Lett* **53**, 321 (1991).
- [68] A. A. Golubov, M. Y. Kupriyanov, and E. Il'ichev, *Rev. Mod. Phys.* **76**, 411 (2004).
- [69] A. I. Buzdin, *Rev. Mod. Phys.* **77**, 935 (2005).
- [70] F. S. Bergeret, A. F. Volkov, and K. B. Efetov, *Rev. Mod. Phys.* **77**, 1321 (2005).

-
- [71] V. V. Ryazanov, V. A. Oboznov, A. Y. Rusanov, A. V. Veretennikov, A. A. Golubov, and J. Aarts, *Phys. Rev. Lett.* **86**, 2427 (2001).
- [72] A. A. Golubov, M. Y. Kupriyanov, and Y. V. Fominov, *Journal of Experimental and Theoretical Physics Letters* **75**, 190 (2002).
- [73] T. Yokoyama, M. Eto, and Y. V. Nazarov, *Phys. Rev. B* **89**, 195407 (2014).
- [74] O. Šipr and B. L. Györfly, *Journal of Low Temperature Physics* **106**, 315 (1997).
- [75] L.-F. Chang and P. F. Bagwell, *Phys. Rev. B* **55**, 12678 (1997).
- [76] N. D. Drummond, V. Zólyomi, and V. I. Fal'ko, *Phys. Rev. B* **85**, 075423 (2012).
- [77] C.-C. Liu, W. Feng, and Y. Yao, *Phys. Rev. Lett.* **107**, 076802 (2011).
- [78] C.-C. Liu, H. Jiang, and Y. Yao, *Phys. Rev. B* **84**, 195430 (2011).
- [79] M. Ezawa, *Phys. Rev. Lett.* **110**, 026603 (2013).
- [80] M. Ezawa, *Journal of the Physical Society of Japan* **84**, 121003 (2015), <https://doi.org/10.7566/JPSJ.84.121003>.
- [81] J. Linder and T. Yokoyama, *Phys. Rev. B* **89**, 020504 (2014).
- [82] K. Li and Y.-Y. Zhang, *Phys. Rev. B* **94**, 165441 (2016).
- [83] X. J. Qiu, Y. F. Cheng, Z. Z. Cao, and C. C. Qin, *Journal of Physics D: Applied Physics* **49**, 245101 (2016).
- [84] J. Wang, L. Hao, and K. S. Chan, *Phys. Rev. B* **91**, 085415 (2015).
- [85] L. Chen, B. Feng, and K. Wu, *Applied Physics Letters* **102**, 081602 (2013), <https://doi.org/10.1063/1.4793998>.
- [86] S. Vosoughi-nia, Y. Hajati, and G. Rashedi, *Journal of Applied Physics* **122**, 043906 (2017), <https://doi.org/10.1063/1.4996347>.
- [87] X. Zhou and G. Jin, *Phys. Rev. B* **94**, 165436 (2016).
- [88] X. Zhou and G. Jin, *Phys. Rev. B* **95**, 195419 (2017).
- [89] F. Dolcini and L. Dell'Anna, *Phys. Rev. B* **78**, 024518 (2008).
- [90] T. Oka and H. Aoki, *Phys. Rev. B* **79**, 081406 (2009).
- [91] W. Yao, A. H. MacDonald, and Q. Niu, *Phys. Rev. Lett.* **99**, 047401 (2007).
- [92] P. Delplace, A. Gómez-León, and G. Platero, *Phys. Rev. B* **88**, 245422 (2013).
-

- [93] Y. T. Katan and D. Podolsky, Phys. Rev. Lett. **110**, 016802 (2013).
- [94] M. Lababidi, I. I. Satija, and E. Zhao, Phys. Rev. Lett. **112**, 026805 (2014).
- [95] T. Iadecola, D. Campbell, C. Chamon, C.-Y. Hou, R. Jackiw, S.-Y. Pi, and S. V. Kusminski, Phys. Rev. Lett. **110**, 176603 (2013).
- [96] N. Goldman and J. Dalibard, Phys. Rev. X **4**, 031027 (2014).
- [97] A. G. Grushin, A. Gómez-León, and T. Neupert, Phys. Rev. Lett. **112**, 156801 (2014).
- [98] C. Dutreix, E. A. Stepanov, and M. I. Katsnelson, Phys. Rev. B **93**, 241404 (2016).
- [99] E. A. Stepanov, C. Dutreix, and M. I. Katsnelson, Phys. Rev. Lett. **118**, 157201 (2017).
- [100] T. Kitagawa, E. Berg, M. Rudner, and E. Demler, Phys. Rev. B **82**, 235114 (2010).
- [101] N. H. Lindner, G. Refael, and V. Galitski, Nature Physics **7**, 490 EP (2011), article.
- [102] B. Dóra, J. Cayssol, F. Simon, and R. Moessner, Phys. Rev. Lett. **108**, 056602 (2012).
- [103] A. Kundu, H. A. Fertig, and B. Seradjeh, Phys. Rev. Lett. **113**, 236803 (2014).
- [104] P. Titum, N. H. Lindner, M. C. Rechtsman, and G. Refael, Phys. Rev. Lett. **114**, 056801 (2015).
- [105] J. Klinovaja, P. Stano, and D. Loss, Phys. Rev. Lett. **116**, 176401 (2016).
- [106] M. Thakurathi, A. A. Patel, D. Sen, and A. Dutta, Phys. Rev. B **88**, 155133 (2013).
- [107] M. Bukov, L. D'Alessio, and A. Polkovnikov, Advances in Physics **64**, 139 (2015), <https://doi.org/10.1080/00018732.2015.1055918>.
- [108] A. Eckardt and E. Anisimovas, New Journal of Physics **17**, 093039 (2015).
- [109] T. Mikami, S. Kitamura, K. Yasuda, N. Tsuji, T. Oka, and H. Aoki, Phys. Rev. B **93**, 144307 (2016).
- [110] P. Mohan, R. Saxena, A. Kundu, and S. Rao, Phys. Rev. B **94**, 235419 (2016).
- [111] Y. H. Wang, H. Steinberg, P. Jarillo-Herrero, and N. Gedik, Science **342**, 453 (2013), <http://science.sciencemag.org/content/342/6157/453.full.pdf>.
- [112] M. C. Rechtsman, J. M. Zeuner, Y. Plotnik, Y. Lumer, D. Podolsky, F. Dreisow, S. Nolte, M. Segev, and A. Szameit, Nature **496**, 196 EP (2013).
- [113] G. Jotzu, M. Messer, R. Desbuquois, M. Lebrat, T. Uehlinger, D. Greif, and T. Esslinger, Nature **515**, 237 EP (2014).

-
- [114] R. Desbuquois, M. Messer, F. Görg, K. Sandholzer, G. Jotzu, and T. Esslinger, *Phys. Rev. A* **96**, 053602 (2017).
- [115] M. Aidelsburger, M. Lohse, C. Schweizer, M. Atala, J. . T. Barreiro, S. Nascimbène, N. . R. Cooper, I. Bloch, and N. Goldman, *Nature Physics* **11**, 162 EP (2014).
- [116] C.-C. Liu, H. Jiang, and Y. Yao, *Phys. Rev. B* **84**, 195430 (2011).
- [117] S. Konschuh, M. Gmitra, and J. Fabian, *Phys. Rev. B* **82**, 245412 (2010).
- [118] M. M. Maricq, *Phys. Rev. B* **25**, 6622 (1982).
- [119] H. Dehghani, T. Oka, and A. Mitra, *Phys. Rev. B* **90**, 195429 (2014).
- [120] T. Mori, T. Kuwahara, and K. Saito, *Phys. Rev. Lett.* **116**, 120401 (2016).
- [121] T. Scrace, Y. Tsai, B. Barman, L. Schweidenback, A. Petrou, G. Kioseoglou, I. Ozfidan, M. Korkusinski, and P. Hawrylak, *Nature Nanotechnology* **10**, 603 (2015).
- [122] J. Braz, B. Amorim, and E. Castro, [arXiv:1712.07157](https://arxiv.org/abs/1712.07157).
- [123] See, for example, article by A. Pinczuk in *Perspectives in Quantum Hall Effects*, S. Das Sarma and A. Pinczuk, eds., (Wiley, New York, 1997).
- [124] G. Giuliani and G. Vignale, *Quantum Theory of the Electron Liquid* (Cambridge University Press, 2005).
- [125] J. S. Ross, S. Wu, H. Yu, N. J. Ghimire, A. M. Jones, G. Aivazian, J. Yan, D. G. Mandrus, D. Xiao, W. Yao, and X. Xu, *Nature Communications* **4** (2013).
- [126] M. M. Ugeda, A. J. Bradley, S.-F. Shi, F. H. da Jornada, Y. Zhang, D. Y. Qiu, W. Ruan, S. Mo, Z. Hussain, Z. Shen, F. Wang, S. G. Louie, and M. F. Crommie, *Nature Materials* **13**, 1091 (2014).
- [127] F. Wu, F. Qu, and A. H. MacDonald, *Phys. Rev. B* **91**, 075310 (2015).
- [128] D. I. Pikulin, A. Chen, and M. Franz, *Phys. Rev. X* **6**, 041021 (2016).
- [129] Y. L. Chen, J.-H. Chu, J. G. Analytis, Z. K. Liu, K. Igarashi, H.-H. Kuo, X. L. Qi, S. K. Mo, R. G. Moore, D. H. Lu, M. Hashimoto, T. Sasagawa, S. C. Zhang, I. R. Fisher, Z. Hussain, and Z. X. Shen, *Science* **329**, 659 (2010).
- [130] C. Chang, J. Zhang, M. Liu, Z. Zhang, X. Feng, K. Li, L. Wang, X. Chen, X. Dai, Z. Fang, X. Qi, S. Zhang, Y. Wang, K. He, X. Ma, and Q. Xue, *Advanced Materials* **25**, 1065 (2013).
-

- [131] D. Kurebayashi and K. Nomura, *Journal of the Physical Society of Japan* **83**, 063709 (2014), <https://doi.org/10.7566/JPSJ.83.063709>.
- [132] N. Bansal, Y. S. Kim, E. Edrey, M. Brahlek, Y. Horibe, K. Iida, M. Tanimura, G.-H. Li, T. Feng, H.-D. Lee, T. Gustafsson, E. Andrei, and S. Oh, *Thin Solid Films* **520**, 224 (2011).
- [133] S. H. Kim, K.-H. Jin, B. W. Kho, B.-G. Park, F. Liu, J. S. Kim, and H. W. Yeom, *ACS Nano* **11**, 9671 (2017), <https://doi.org/10.1021/acsnano.7b03880>, PMID: 28825806.
- [134] S.-M. Huang, S.-Y. Xu, I. Belopolski, C.-C. Lee, G. Chang, B. Wang, N. Alidoust, G. Bian, M. Neupane, C. Zhang, S. Jia, A. Bansil, H. Lin, and M. Hasan, *Nature Communications* **6**, 7373 (2015).
- [135] L. X. Yang, Z. K. Liu, Y. Sun, H. Peng, H. F. Yang, T. Zhang, B. Zhou, Y. Zhang, Y. F. Guo, M. Rahn, D. Prabhakaran, Z. Hussain, S.-K. Mo, C. Felser, B. Yan, and Y. L. Chen, *Nature Physics* **11**, 728 EP (2015).